

Geometric Approaches in Phase Space Transport and Partial Control of Escaping Dynamics

Shibabrat Naik

Dissertation submitted to the
Virginia Polytechnic Institute and State University
in partial fulfillment of the requirements for the degree of

Doctor of Philosophy
in
Engineering Mechanics

Shane D. Ross, Chair

Mark R. Paul

Ishwar K. Puri

Craig A. Woolsey

Sunghwan Jung

Blacksburg, Virginia

9 September, 2016

Keywords: Invariant manifolds, Phase space transport, Escaping dynamics, Partial control

Copyright 2016, Shibabrat Naik

All rights reserved

Geometric Approaches in Phase Space Transport and Partial Control of Escaping Dynamics

Shibabrat Naik

ABSTRACT

This dissertation presents geometric approaches of understanding *chaotic transport* in phase space that is fundamental across many disciplines in physical sciences and engineering. This approach is based on analyzing phase space transport using boundaries and regions inside these boundaries in presence of perturbation.

We present a geometric view of defining such boundaries and study the transport that occurs by crossing such phase space structures. The structure in two dimensional non-autonomous system is the codimension 1 stable and unstable manifolds (that is \mathbb{R}^1 geometry) associated with the hyperbolic fixed points. The manifolds separate regions with varied dynamical fates and their time evolution encodes how the initial conditions in a given region of phase space get transported to other regions. In the context of four dimensional autonomous systems, the corresponding structure is the stable and unstable manifolds (that is $\mathbb{S}^1 \times \mathbb{R}^1$ geometry) of unstable periodic orbits which reside in the bottlenecks of energy surface. The total energy and the cylindrical (or tube) manifolds form the necessary and sufficient condition for global transport between regions of phase space.

Furthermore, we adopt the geometric view to define *escaping zones* for avoiding transition/escape from a potential well using *partial control*. In this approach, the objective is two fold: finding the *minimum control* that is required for avoiding escape and obtaining discrete representation called *disturbance* of continuous noise that is present in physical sciences and engineering. In the former scenario, along with avoiding escape, the control is constrained to be smaller than the disturbance so that it can not exactly cancel out the disturbances.

The work presented was funded by Virginia Tech and National Science Foundation under

award #1150456 and #1537349.

Geometric Approaches in Phase Space Transport and Partial Control of Escaping Dynamics

Shibabrat Naik

GENERAL AUDIENCE ABSTRACT

The prediction and control of critical events in engineering systems has been a major objective of scientific research in recent years. The multifaceted problems facing the modern society includes critical events such as spread of pathogens and pollutants in atmosphere and ocean, capsize of boats and cruise ships, space exploration and asteroid collision, to name but a few. Although, at first glance they seem to be disconnected problems in different areas of engineering and science, however, they have certain features that are inherently common. This can be studied using the abstraction of *phase space* which can be thought of as the universe where all possible solutions of the governing equations, derived using principles of physics, live and evolve in time. The phase space can be just 2D, 3D or even infinite dimensional but the critical events manifest themselves as volumes of phase space, which represent solutions at a given instant of time, get transported from one region to another due to the underlying dynamics. This mathematical abstraction is called phase space transport and studied under the umbrella of dynamical systems theory. The geometric view of the solutions that live in the phase space provides insight into the mechanisms of how the critical events occur, and the understanding of these mechanisms is useful in deciding about control strategies.

A slightly different view for understanding critical events is to consider a thought experiment where a ball is rolling on a multi-well surface or potential well. As the time evolves, the ball will escape from its initial well and roll into another well, and eventually start exploring all the wells in a seemingly unpredictable way. However, these unpredictable escape/transition can be studied systematically using methods of chaos and dynamical systems. The escape/transition in a potential well implies a dramatic change in the behavior of the system,

and hence the significance in prediction and control of *escaping dynamics*. The control aspect becomes more challenging due to inherent disturbance in the system that is difficult to model and we may not have the equal or more control authority to cancel those disturbances. However, we can usually estimate the maximum values of the disturbance, and try to avoid escaping from the potential well while using a smaller control. This idea is called *partial control of escaping dynamics* and can guarantee avoidance of escape for *ad infinitum*.

In this doctoral research, we focus on the two mechanisms, phase space transport and escaping dynamics, by considering problems from fluid dynamics and capsize of a ship. The applications are used for numerical demonstration and evidence of the general approach in studying a large class of problems in classical physics.

The work presented was funded by Virginia Tech and National Science Foundation under award #1150456 and #1537349.

*To my parents, Jyotsna Mayee and Tarini Sen Naik
for teaching me the core values of life summarized by*

*karmaṇy-evādhikāras te mā phaleṣhu kadāchana
mā karma-phala-hetur bhūr mā te saṅgo 'stvakarmaṇi*

Bhagavad Gita: Chapter 2, Verse 47

Acknowledgments

I would like to express my deepest gratitude towards Prof. Shane Ross for being a kind and supporting adviser. His clarity in thinking and simple explanations of difficult topics in dynamics will remain with me as his legacy. He has been enthusiastic about the new ideas and methods that I have proposed over the years, and taught me to carry a healthy skepticism of numerical results and theoretical predictions. His research and teaching philosophy is an inspiration for me to strive for as a professional.

I am grateful to Prof. Mark Paul, Prof. Craig Woolsey, Prof. Sunghwan Jung, and Prof. Ishwar Puri for serving on my committee. A special thanks to Prof. Nicole Abaid for attending my final defense, and accepting to serve as a proxy. I benefited immensely from the constructive criticism and feedback on my research. My private communications with all of them have enlightened me, and they are the scientific minds I will always look up to. I would also like to thank all the professors and educators at Virginia Tech for teaching me the advanced subjects in Mathematics and Applied Mechanics.

I would like to thank the teachers of yesteryear who have shaped my early days as a student. My high school teachers Ms. Pompa Mandal, Mr. Siddhartha Bhattacharya, Mr. Sanjay Bhattacharya, Mr. Ambarnath Banerjee taught me the ropes of Geometry, Calculus, Statistics, Physics, respectively, and which lead to better appreciation of nonlinear dynamics. Mr. Nikhil Pandey deserves a special mention for being a mentor in my early days of high school Mathematics and Physics. I would also like to express my gratitude towards Prof. Ramesh-

war Dubey for educating me in geometric ways of thinking about classical mechanics. I am also thankful to my high school English teacher Miss Zabin who encouraged me to write regularly; this was a lesson to be relearned while writing this dissertation.

During my undergraduate years, educators who played significant roles in my formative years are Professors Saroj Mandal, Somnath Ghosh, Partha Bhattacharya, Gopinath Bhandari, Arup Guha Niyogi in the department of Civil Engineering at Jadavpur University. They inspired me to pursue interdisciplinary research even within the confines of a conventional program. I will be forever grateful to Professor Himadri Pai Majumdar in Physics and Applied Mathematics Unit at Indian Statistical Institute, Kolkata, for providing guidance as my undergraduate research mentor and advising me to pursue dynamical systems for my doctoral research. Their belief and confidence in me as a student remained crucial every step of the way.

The staff members of Engineering Mechanics Program (or formerly, Department of Engineering Science and Mechanics) were incredible in providing support in terms of resources and kind words during exams. I would like to thank Anne-Marie for all the cheerful conversations and caring words of support. I would also like to thank Amanda Covey, Sally Shrader, Melissa Nipper, and Lisa Smith for being accessible and helpful in all matters of logistics. I would also like to thank Tim Tomlin for his assistance with supercomputer, *Linux Computer Cluster*, throughout my graduate work. His general helpfulness and prompt responses made treading the world of computing that much easier and educating.

I would also like to thank Virginia Tech Cycling Team for introducing me to bike racing, and for giving a novice the opportunity to compete as a collegiate athlete. Traveling and racing with the team has made for some of the happy moments of attending Virginia Tech. I learned mental tenacity and fortitude as a cyclist which, without a doubt, helped in overcoming the downs of life and staying positive during trying times. I also learned the value of performance metric and deferred gratification that is essential for pursuing long term goals. I have much

more appreciation for the scale in plotting a cycling route's profile, sport aerodynamics, and the complexity of a 21 day stage race; I will remain a *total nerd* for the sport thanks to VT Cycling. I will forever cherish the friendship of Will Massey, Cora Olson, and Chrissy Esposito among others in the cycling community of Blacksburg.

I would like to thank the members of Ross Dynamics Lab who have been great lab mates over the years. Amir E. Bozorg Magham for helpful discussion during the early days of learning advanced dynamics, and Phanindra Tallapragada for advising me on subjects in Applied Mathematics. A very special thanks to Piyush Grover for serving as my research adviser during the internship at Mitsubishi Electric Research Laboratory (Cambridge, MA). The one-on-one discussions with him sharpened my attitude towards scientific curiosity and formed a substantial part of my research experience. I would also like to thank Peter Nolan, Isaac Yeaton, Gary Nave, and Thomas Battista for being good friends and providing moral support during proposal and final defense.

I would like to thank Saurabh Bisht, Arnab Gupta, Souvick Chatterjee for being friends through thick and thin, and helping me on multiple occasions. I am very grateful to Ganesh Balasubramanian for being a great friend and mentor since undergraduate, and I consider myself fortunate to have found a friend in him. His advice on a diverse array of life as graduate student and researcher has helped in many occasions.

My parents and sister have supported and encouraged me to pursue my dream of earning a Ph.D., even at the cost of sending me farthest from them. Their sacrifice and selfless love has been a motivation for me everyday. I strive to become better in my profession in the light of their teachings and blessings. I will remain grateful to them, forever.

Shibabrat Naik
Blacksburg, Virginia
September, 2016

Contents

- 1 Introduction** **3**
- 1.1 Phase space transport and escaping dynamics: 4
- 1.2 Attribution 6

- 2 Computational Method for Phase Space Transport with Applications to Lobe Dynamics and Rate of Escape** **8**
- 2.1 Introduction 8
- 2.2 Curve Area 11
- 2.3 Intersection Points and Lobes 12
- 2.4 Non-Transverse Intersections 21
- 2.5 Applications 28
- 2.6 Conclusion 39
- 2.7 Acknowledgements 41

- Appendix A** **44**
- A.1 Usage and outputs 44

3	Partial control of escaping dynamics: Application to ship roll motion and avoiding capsizing	46
3.1	Introduction	46
3.2	Description of ship roll motion	47
3.3	Partial control of escaping dynamics:	55
3.4	Application to ship rolling motion and capsizing	57
3.5	Conclusions	64
3.6	Acknowledgments	64
	Appendix B	67
B.1	Wave height parameter	67
B.2	Modeling wave excitation	67
B.3	Algorithm for obtaining initial set	68
4	Cylindrical manifolds and partial control: Application to coupled roll-pitch ship motion	70
4.1	Introduction	70
4.2	Description of coupled roll-pitch model	73
4.3	Invariant manifolds and ship capsizing	82
4.4	Partial control and ship capsizing	96
4.5	Discussion and Conclusions	103
4.6	Acknowledgments	104

Appendix C	110
C.1 The Linearized Hamiltonian system	110
C.2 Geometry of solutions near equilibria	116
C.3 Derivation of coupling constant	124
C.4 Derivation of differential correction term	126
C.5 Boundary of total energy on surface-of-section	129
5 Conclusions	131
5.1 Contributions and future directions	132
Complete list of references	135

List of Figures

2.1	(a) Pieces of the local unstable and stable manifolds, $W^u(p_i)$ (red) and $W^s(p_i)$ (green) of saddle fixed points $\{p_i\}$. (b) When the manifolds $W^u(p_i)$ and $W^s(p_i)$ are followed out on a global scale, they often intersect in primary intersection points $\{q_i\}$. These intersections allow one to define boundaries between regions $\{R_i\}$	9
2.2	(a) shows schematically lobes, pips and sips as defined for lobe dynamics. (b) shows example of two closed curves, C_1 and C_2 in \mathbb{R}^2 , oriented in counter-clockwise and clockwise direction which bound the two-dimensional subsets of \mathbb{R}^2 , A_1 and A_2 , respectively.	10
2.3	Example of closed curves with transverse intersection. (a) Green intersection points have $\rho(p_i) = 1$. Blue intersection points have $\rho(p_1) = -1$. (b) Intersection points of the same color belong to the same equivalency class. The arrows represent the one-to-one and onto relationship σ between the intersection points and the points joining the same equivalency class can either be a <i>knob</i> or <i>handle</i>	14
2.4	Schematic showing the slightly perturbed separatrices with different boundary intersection point(BIP). When the separatrices have near-tangent intersections, obtaining intersection points require inflating/deflating the points to avoid false lobes formed by the section of curve L and L'	21

2.5	Schematic view of the paths involved in the definition of Q_1 , Q_2 and Q_3 . . .	23
2.6	Showing the lobe area for different curve densifier option in OVP flow and PCR3BP. Along the x-axis the indices denote the following densifier options:1.-DENS 0, 2.-DENS 1 10, 3.-DENS 3 10, 4. -DENS 5 100, 5. without -DENS option which triggers the AUTO densifier. The y-axis is the average of the entraining and detraining lobes for the parameters $\epsilon = 0.1, \gamma = 0.5$ related to the flow. Using webplotDigitizer, we obtained lobe area from the analytical result in [18] which is $\mu(L) \approx 2\epsilon F(\gamma) \approx 0.2145$	28
2.7	(a) shows the unperturbed streamlines with periodic orbits in the region R_1 and free flow region R_2 and (b) shows the regions of interest R_1 and R_2 for studying transport in the OVP flow.The transport between the regions R_1 and R_2 can be explained and quantified in terms of the turnstile mechanism.	30
2.8	Computed unstable(red) and stable(green) manifolds of the hyperbolic fixed points for perturbation amplitude of $\epsilon = 0.1$.The manifolds are shown for qualitative comparison and a change in orientation for the γ values as predicted by Melnikov theory in Ref. [18].	31
2.9	Showing the separatrix with q as a bip and its backward evolution with the pre-images of q as bips. The region R_1 is the transparent layer on the pre-images.	33
2.10	Showing the <i>turnstile</i> s in red(entraining lobe labeled $L_{1,2}(1)$) and cyan(detraining lobe labeled $L_{2,1}(1)$) for the OVP flow with parameters $\epsilon = 0.1, \gamma = 0.5$. The zoom-in view shows the intersection regions that are used in quantifying the transport.	33
2.11	Output of Lober identifying the lobes, pips(filled black circle) and the separatrix(thick black line). For both the cases, $\epsilon = 0.5$	34

2.12	Fig. (a) Shows the area of lobes for $\epsilon = 0.1$ and different γ values. This agrees well with Fig.9 in [18] which compares the brute force method of lobe area calculations with Melnikov function. Fig. (b) Shows the normalized fluid volume for increasing iterates of the perturbation period.	35
2.13	Realms of possible motion shown in white and energetically inaccessible region in grey for capsizes/critical energy, $E_c = 0.25$ and $R = 1.6$. Poincaré S-O-S defined by U_1 of the energy manifold.	37
2.14	Showing the periodic orbit and corresponding stable manifold as transition tube for trajectory (red) escaping to the capsizes realm and non-transit trajectory (blue) that remains bounded.	38
2.15	Tube manifolds of right and left critical points in (x, y, v_y) subspace of the 4D phase space for energy, $\Delta e = 0.00307$ above critical energy.	39
3.2.1	Schematic of the degrees of freedom of a ship in 4.1(a) and 4.1(b) illustrates the wave characteristics. Adapted from [42].	48
3.2.2	The restoring moment, $GZ(\phi)$, for the ship <i>Edith Terkol</i> is shown in (a) and the roll angle of vanishing stability, ϕ_v denotes the roll angle when the restoring moment goes to zero. The potential energy, $V(\phi)$, that underlies the restoring moment and the roll angle of vanishing stability is shown in (b).	50

3.2.3 Non-capsize basin in the phase space of roll model where the gray region denotes initial conditions that do not lead to capsize during $1 \bar{T}$ (nondimensional wave period) for wave heights $H = 3.28$ m, $H = 4.92$ m, and $H = 9.84$ m in Fig. 3.3(a)- 3.3(c). The parameters are for the ship *Edith Terkol* and it should be noted that in Fig. 3.2.3, the nondimensional wave period corresponds to beam seas ($\chi = 90$ deg), so the ship's forward speed has no effect on the encounter frequency which is equal to the wave frequency ([42, chap.2]) in beam seas. This means the non-capsize basin is for waves of different heights are incident on the ship at same encounter frequency. 52

3.2.4 (a) Pre-image of the left (green) and right (magenta) boundaries for a wave height of $H = 9.84$ m and the non-capsize basin shown as the gray region.
 (b) Invariant manifolds for the unforced form of roll model (3.2.7) where the red curves denote the unstable and blue denotes the stable manifolds of the saddle p_{\pm} , respectively. Due to damping, stable and unstable manifolds of the saddles are not connected by a heteroclinic orbit and instead unstable manifolds connect to the center sink at p_0 54

3.3.1 Partial control applied to slope-3 tent map with $Q = [-1.5, 1.5]$ as the region we want to keep the admissible trajectory. Figs. (a), (b), and (c) shows the first 10 iterations, the admissible disturbance that acts at each iteration and the admissible control that is applied at each iteration, and the obtained admissible trajectory for 100 iterations, respectively, for $\xi_{\max} = 2$, $u_{\max} = 1$. Figs. (d), (f), and (e) shows the same for $\xi_{\max} = 2/3$, $u_{\max} = 1/3$. Figs. (a) and (d) show Q as the grey closed set on \mathbb{R} , and the cyan dots are the safe set, S which is either $\{-1, 1\}$ or $\{-1 - 1/3, -1 + 1/3, 1 - 1/3, 1 + 1/3\}$ for the two cases, respectively. The black dot denote iterates of the tent map while the red dots denote points after disturbance has acted on the iterate. The admissible trajectory is shown as green dots which are in S and hence in Q , and obtained using control that is always less than the disturbance as shown in Figs. (b) and (e).

58

3.4.1 Fig. 3.1(a) shows the initial set (also referred in [41] as the safe basin) under the wave forcing for 1 T_e , $H = 4.94$ m. Final safe set (blue region) shown here denote the initial conditions that are for a control upper bound, $u_{\max} = 0.096988$ and disturbance, $\xi_{\max} = 0.15314$ with safe ratio, $\rho = 0.63$. The grid resolution was 1001×1001 and the wave height $H = 4.92$ m. The control upper bound is very close to the minimum value of $u_0^{min} = 0.096477$ below which the safe set vanishes.

60

3.4.2 Fig. 3.2(a) shows the initial set, Q (as blue region), and the controlled trajectory (marked as black x). Q is the set of initial condition that don't lead to capsize over 1 period of the regular sea of 4.94 m wave height. The noise is assumed to be uniformly distributed with upper bound of $\xi_{\max} = 0.15314$ and acts at the end of every period as shown (in red) in Fig. 3.2(b).

61

3.4.3 Ocean wave spectrum given by Eqn. (4.3.4) that is used to generate the continuous wave forcing in rough seas.	62
3.4.4 The wave energy spectrum of the rough sea used in the computations. A sample ensemble of trajectories for random sea waves of significant height, $H = 4.94\text{m}$	62
3.4.5 Safe set for rough seas of wave height $H_s = 4.94$ m while the partial control time, $t_{pc} = 2$ secs obtained for a safe ratio of 0.925	63
3.4.6 Figures showing the safe set and asymptotic safe set which is almost equal to the safe set.	63
B.3.1 Showing the algorithm 2 as a schematic for computing the initial set Q.	69
4.2.1 Schematic adapted from [66] illustrating the wave characteristics relative to ship motion using (x, y, z) as the body-fixed reference frame.	74
4.2.2 (a) Shows the effective potential energy with an upright ship in the region that corresponds to bounded motion inside the well and a capsized ship in the region that corresponds to unbounded motion. The total energy of the system can be considered as fixing a height of this potential well and shown here as contour lines of $0.5E_e, E_e, 2E_e, 4E_e$. (b) Shows the total energy as contour lines on the configuration space (x, y) for different values above and below the critical energy E_e	76

4.2.3 Poincaré surface-of-section (SOS) of the energy surface, showing orbits of the return map for different energy values. In the absence of damping and wave forcing, the system conserves energy and for energy below the critical value, E_e , all the trajectories intersect the SOS (4.2.13) as shown in (a) and (b) for $e = 0.22$ and $e = 0.25$. When the energy is above the critical value, trajectories leading to capsizes do not intersect the surface (4.2.13) any longer and hence less return orbits are shown in (c) 79

4.2.4 (a), (b), and (c) show the Hill's region for $e < E_e$, $e = E_e$, and $e > E_e$ where E_e denotes the critical energy. The white region is the energetically accessible region bounded by the zero velocity curve and while the gray region is the energetically forbidden realm where kinetic energy is negative and motion is impossible. 80

4.3.1 Schematic of the globalization of invariant manifolds that computes an approximation of the two branches of the unstable (W_{\pm}^u) and stable (W_{\pm}^s) manifolds of a periodic orbit. The two branches are computed using the positive and negative directions of the eigenvectors $e^u(t_0)$ and $e^s(t_0)$, respectively, after an initial displacement of small magnitude from X_0 to X_1 . Then, the unstable (stable) manifold is computed using successive forward (backward) iterate of the map P which marches along the half manifold. 89

4.3.2 Shows the Poincaré surface-of-section, U_1 (4.2.13), as the magenta plane and the stable manifold of right saddle is shown as the cyan surface for a given energy e . The manifold is codimension-1 in the phase space of \mathbb{R}^4 with geometry $\mathbb{R}^1 \times \mathbb{S}^1$ that is cylindrical, and hence the name *tube manifold*. The stable manifold of a saddle up to its first intersection with U_1 is the pathway that leads to imminent capsizing. The trajectory that leads to escape from the potential well and corresponds to the imminent capsizing of a ship, for example the red trajectory, lies in the interior of the tube. Similarly, a trajectory that stays inside the potential well and corresponds to an upright ship lies outside the tube. These example trajectories are shown in the $x - y - v_y$ space for a given energy e and also as projection in the configuration space. 90

4.3.3 (a) Shows the tubes that lead to imminent capsizing to left and right, and the SOS, U_1 (4.2.13), is shown as the magenta plane. These are the stable manifolds of the left and right saddles, and are cylindrical, that is $\mathbb{R}^1 \times \mathbb{S}^1$ geometry. (b) Shows the intersection of the stable manifolds with the SOS U_1 as regions with green boundary, and the black boundary corresponds to intersection of the energy surface (4.2.12) with the SOS U_1 . where the boundary of the region leading to imminent capsizing is the intersection of the stable manifolds with the SOS. 91

4.3.4 (a) Shows the wave energy spectrum, called the *Pierson-Moskowitz*, for different significant wave height. The peak energy is centered at the same frequency and the max energy increases with increasing significant wave height. This is used to sample the wave forcing for simulating a ship rolling and pitching in rough sea. (b) Shows 10 samples of forcing, $f_x(t)$ in beam sea of significant wave height, $H_s = 4.92$ m and the mean of 10^5 ensembles as the zero line which demonstrates the underlying stochastic process has zero mean. 93

4.3.5 (a) Shows the distribution of capsizing probability as the contour plot with region that does not lead to capsizing, that is starting conditions with 0 probability of imminent capsizing, shown as grey region for $H_s = 4.92$ m and $\Delta E = 0.003$.	
(b) Shows the same for $H_s = 9.84$ m and $\Delta E = 0.003$. In both figures, the black boundary is the intersection of the energy ellipsoid (see Appendix C.5 for details) with the Poincaré SOS and the magenta curve is the boundary of the region that has capsizing probability greater than 0.05. In absence of random forcing, the boundary of the region with 1 probability is given by the tube intersection, shown as red curve. The dotted lines denote the cross-section of the distribution at a constant v_y , and shown at the top of the contour plot. The red bar of sharp unit probability corresponds to the tube intersection at its maximum width; while the spread out distribution corresponds to the dotted lines with different v_y values.	95
4.3.6 (a) Shows the distribution of capsizing probability as the contour plot with region that does not lead to capsizing, that is starting conditions with 0 probability of imminent capsizing, shown as grey region for $H_s = 4.92$ m and $\Delta E = 0.03$.	
(b) Shows the same for $H_s = 9.84$ m and $\Delta E = 0.03$	96
4.4.1 Schematic of a safe point \mathbf{q} in the final safe set, S . \mathbf{q} is mapped to $f(\mathbf{q})$ and the disturbance, $\boldsymbol{\xi}_0$ takes it to the boundary of the disk which is at most \mathbf{u}_0 distance	98
4.4.2 Shows the region Q and its image under the map f (4.4.5) in (a) and (b), respectively. The same is shown for the map f (4.4.6) in (c) and (d), respectively. These two approaches of defining the map f form the basis of obtaining safe sets in the partial control framework.	101

4.4.3	Using the safe set sculpting algorithm, we compute sets in the region Q (shown in (c)) and the map f (4.4.6) for the disturbance upper bound of $\xi_0 = 0.1$ and control upper bounds of $u_0 = 0.061$ (shown in (a)) and $u_0 = 0.1$ (shown in (b)). The red and green disks are the size of disturbance and control, respectively, which are used in the safe set sculpting algorithm and shown here for scale. When obtaining a <i>partially controlled</i> trajectory, we sample values ξ_n from $[-\xi_0, \xi_0]$ and obtain \mathbf{u}_n by computing distance from the safe set. Safe set in Fig.(a) corresponds to the minimum control (in the sense of upper bound) that is needed for the given disturbance, and below $u_0 = 0.061$ the safe set does not exist. This is a critical value for partial control, however, this approach guarantees safety with $u_0 < \xi_0$ <i>ad infinitum</i>	102
C.2.1	The projection onto the $\eta - \xi$ plane of orbits near the equilibrium point; the $\eta - \xi$ axis is rotated by 45° . (a) Shows the equilibrium region, \mathcal{R} , is bounded by the thick hyperbolic segments at top and bottom and the dotted vertical segments at left and right. At the origin is the periodic orbit in \mathcal{R} . The thick lines with arrows pointing toward or away from the origin are trajectories asymptotically winding onto the periodic orbit. (b) Shows four additional trajectories. The label T_{ij} denotes the path of a particle which entered \mathcal{R} through n_i and exited through n_j . Two transit orbits, T_{12} and T_{21} , and two non-transit orbits, T_{11} and T_{22} , are shown.	122
C.3.1	Schematic of a solid rectangular parallelepiped that represents a ship	125

List of Tables

2.1	Functions ρ and σ for the intersection points between the curves of Fig. 2.3. There are two equivalency classes for this example.	15
2.2	Function $A_{C_1}^+$ for the intersection points between the curves of Fig. 2.3. The lines and columns correspond respectively to the first and second argument of $A_{C_1}^+$	15
2.3	Function $A_{C_2}^-$ for the intersection points between the curves of Fig. 2.3. The lines and columns correspond respectively to the first and second argument of $A_{C_2}^-$	15
2.4	Function γ for the intersection points between the curves of Fig. 2.3. The lines and columns correspond respectively to the first and second argument of γ	16
2.5	Percentage of trajectories escaping via left/right stable tube that entered via left and right unstable tubes.	40

Preface

This dissertation was submitted to the Virginia Polytechnic Institute and State University on 23rd September 2016, as a partial fulfillment of the requirements for the degree of Doctor of Philosophy in Engineering Mechanics. This dissertation is meant to serve as a research report on geometric methods for phase space transport in dynamical systems, and prediction and control of escaping dynamics. The approach is to present the mathematical ideas by application to archetypical problems from mechanics and engineering, and present numerical demonstration of the geometric methods.

The overall superstructure of the dissertation is divided into three core chapters that are kept independent to facilitate publication and some of the content has been submitted to peer-reviewed journals in slightly modified form. A general introduction to the dissertation's theme is in the Chapter 1, and the summary of contribution with future directions is presented in the Chapter 5. The remaining chapters are as follows:

- Chapter 2 has been submitted as S. Naik, F. Lekien, S. D. Ross, Computational Method for Phase Space Transport with Applications to Lobe Dynamics and Rate of Escape, to *Regular and chaotic dynamics*
- Chapter 3 is in preparation as S. Naik, S. D. Ross, Partial control of escaping dynamics: Application to ship roll motion and avoiding capsizing, for submission to *Proceedings of Royal Society: A*

- Chapter 4 has been submitted as S. Naik, S. D. Ross, Geometry of Escaping Dynamics in Nonlinear Ship Motion, to *Communications in Nonlinear Science and Numerical Simulation*

Chapter 1

Introduction

“A mathematician, like a painter or poet, is a maker of patterns. If his patterns are more permanent than theirs, it is because they are made with ideas.” – G. H. Hardy, A Mathematician’s Apology

In applied mathematics, dynamical systems is concerned with understanding motion given by a differential equation

$$\dot{\mathbf{x}} = \mathbf{v}(\mathbf{x}, t) \tag{1.1}$$

where, $\dot{(\)}$ denotes time derivative, $\mathbf{x} \in \mathbb{R}^n$ are the states or phase space co-ordinates of the system, $\mathbf{v} \in \mathbb{R}^n$ are the known functions expressed in terms of the states \mathbf{x} and time t , and also known as the *vector field*. This form of representing the time evolution of states arises in a myriad of disciplines in physical sciences and engineering, when using iterated maps or ordinary differential equations (ODE) or partial differential equations (PDE) as mathematical models, or experiments for observing physical phenomena. In the case of numerical solution of PDE or experimental data, the smooth representation of $\mathbf{v}(\mathbf{x}, t)$ can be obtained by interpolation of the snapshots of vector field. In general, the vector field is

given by a nonlinear equation and the goal is to understand how the time evolution of the states, and thus enabling prediction and control. To study such evolution, we resort to the abstraction of *phase space* where the states are chosen as the coordinates and we observe the time evolution as global behavior of the solutions.

As nonlinear systems exhibit *finite escape time*, *multiple equilibria*, and *multiple modes of behavior* [1], characterizing the global dynamics can become complicated and cumbersome task. However, with the aid of organizing structures that exist in the phase space, or extended phase space for non-autonomous systems, we can categorize the trajectories based on the global behavior [2, 3, 4]. Thus, circumventing the exhaustive search for trajectories with different fates. This approach also enhances the efficiency of parametric study using numerical solution, and provides guiding assumptions for analytical derivations. Thus, in dynamical systems approach of understanding motion, the objective is to identify the geometric structures and describe conditions of phase space transport in terms of these structures.

To further elucidate these ideas, we adopt *simple* clean problems that are related to generic models of physical phenomena and components that arise in practical engineering systems [5]. In this research report, we adopt the classical problem of ship capsize that fits into this framework of study.

1.1 Phase space transport and escaping dynamics:

The geometric methods of phase space transport deals with local and global behavior of *transit orbits*, *invariant manifolds* of unstable periodic orbit which separate motions with distinct dynamical behavior.

Chaotic transport. In this context, the goal for studying chaos enhanced transport is to understand, forecast, and control the evolution and motion of boundaries that act as barriers to the phase space volume [6]. These boundaries are defined using the perturbed manifolds

associated with the saddles in forward time, that is $t \rightarrow \infty$, and are called unstable manifolds and those in backward time, that is $t \rightarrow -\infty$, are called stable manifolds. The regions of the phase space that lead to crossing of the barriers are formed by segments of unstable and stable manifolds of hyperbolic fixed points, p_{\pm} , called *lobes* [7]. The lobes form atoms of transport in the sense that global phase space transport can be explained by considering a few basic forms of lobes and their forward and backward iterates. However, from the perspective of transport and its rate, we need longer integration times to resolve the manifolds as they are infinitely stretched and folded due to the hyperbolic nature of the fixed points [6, 4]. This generates a chaotic tangle of manifolds, called homoclinic/heteroclinic tangle, that requires understanding of the geometry of the manifolds and the regions bounded between the segments. This was formalized in Ref. [8, 7] as lobe dynamics which provided a language to discuss global transport in phase space and computation of transport properties like residence time and exit time distribution, entrainment and detrainment rates, and the flux across a boundary.

Escape from potential well. This is a more general problem and appears across various disciplines with the guiding approach being the crossing of transition state [9, 10, 11] or periodic orbit in the bottleneck region of a potential well. We apply this framework of understanding critical events to the classical problem of ship dynamics and capsizing. The motion of a marine vessel in ocean have received considerable attention from the perspective of nonlinear dynamics and control systems for quite a while now [12, 13, 14, 15, 15]. This has two fold purpose; namely the mechanics involved in describing the motion, and control of undesirable behavior. The former purpose serves to explore dynamical features of a nonlinear system as in Ref. [16], the later purpose is served in developing control approaches and engineering devices as can be found in Ref. [17].

Effect of noise on escaping dynamics. In case of open dynamical systems, the environment and external constraints imposed on the system fluctuate, in general, more or less strongly. Rapid random fluctuations are always present in natural and engineering systems

and their amplitude is not necessarily small. In laboratory experiments, the experimenter will of course try to minimize the effect of random perturbations, we call these *noise* following common usage, though it is impossible to eliminate noise completely. Hence, random fluctuations are ubiquitous in the external constraints of open systems. Furthermore, systems near the onset of instabilities are sensitive to random noise just because instability causes even the smallest of fluctuations to grow with time rather than decay away.

1.2 Attribution

This dissertation is in form of three manuscripts that are in preparation for submission in peer reviewed journals. The title of this dissertation encapsulates the common theme of these chapters, but an attempt has been made to limit the redundancy of description. In this section, I declare the roles of co-authors and attribute the contributions made for individual chapters.

Chapter 2

S. Naik, F. Lekien, S. D. Ross, Computational Method for Phase Space Transport with Applications to Lobe Dynamics and Rate of Escape, Submitted to *Regular and chaotic dynamics*

My main contributions to this paper are helping with finishing of the draft, to produce the computational results, coming up application problems to test the software *Lober*, comparing the accuracy of computation with literature and previously established results, to produce the results of all LCS computations. Dr. Lekien and Dr. Ross developed the theory, proved the theorems therein, generated the code *Lober* in C, and wrote the first draft.

Chapter 3

S. Naik, S. D. Ross, Partial control of escaping dynamics: Application to ship roll motion and avoiding capsizing, In preparation for submission to *Proceedings of Royal Society: A*

I did the majority of writing, proposed the model problem, obtained the computational results on invariant manifolds and safe sets, proposed the application of partial control and formulated the problem as escaping dynamics. Dr. Ross edited the manuscript and provided feedback, helped with parameter estimation, discussed directions of investigation.

Chapter 4

S. Naik, S. D. Ross, Cylindrical manifolds and partial control: Application to coupled roll-pitch ship motion, Submitted to *Communications in Nonlinear Science and Numerical Simulation*

I did the editing, derived the analytical results, proposed the application of partial control and obtained the computational results on safe sets. Dr. Ross wrote the first draft of the manuscript, and performed computations of cylindrical manifolds.

Chapter 2

Computational Method for Phase Space Transport with Applications to Lobe Dynamics and Rate of Escape

In collaboration with Francois Lekien and Shane D. Ross

2.1 Introduction

Lobe dynamics, introduced in [18], is a geometric method for determining the transport in maps, typically two-dimensional, but there have been attempts at extension to higher dimensions ([19, 20]). Although chaotic transport in fluid was the initial inspiration for this theory([18]), it has been applied to diverse transport problems which include dynamical astronomy [21], wake behind a cylinder [22], oceanic flow in geophysics [23]. Following the developments in [8, 24], lobe dynamics states that the two-dimensional phase space M of the Poincaré map f can be partitioned into certain regions, with boundaries consisting of parts of the boundary of M (which may be at infinity) and/or segments of stable and unstable

invariant manifolds of hyperbolic fixed points, $p_i, i = 1, \dots, N$, as shown schematically in Fig. 2.1(a). When the manifolds $W^u(p_i)$ and $W^s(p_i)$ are followed out on a global scale, they often intersect in primary intersection points $\{q_i\}$. These intersections allow one to define boundaries between regions $\{R_i\}$, as illustrated in Fig. 2.1(b). Moreover, the transport between regions of phase space can be completely described by the dynamical evolution of small subregions of phase space, “lobes” enclosed by segments of the stable and unstable manifolds as defined below.

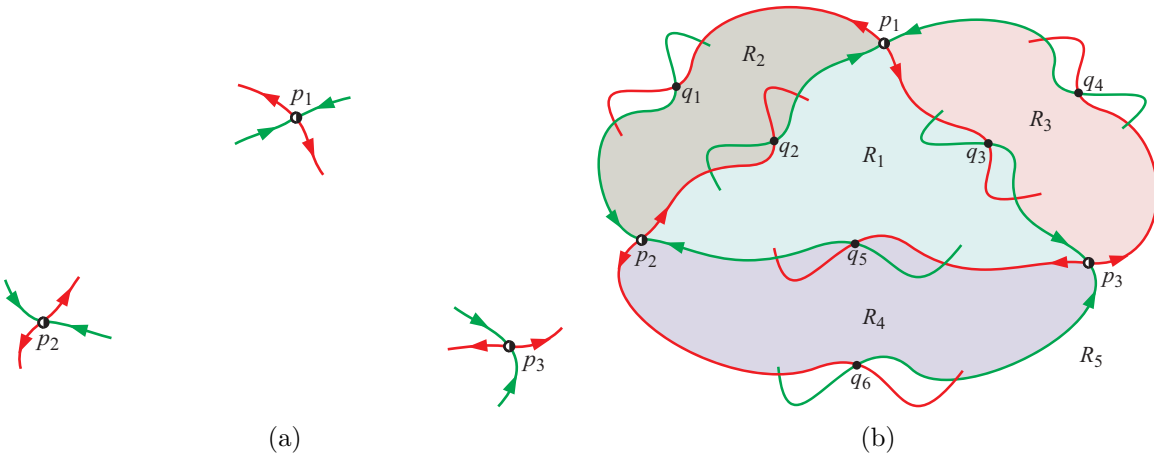


Figure 2.1: (a) Pieces of the local unstable and stable manifolds, $W^u(p_i)$ (red) and $W^s(p_i)$ (green) of saddle fixed points $\{p_i\}$. (b) When the manifolds $W^u(p_i)$ and $W^s(p_i)$ are followed out on a global scale, they often intersect in primary intersection points $\{q_i\}$. These intersections allow one to define boundaries between regions $\{R_i\}$.

Classically, invariant manifolds of hyperbolic fixed points are computed for as long as possible and lobes are extracted from the two curves [18, 21]. However, it is possible to get more lobes, hence compute transport for a much longer period of time, by integrating separatrices directly, particularly in the complex case of multiple, self-intersecting, lobes [21]. In this approach, the notion of pips and sips are not suitable, thus we propose a generalization of definition of lobes for two intersecting closed curves. When applying lobe dynamics to transport problems, it is of eventual interest to quantify volume of phase space M that crosses the boundary with higher iterates of the Poincarè map f . This is typically achieved in multiple ways:

- Distribute test points inside the phase space region of interest and computing the iterate/s required for each to escape. This will also need to take care of the re-entrainment due to the underlying turnstile mechanism [8, 25, 3].
- Constructing a functional of the nonlinear system of vector field which measures area between the manifolds as parametrized by time. This is a semi-analytical approach and remains valid near small perturbations, for example Melnikov method for mixing, stirring, optimal phase space flux in [26, 27, 28, 29], and action-integral method.
- Following the boundaries of separatrices/manifolds as it is evolved in time and compute set operations with its pre-images/images. This is a more general but surely a difficult approach due to the stretching and folding of the curves that are involved in such computations [30, 31, 32].

We consider two closed curves C_1 and C_2 in \mathbb{R}^2 , both oriented in a counter-clockwise direction which bound the two-dimensional subsets of \mathbb{R}^2 , A_1 and A_2 , respectively (see Fig. 2.2(b)). We want to determine the area of the lobes (i.e., the area of $A_1 \setminus A_2$ and $A_2 \setminus A_1$) defined by these two curves.

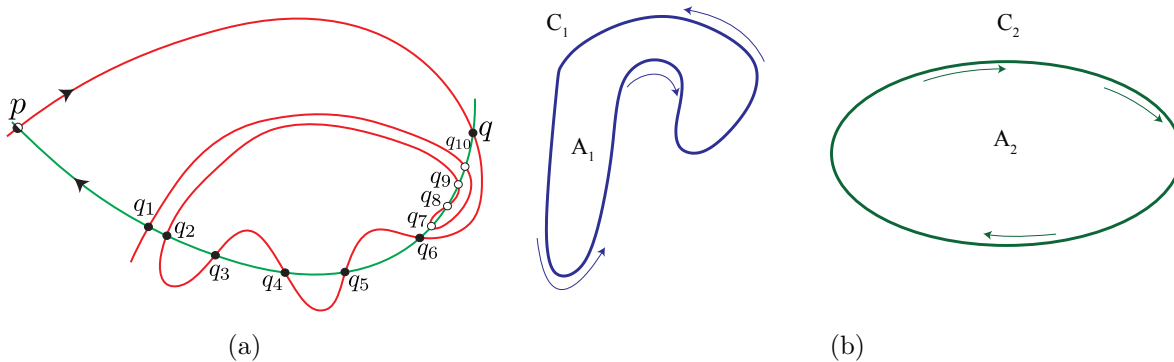


Figure 2.2: (a) shows schematically lobes, pips and sips as defined for lobe dynamics. (b) shows example of two closed curves, C_1 and C_2 in \mathbb{R}^2 , oriented in counter-clockwise and clockwise direction which bound the two-dimensional subsets of \mathbb{R}^2 , A_1 and A_2 , respectively.

In the §2.2-2.3, we derive the theory and numerical methods to separate the intersection points between the two curves into equivalence classes and derive the area of the lobes

defined by the two curves. In §2.4, we present an alternate method that can be used when portions of the two curves have non-transverse intersections, which arises in the case of an iterated separatrix. In §2.5, the results are applied to three examples of interest in the dynamical systems literature. We apply the numerical methods to the planar restricted three body problem(PCR3BP) in celestial mechanics, oscillating vortex pair flow as a model of chaotic fluid transport. Finally, we study the escape from a potential well, by considering the Poincaré surface-of-section and *tube dynamics*.

2.2 Curve Area

2.2.1 One-Dimensional Integrals for Areas

Let us define $A_1 = \text{int}(C_1)$ and $A_2 = \text{int}(C_2)$ as the area enclosed by C_1 and C_2 , respectively and denote this using the standard Lebesgue measure for μ in \mathbb{R}^2 as $[A] = \mu(A)$. The area of each region can be computed as:

$$[A_i] = \iint_{A_i} dA = \frac{1}{2} \oint_{C_i} ydx - xdy , \quad (2.1)$$

by applying Green's theorem to the vector field

$$\bar{f} = \begin{pmatrix} x \\ y \end{pmatrix} \implies \nabla \cdot \bar{f} = 2 . \quad (2.2)$$

Eq. (2.1) allows us to reduce the computation of the area of a complicated region to a one-dimensional integral over its boundary. Notice that the sign of the integral is to be reversed if the curves are oriented clockwise. Our hypothesis stating that the curves are oriented in

a counter-clockwise direction is equivalent to

$$\forall i : \oint_{C_i} ydx - xdy \geq 0. \quad (2.3)$$

2.2.2 Numerical Methods

We assume that the curves C_1 and C_2 are given in terms of a sequence of points (x_i, y_i) . We want an exact evaluation of the integral in Eq. (2.1) for piecewise polygonal curves. By defining

$$\begin{cases} x = x_i + t(x_{i+1} - x_i) , \\ y = y_i + t(y_{i+1} - y_i) , \end{cases} \quad (2.4)$$

we have

$$\int_{x_i, y_i}^{x_{i+1}, y_{i+1}} ydx - xdy = \int_0^1 (y_i x_{i+1} - x_i y_{i+1}) dt = y_i x_{i+1} - x_i y_{i+1} . \quad (2.5)$$

As a result the exact value of the contour integral for a polygon is given by

$$[A_i] = \frac{1}{2} \oint_{C_i} ydx - xdy = \frac{1}{2} \sum_i (y_i x_{i+1} - x_i y_{i+1}) . \quad (2.6)$$

2.3 Intersection Points and Lobes

Lobe dynamics is based on the geometry of a stable, W^s and an unstable, W^u invariant manifold of (perhaps one/two different) hyperbolic fixed points, their intersection points and areas enclosed by the pieces of the invariant manifolds. As defined in [18] and shown in Fig. 2.2(a), $q_1 \in W^u \cap W^s$ is a *primary intersection point* (pip) if the segment $W^u[p_{-, \epsilon}, q_1]$ and $W^s[p_{+, \epsilon}, q_1]$ intersects only at q_1 , and is a *secondary intersection point* (sip) if there are other intersection points. If q_1 and q_2 are two adjacent pips, then the area enclosed by the segments $W^u[q_2, q_1]$ and $W^s[q_1, q_2]$ is called *lobe*. Thus, a formal definition of pips

and *sips* is not possible for closed curves without a reference point (e.g., a hyperbolic fixed point/s). Instead, for intersecting curves C_1 and C_2 (see Fig. 2.3(a)) encountered in phase space transport problems, we separate the set of intersection points between the two curves into classes of equivalence. For two curves corresponding to the invariant manifolds of a hyperbolic fixed point, each class of equivalence corresponds exactly to the two *pips* and associated *sips* of a lobe, as defined by [8].

2.3.1 Intersection Points

In this section, we assume that there are only transverse intersections of the curves. A numerical algorithm for efficiently computing the intersection points is presented below. The two curves are closed and the intersections are transverse, so the number of intersection points must be even. We compute the $2N$ intersection points p_i between the two curves C_1 and C_2 . The unit tangent vector to the curve C_j at point p_i is denoted $\mathbf{1}_j(p_i)$. For each intersection point, p_i , we define

$$\rho(p_i) = \frac{\mathbf{1}_1(p_i) \times \mathbf{1}_2(p_i)}{\|\mathbf{1}_1(p_i) \times \mathbf{1}_2(p_i)\|} . \quad (2.7)$$

Notice that the intersections are transverse, so the denominator of Eq. (2.7) is always non-zero and $\rho(p_i) \in \{-1, +1\}$. Fig. 2.3 gives two examples of curves, their intersection points and the value of ρ for each point.

2.3.2 Classes of Intersection Points

The segments of curve between intersection points are most important to our computation, so we define $C_1^+[p_i, p_j]$ and $C_2^+[p_i, p_j]$ as the counter-clockwise segments of respectively C_1 and C_2 between the points p_i and p_j . Similarly, $C_1^-[p_i, p_j]$ and $C_2^-[p_i, p_j]$ are the clockwise segments of respectively C_1 and C_2 between the points p_i and p_j . We define the positive and

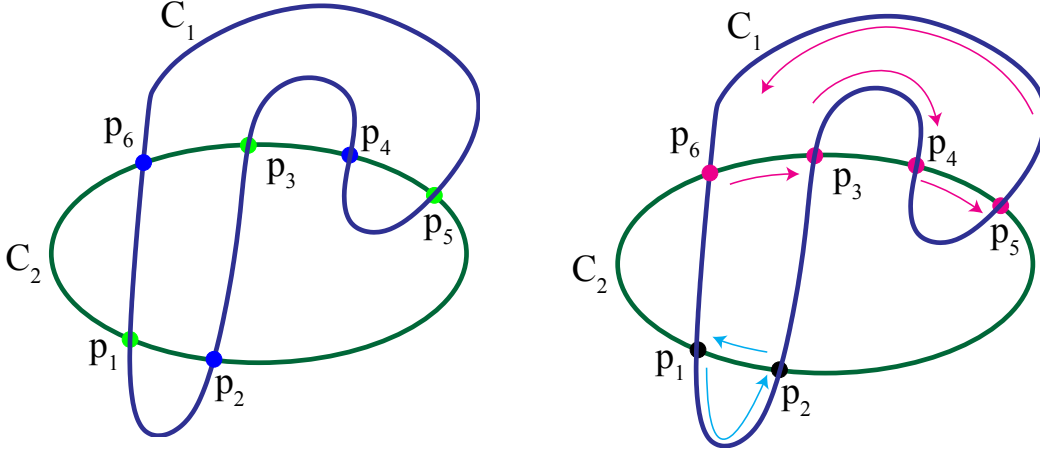


Figure 2.3: Example of closed curves with transverse intersection. (a) Green intersection points have $\rho(p_i) = 1$. Blue intersection points have $\rho(p_i) = -1$. (b) Intersection points of the same color belong to the same equivalency class. The arrows represent the one-to-one and onto relationship σ between the intersection points and the points joining the same equivalency class can either be a *knob* or *handle*.

negative adjacency on C_1 by

$$A_{C_1}^{\pm}(p_i, p_j) = \begin{cases} 1 & \text{if } \forall 1 \leq k \leq 2N : k \neq i \text{ and } k \neq j \implies p_k \notin C_1^{\pm}[p_i, p_j] \\ 0 & \text{otherwise} \end{cases} . \quad (2.8)$$

and the adjacency on C_2 as

$$A_{C_2}^{\pm}(p_i, p_j) = \begin{cases} 1 & \text{if } \forall 1 \leq k \leq 2N : k \neq i \text{ and } k \neq j \implies p_k \notin C_2^{\pm}[p_i, p_j] \\ 0 & \text{otherwise} \end{cases} . \quad (2.9)$$

The visual interpretation of adjacency is that when traversing a curve in CCW/CW(positive or negative sense) direction, the point p_j with adjacency value of 1 is the point next to the point p_i .

The objective of this section is to determine a generalized notion of a lobe. Intuitively, lobes are bounded by “segments of the curves C_1 and C_2 turning in opposite directions on each

	$\rho(p)$	$\sigma(p)$	Class
p_1	+1	p_2	1
p_2	-1	p_1	1
p_3	+1	p_4	2
p_4	-1	p_5	2
p_5	+1	p_6	2
p_6	-1	p_3	2

Table 2.1: Functions ρ and σ for the intersection points between the curves of Fig. 2.3. There are two equivalency classes for this example.

$A_{C_1}^+(\downarrow, \rightarrow)$	p_1	p_2	p_3	p_4	p_5	p_6
p_1	0	1	0	0	0	0
p_2	0	0	1	0	0	0
p_3	0	0	0	1	0	0
p_4	0	0	0	0	1	0
p_5	0	0	0	0	0	1
p_6	1	0	0	0	0	0

Table 2.2: Function $A_{C_1}^+$ for the intersection points between the curves of Fig. 2.3. The lines and columns correspond respectively to the first and second argument of $A_{C_1}^+$.

curve". We formalize this idea by defining the signed adjacency

$$\gamma(p_i, p_j) = \frac{\rho(p_i) + 1}{2} A_{C_1}^+(p_i, p_j) - \frac{\rho(p_i) - 1}{2} A_{C_2}^-(p_i, p_j). \quad (2.10)$$

Table 2.3.2, 2.3.2 and 2.3.2 show the value of the functions $A_{C_1}^+$, $A_{C_2}^-$ and γ for the example intersecting curves of Fig. 2.3.

$A_{C_2}^-(\downarrow, \rightarrow)$	p_1	p_2	p_3	p_4	p_5	p_6
p_1	0	0	0	0	0	1
p_2	1	0	0	0	0	0
p_3	0	0	0	1	0	0
p_4	0	0	0	0	1	0
p_5	0	1	0	0	0	0
p_6	0	0	1	0	0	0

Table 2.3: Function $A_{C_2}^-$ for the intersection points between the curves of Fig. 2.3. The lines and columns correspond respectively to the first and second argument of $A_{C_2}^-$.

$\gamma (\downarrow, \rightarrow)$	p_1	p_2	p_3	p_4	p_5	p_6
p_1	0	1	0	0	0	0
p_2	1	0	0	0	0	0
p_3	0	0	0	1	0	0
p_4	0	0	0	0	1	0
p_5	0	0	0	0	0	1
p_6	0	0	1	0	0	0

Table 2.4: Function γ for the intersection points between the curves of Fig. 2.3. The lines and columns correspond respectively to the first and second argument of γ .

In order to separate the intersection points in disjoint classes, we define an equivalency relation between the intersection points by

Definition 2.3.1 $p_i \sim p_j$ iff there exists a sequence of K intersection points p_{α_k} such that

$$\left\{ \begin{array}{l} p_{\alpha_1} = p_i , \\ p_{\alpha_K} = p_j , \\ \prod_{k=1}^{K-1} \gamma(p_k, p_{k+1}) = 1 . \end{array} \right. \quad (2.11)$$

We have the following properties

Theorem 2.3.1 (Reflexivity of \sim)

$$\forall i : p_i \sim p_i , \quad (2.12)$$

Proof Letting $K = 1$ and $\alpha_1 = i$ in Eq. (2.11) gives the desired result. \square

Theorem 2.3.2 (Symmetry of \sim)

$$\forall i, j : p_i \sim p_j \implies p_j \sim p_i , \quad (2.13)$$

Proof We notice that for any intersection point p_i , there is one and only one intersection

point p_j satisfying $A_{C_1}^+(p_i, p_j) = 1$. This is a consequence of the fact that the intersections are transverse and that there are not any self-intersections. There must be at least one segment of the curve C_1 leaving p_i (based on a counter-clockwise orientation of C_1). If there was more than one segment leaving this point, the curve C_1 would self-intersect. Similarly, there is also one and only one intersection point satisfying $A_{C_2}^-(p_i, p_k) = 1$. Since $\rho(p_i) \in \{-1, 1\}$, there is only one intersection point p_q ($q = j$ or k) such that $\gamma(p_i, p_q) = 1$. We define $\sigma(p_i)$ as the unique intersection point satisfying

$$\gamma(p_i, \sigma(p_i)) = 1 . \quad (2.14)$$

Notice that

$$p_i \neq p_j \implies \sigma(p_i) \neq \sigma(p_j) , \quad (2.15)$$

and σ is therefore invertible. We construct the sequence (p_{α_i}) using

$$\begin{cases} p_{\alpha_1} = p_i , \\ p_{\alpha_{k+1}} = \sigma(p_{\alpha_k}) . \end{cases} \quad (2.16)$$

Notice that the sequence (p_{α_i}) satisfies the third condition of Eq. (2.11) for any length. The number of intersection point is finite, so there must be an integer K such that p_{α_K} is identical to p_{α_k} for $k < K$. We cut the sequence at the smallest possible K , so there is only one repeated element in the sequence. The repeated element must be p_{α_1} because σ is invertible. As a result, the sequence (p_{α_i}) is the unique path from p_i to p_i that does not contain only p_i and does not contain repeated points except for the endpoints. To prove the relationship, we notice that $p_i \sim p_j \implies$ the point p_j must be included in the unique sequence (p_{α_i}) . As a result, we can take a subsequence from p_i to p_j in (p_{α_i}) and $p_j \sim p_i$. \square

Theorem 2.3.3 (Transitivity of \sim)

$$\forall i, j, k : \begin{cases} p_i \sim p_j \\ p_j \sim p_k \end{cases} \implies p_i \sim p_k . \quad (2.17)$$

Proof The hypothesis gives us one path from p_i to p_j and one path from p_j to p_k . We can combine these two paths to go from p_i to p_k and $p_i \sim p_k$. \square

As a result, \sim is an equivalence relation for the set P of intersection points. We can define the classes of equivalency $\{P_i\} = P \setminus \sim$ corresponding to subsets of P containing all the elements that are equivalent under \sim (i.e., the quotient of P by \sim). We define the number of sets in $P \setminus \sim$ as n_P and we note that the equivalency classes constitute a partition of P . Namely the P_i are disjoint and the union of their elements is P . For the example intersecting curves, there are $n_P = 2$ equivalency classes, $P_1 = \{p_1, p_2\}$ and $P_2 = \{p_3, p_4, p_5, p_6\}$.

2.3.3 Lobe Area

We define

$$S(p) = \begin{cases} \int_{C_1^+[p, \sigma(p)]} y dx - x dy & \text{if } \rho(p) = +1 , \\ \int_{C_2^- [p, \sigma(p)]} y dx - x dy & \text{if } \rho(p) = -1 , \end{cases} \quad (2.18)$$

where $\sigma(p)$ has been defined in the proof of Theorem 2.3.2.

Conjecture:

$$[A_1 \setminus A_2] = \sum_{P_i \in P \setminus \sim} \left(\sum_{p \in P_i} S(p) \right) . \quad (2.19)$$

Notice that using $A_{C_1}^-$ and $A_{C_2}^+$ instead of $A_{C_1}^+$ and $A_{C_2}^-$ in the definition of γ (Eq. 2.10) gives another equivalence relationship. The equivalence classes of the latter gives the area $[A_2 \setminus A_1]$ in a form identical to Theorem 2.3.3. Also notice that Theorem 2.3.3 could be written with

a single sum over all the intersection points. However, we prefer to keep the sum of the equivalency classes. The sum over each intersection point in the same class correspond to the area of a lobe, i.e., an individual protuberance of A_1 outside A_2 .

2.3.4 Numerical Implementation

Intersection Points

The computation of the intersection points between two curves that are piecewise linear requires browsing every pair of linear segments (one on C_1 and one on C_2) and determining the possible intersection point between these two segments. This is a computationally expensive operation requiring one to solve a 2×2 linear system. Instead, we propose to quick check for the existence of an intersection point between two segments using the following properties.

Theorem 2.3.4 *If the segments $[(x_1, y_1), (x_2, y_2)]$ and $[(x'_1, y'_1), (x'_2, y'_2)]$ intersect, then we must have*

$$((y_2 - y_1)x'_1 - (x_2 - x_1)y'_1 - x_1y_2 + y_1x_2)((y_2 - y_1)x'_2 - (x_2 - x_1)y'_2 - x_1y_2 + y_1x_2) \leq 0 , \quad (2.20)$$

Proof The equation of the line passing through the two points (x_1, y_1) and (x_2, y_2) is

$$f(x, y) = (y_2 - y_1)x - (x_2 - x_1)y - x_1y_2 + y_1x_2 = 0 . \quad (2.21)$$

The theorem states that if the segment $[(x'_1, y'_1), (x'_2, y'_2)]$ intersects the segment $[(x_1, y_1), (x_2, y_2)]$, then it must also intersect the line $f(x, y) = 0$. As a result, the endpoints of the segment $[(x'_1, y'_1), (x'_2, y'_2)]$ must be on opposite sides of the line and we have

$$f(x'_1, y'_1)f(x'_2, y'_2) \leq 0 . \quad (2.22)$$

Theorem 2.3.4 gives us a necessary condition for an intersection between two segments. Notice that we can reverse the role of each segment in Theorem 2.3.4 and get another necessary condition. In addition, we have

Theorem 2.3.5 *The segments $[(x_1, y_1), (x_2, y_2)]$ and $[(x'_1, y'_1), (x'_2, y'_2)]$ intersect if and only if*

$$((y_2 - y_1)x'_1 - (x_2 - x_1)y'_1 - x_1y_2 + y_1x_2)((y_2 - y_1)x'_2 - (x_2 - x_1)y'_2 - x_1y_2 + y_1x_2) \leq 0 , \quad (2.23)$$

and

$$((y'_2 - y'_1)x_1 - (x'_2 - x'_1)y_1 - x'_1y'_2 + y'_1x'_2)((y'_2 - y'_1)x_2 - (x'_2 - x'_1)y_2 - x'_1y'_2 + y'_1x'_2) \leq 0 . \quad (2.24)$$

Proof Theorem 2.3.4 directly implies one direction (\implies) of the equivalence. To prove \impliedby , notice that if the two equations are satisfied, the endpoints of the first segment are on each side of the line containing the second segment. The endpoints of the second segment are also on each side of the line containing the first segment. As a result, the two segments must intersect in at least one point.

The two theorems above allow for a very fast and efficient algorithm to detect intersection points. Each segment on curve C_1 is checked for intersections with each segment on curve C_2 . However, only the necessary condition given by Theorem 2.3.4 is checked. Only if this condition is satisfied is the second condition in Theorem 2.3.5 checked. If the necessary and sufficient condition is satisfied, then the intersection point is effectively computed.

Integrals

We assume that the curves C_1 and C_2 are given in terms of a sequence of points (x_i, y_i) . We want an exact evaluation of the integral in Eq. (2.18) for piecewise polygonal curves. By

using Eq. (2.6) in the section above, Eq. (2.18) becomes

$$S(p) = \sum_{\substack{(x_i, y_i) \\ \in \mathcal{C}^{\rho(p)}[p, \sigma(p)]}} (y_i x_{i+1} - x_i y_{i+1}) . \quad (2.25)$$

2.4 Non-Transverse Intersections

2.4.1 Previous Approaches

Here, in contrast with the previous section, we do *not* require that the two curves have only transverse intersections. We allow non-transverse intersection points and we also allow segments of curves that are common to C_1 and C_2 .

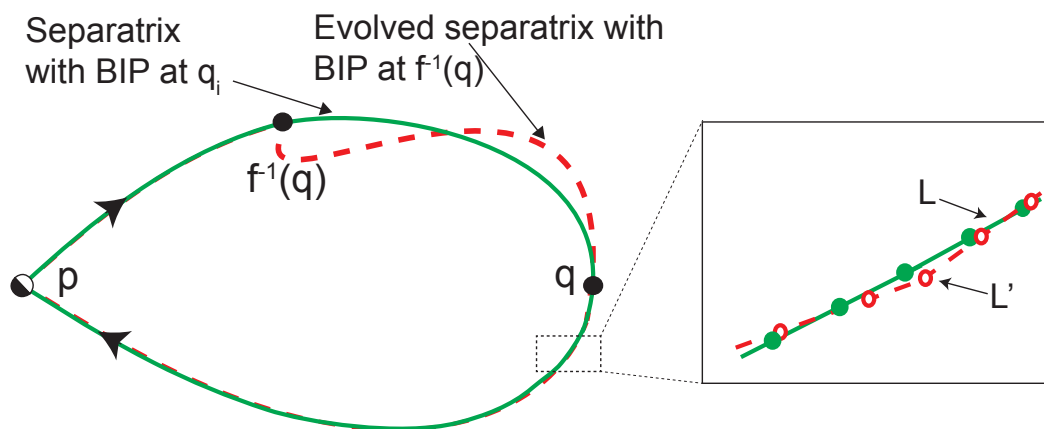


Figure 2.4: Schematic showing the slightly perturbed separatrices with different boundary intersection point (BIP). When the separatrices have near-tangent intersections, obtaining intersection points require inflating/deflating the points to avoid false lobes formed by the section of curve L and L' .

During previous numerical runs, we used an algorithm based on primary intersection points and regular intersection points to identify the boundary of each lobe and then compute the area of these lobes. These algorithms cannot be adapted to match the new problem. The tangency of the two curves creates both a confusion in the ordering of the intersection points

and the position of the lobes as well as an enormous computational difficulty to extract the actual position of the intersection (determinant of a linear system $\rightarrow 0$).

The most reasonable patch used is to “inflate” or “deflate” the curves before computation in order to avoid the tangency. We transformed each point \bar{x} of one of the curves to $\bar{x} + \epsilon(\bar{x} - \bar{x}_g) / \|(\bar{x} - \bar{x}_g)\|$, where \bar{x}_g is the center of gravity of the curve. This can remove the presence of non-transverse intersections for $\epsilon > \epsilon_0$, where the limit ϵ_0 is carefully chosen. However, the curve used in our problem contains many segments very close to each other in such a way that increasing ϵ above the minimum distance between the segments ϵ_1 creates new non-transverse intersections. In one example, ϵ_1 was smaller than ϵ_0 forbidding the use of this trick to compute the lobe area. Moreover, the error on the area increases quickly with ϵ , so we developed the following exact method that is robust to the presence of non-transverse intersection of the curves.

2.4.2 Interior Function

Let us define the complex function

$$f_{z_0}(z) = \frac{1}{x - x_0 + i(y - y_0)}. \quad (2.26)$$

The integral of $f(z)$ over a closed curve is equal to $2i\pi$ times the number of turns that the closed curve makes around the point $x_0 + iy_0$ (to prove that, use the fact that $f(z)$ is analytic everywhere in the complex plane except at $x_0 + iy_0$ and use the residue theorem).

We define

$$J_i(x_0, y_0) = \text{Im} \left\{ \int_{C_i} \frac{dx + idy}{x - x_0 + i(y - y_0)} \right\}, \quad (2.27)$$

and

$$I_i(x_0, y_0) = \begin{cases} 1 & \text{if } J_i(x_0, y_0) < \pi \\ -1 & \text{if } J_i(x_0, y_0) \geq \pi \end{cases}, \quad (2.28)$$

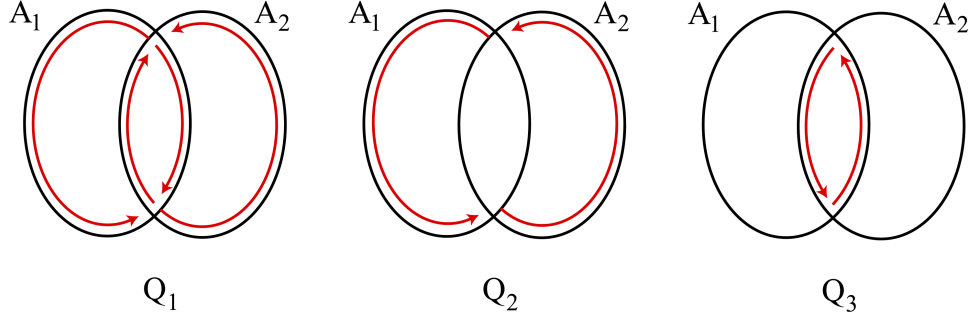


Figure 2.5: Schematic view of the paths involved in the definition of Q_1 , Q_2 and Q_3 .

and we notice that $I_i(x_0, y_0)$ is negative when the point (x_0, y_0) is contained in A_i and positive otherwise.

2.4.3 Lobe Area

In order to extract $[A_1 \setminus A_2]$ and $[A_2 \setminus A_1]$ from the shape of the curves, we define the following quantities

$$Q_1 = \int_{C_1} I_2(x, y) (ydx - xdy) + \int_{C_2} I_1(x, y) (ydx - xdy), \quad (2.29)$$

$$Q_2 = \int_{C_1} \frac{I_2(x, y) + 1}{2} (ydx - xdy) + \int_{C_2} \frac{I_1(x, y) + 1}{2} (ydx - xdy), \quad (2.30)$$

$$Q_3 = \int_{C_1} \frac{I_2(x, y) - 1}{-2} (ydx - xdy) + \int_{C_2} \frac{I_1(x, y) - 1}{-2} (ydx - xdy). \quad (2.31)$$

A quick look at the different paths on Fig. 2.5 reveals that

$$Q_1 = [A_1 \cup A_2] - [A_1 \cap A_2] = [A_1 \setminus A_2] + [A_2 \setminus A_1] \quad (2.32)$$

$$Q_2 = [A_1 \cup A_2], \quad (2.33)$$

$$Q_3 = [A_1 \cap A_2]. \quad (2.34)$$

Notice that the three equation above are not linearly independent and *any* of them can give us the expected results. However, we compute Q_1 , Q_2 and Q_3 and use the redundancy to minimize the error on the integrals and provide an approximation of the computational error. Since

$$[A_1 \setminus A_2] = [A_1 \cup A_2] - [A_2] = [A_1] - [A_1 \cap A_2], \quad (2.35)$$

and

$$[A_2 \setminus A_1] = [A_1 \cup A_2] - [A_1] = [A_2] - [A_1 \cap A_2], \quad (2.36)$$

we have

$$[A_1 \setminus A_2] = \frac{1}{2}(Q_2 - Q_3) + \frac{1}{2}([A_1] - [A_2]), \quad (2.37)$$

and

$$[A_2 \setminus A_1] = \frac{1}{2}(Q_2 - Q_3) + \frac{1}{2}([A_2] - [A_1]). \quad (2.38)$$

And using

$$[A_1] + [A_2] = [A_1 \cup A_2] + [A_1 \cap A_2], \quad (2.39)$$

we find

$$[A_1 \setminus A_2] = \frac{1}{2}Q_1 + \frac{1}{2}([A_1] - [A_2]), \quad (2.40)$$

and

$$[A_2 \setminus A_1] = \frac{1}{2}Q_2 + \frac{1}{2}([A_2] - [A_1]). \quad (2.41)$$

Our algorithm combines these two results and provides the following final answer

$$[A_1 \setminus A_2] = \frac{1}{2}(A_1 - A_2) + \frac{1}{4}(Q_1 + Q_2 - Q_3), \quad (2.42)$$

$$[A_2 \setminus A_1] = \frac{1}{2}(A_2 - A_1) + \frac{1}{4}(Q_1 + Q_2 - Q_3), \quad (2.43)$$

$$\delta[A_1 \setminus A_2] = \delta[A_2 \setminus A_1] = \frac{1}{4} |Q_2 - Q_3 - Q_1| , \quad (2.44)$$

where the last equation gives the approximate error on the computed area.

2.4.4 Numerical Methods

The only technical difficulty in this algorithm is the numerical computation of the functions J_i in Eq. (2.27). A fast and accurate algorithm for polygonal boundaries is given in §2.4.4. The computation of the integrals in Eq. (2.29), (2.30) and (2.31) is similar to the integral computed in §2.2.2.

In addition, we present a simple algorithm that we used to densify the curve close to the intersection points. The algorithm in §2.4.4 has proved to increase the accuracy of this method without decreasing its efficiency too much.

Computation of $J_i(x, y)$

In this section, we derive the exact value of the function J_i defined in Eq. (2.27) when the boundary C_i is a polygonal line. For each linear segment $[(x_1, y_1), (x_2, y_2)]$, we have

$$\begin{cases} x = x_1 + t(x_2 - x_1) , \\ y = y_1 + t(y_2 - y_1) . \end{cases} \quad (2.45)$$

Hence,

$$Im \left\{ \frac{dx + idy}{x - x_0 + i(y - y_0)} \right\} = \frac{(x_1 - x_0)(y_2 - y_1) - (y_1 - y_0)(x_2 - x_1)}{(x_1 - x_0 + t(x_2 - x_1))^2 + (y_1 - y_0 + t(y_2 - y_1))^2} , \quad (2.46)$$

$$= \bar{1}_z \frac{(\bar{x}_1 - \bar{x}_0) \times (\bar{x}_2 - \bar{x}_1)}{\|\bar{x}_2 - \bar{x}_1\|^2 t^2 + 2(\bar{x}_2 - \bar{x}_1) \cdot (\bar{x}_1 - \bar{x}_0)t + \|\bar{x}_1 - \bar{x}_0\|^2} , \quad (2.47)$$

$$= \frac{\|u\|^2 \|v\|^2 \sin(u, v)}{\|v\|^2 t^2 + 2 \|\bar{u}\| \|\bar{v}\| \cos(\bar{u}, \bar{v}) t + \|u\|^2} , \quad (2.48)$$

where

$$\begin{cases} \bar{u} &= \bar{x}_1 - \bar{x}_0, \\ \bar{v} &= \bar{x}_2 - \bar{x}_1. \end{cases} \quad (2.49)$$

Notice that the realisant of the denominator of Eq. 2.48 is

$$\rho = -4 \|\bar{u}\|^2 \|\bar{v}\|^2 \sin^2(\bar{u}, \bar{v}) \leq 0. \quad (2.50)$$

As a result, we have

$$Im \left\{ \int_{[\bar{x}_1, \bar{x}_2]} \frac{dx + idy}{x - x_0 + i(y - y_0)} \right\} = \int_0^1 \frac{\|\bar{u}\|^2 \|\bar{v}\|^2 \sin(u, v) dt}{\|\bar{v}\|^2 t^2 + \|u\| \|v\| \cos(\bar{u}, \bar{v}) + \|\bar{u}\|^2} \quad (2.51)$$

$$= \frac{\sin(\bar{u}, \bar{v})}{|\sin(\bar{u}, \bar{v})|} \left[\tan^{-1} \frac{\|v\|^2 t + \bar{u} \cdot \bar{v}}{\|\bar{u}\| \|\bar{v}\| |\sin(\bar{u}, \bar{v})|} \right]_0^1 \quad (2.52)$$

$$= \tan^{-1} \frac{\|\bar{v}\|^2 + \bar{u} \cdot \bar{v}}{\bar{1}_z \cdot (\bar{u} \times \bar{v})} - \tan^{-1} \frac{\bar{u} \cdot \bar{v}}{\bar{1}_z \cdot (\bar{u} \times \bar{v})} \quad (2.53)$$

Notice that for $\sin(\bar{u}, \bar{v}) = 0$, the increment to the integral is zero. This is consistent with the equation above where the right-hand term is continuous for $\bar{u} \times \bar{v} = 0$ and vanishes.

From a numerical point of view, ...

get back to original notation

One can easily check that

$$\phi'(0) = \frac{\|\bar{v}\|}{\|u\| + \|v\|}. \quad (2.54)$$

Hence when $\sin(u, v)$ is small, one can approximate the integral by

$$\phi = \frac{\|v\|}{\|u\| + \|v\|} \sin(\bar{u}, \bar{v}), \quad (2.55)$$

or

$$\phi = \bar{1}_z \frac{\bar{u} \times \bar{v}}{\|\bar{u}\| (\|\bar{u}\| + \|\bar{v}\|)}. \quad (2.56)$$

This approach is exactly as point in polygon problem in computational geometry which favors the ray passing over the winding number concept. Although, our method is mathematically satisfying, it can have poor performance when compared to the more efficient method of ray passing. This is due to the integral and trigonometric function evaluations that are involved but our purpose is to adopt a more rigorous method with some sacrifice of performance.

Curve Densifier

There is a built-in densifier in the light version of Lober. It adds points on the curves close to their intersections. To activate the densifier, add the parameters `-DENS <nPass> <nDens>` at the end of the command line. The arguments `<nPass>` and `<nDens>` give respectively the number of passes to be performed and the number of points to add near each intersection at each pass.

The extra precision is always $i_r = n_{dens}^{n_{pass}}$. In other words, the precision is the same with $(n_{pass} = 1, n_{dens} = 1000)$ than with $(n_{pass} = 3, n_{dens} = 10)$. For a constant i_r , the value of the two parameters n_{dens} and n_{pass} should minimize the computational time. Small n_{pass} means that fewer steps are necessary to densify the curve and can reduce the computational time. However, small n_{pass} usually implies large n_{dens} to maintain a constant i_r . Since the extra length of the curve is $n_{dens}n_{pass}$, the number of points increases rapidly if n_{pass} is too small and lengthens the computation. So there is an optimal n_{pass} that minimizes computation time.

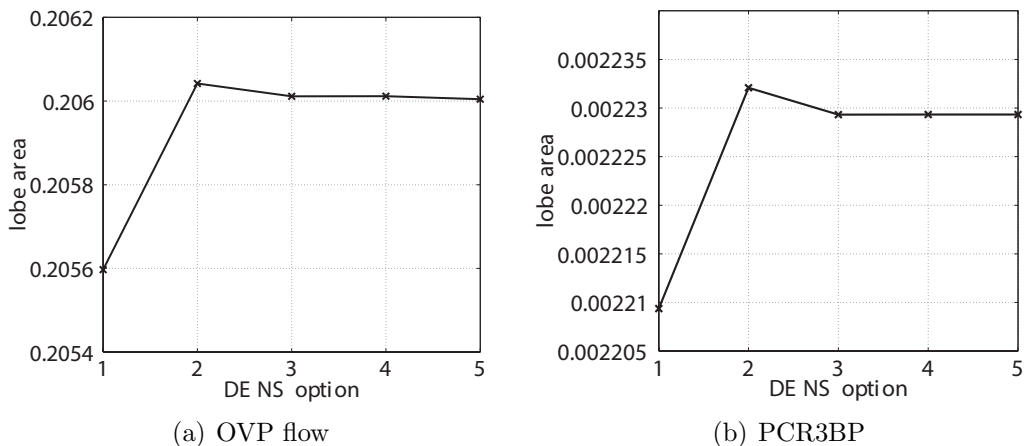


Figure 2.6: Showing the lobe area for different curve densifier option in OVP flow and PCR3BP. Along the x-axis the indices denote the following densifier options:1.-DENS 0, 2.-DENS 1 10, 3.-DENS 3 10, 4. -DENS 5 100, 5. without -DENS option which triggers the AUTO densifier. The y-axis is the average of the entraining and detraining lobes for the parameters $\epsilon = 0.1, \gamma = 0.5$ related to the flow. Using webplotDigitizer, we obtained lobe area from the analytical result in [18] which is $\mu(L) \approx 2\epsilon|F(\gamma)| \approx 0.2145$.

2.5 Application to Dynamical Systems and Lobe Dynamics

In this section, we will explore transport in phase space using the theory of intersection points and curves developed in the previous section. This will also be an exercise in using geometric approach of lobe dynamics and heteroclinic/homoclinic tangles.

2.5.1 Chaotic transport in fluid flow

We will apply the methods developed above to quantify phase space transport in the oscillating vortex pair (OVP) flow that was introduced in Rom-Kedar et al. [18]. In this fluid flow, it is of interest to calculate the escape rates of species S_1 from the inner core R_1 to the outside region R_2 shown in Fig. 2.7(b). For two-dimensional, incompressible, inviscid fluid flow, it is known that the stream-function is analogous to the Hamiltonian governing parti-

cle motion and the domain of the fluid flow is identified as the phase space. The OVP flow is generated by two-counter rotating vortices which are sinusoidally perturbed to obtain a non-autonomous velocity field in \mathbb{R}^2 . Under the steady flow, without external perturbation, the trajectory on the streamfunction, $\Psi = 0$ approaches the saddle equilibrium points p_+ as $t \rightarrow \infty$ and p_- as $t \rightarrow -\infty$ ($p_+ \neq p_-$ for heteroclinic and $p_+ = p_-$ for homoclinic connections). This acts as a boundary restricting particles to enter or escape the region R_1 and in dynamical systems terminology, is called *separatrix*. However, with suitable perturbation the picture changes dramatically as transport across the boundary becomes feasible due to chaotic particle motion in phase space. We introduce a periodic perturbation in the flow field and generate the Poincaré map defined by

$$f : U^0 \rightarrow U^0 \tag{2.57}$$

$$\text{where, } U^0 = \{(x, y, \theta) \in \mathbb{R}^2 \times \mathbb{S}^1 : \theta = 0\} \tag{2.58}$$

is the cross-section on which the structure of manifolds and associated lobe dynamics is applied. The general transport problem for two-dimensional maps and underlying geometric view of quantifying transport is developed and presented in detail in [6, 33, 18] and we will briefly summarize the approach relevant for the numerical experiments in our study.

The dynamical system of interest is the passive particle motion in a co-moving frame of two counter rotating vortices under an external field of sinusoidal strain-rate. Casting the equations in a Hamiltonian formulation using the streamfunction as the Hamiltonian function and performing perturbation expansion of the velocity field (refer [18] for details), the system can be expressed as

$$\begin{aligned} \dot{x}t &= f_1(x, y) + \epsilon g_1(x, y, t/\gamma; \gamma) + \mathcal{O}(\epsilon^2) \\ \dot{y}t &= f_2(x, y) - \epsilon g_2(x, y, t/\gamma; \gamma) + \mathcal{O}(\epsilon^2) \end{aligned} \tag{2.59}$$

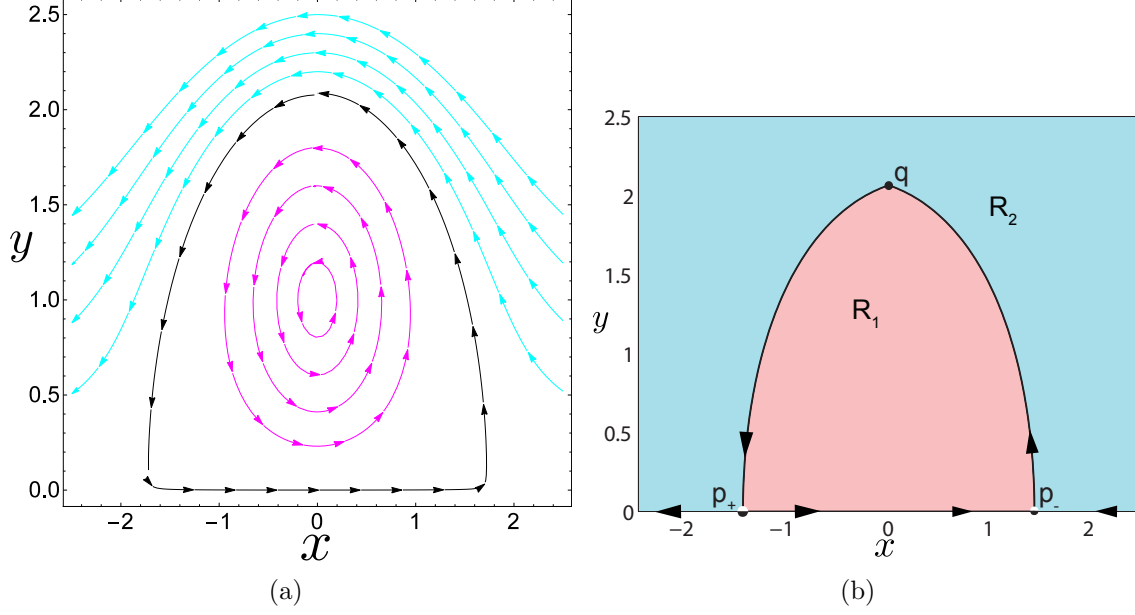


Figure 2.7: (a) shows the unperturbed streamlines with periodic orbits in the region R_1 and free flow region R_2 and (b) shows the regions of interest R_1 and R_2 for studying transport in the OVP flow. The transport between the regions R_1 and R_2 can be explained and quantified in terms of the turnstile mechanism.

where,

$$f_1 = -\frac{y-1}{I_-} + \frac{y+1}{I_+} - 0.5 \quad (2.60)$$

$$f_2 = \frac{x}{I_-} - \frac{x}{I_+}$$

and

$$g_1 = [\cos(t/\gamma) - 1] \left\{ \frac{1}{I_-} + \frac{1}{I_+} - \frac{2(y-1)^2}{I_-^2} - \frac{2(y+1)^2}{I_+^2} \right\}$$

$$+ (x/\gamma) \sin(t/\gamma) \left\{ \gamma^2 \left[\frac{y-1}{I_-^2} - \frac{y+1}{I_+^2} \right] + 1 \right\} - 0.5$$

$$g_2 = 2x[\cos(t/\gamma) - 1] \left\{ \frac{y-1}{I_-^2} + \frac{y+1}{I_+^2} \right\} \quad (2.61)$$

$$+ (1/\gamma) \sin(t/\gamma) \left\{ \frac{\gamma^2}{2} \left[\frac{1}{I_-} - \frac{1}{I_+} \right] - x^2 \gamma^2 \left[\frac{1}{I_-^2} - \frac{1}{I_+^2} \right] - y \right\}$$

$$\text{and} \quad I_{\pm} = x^2 + (y \pm 1)^2$$

The OVP flow has two non-dimensional parameters which denote the circulation strength of the vortices, γ , and perturbation amplitude, ϵ . For a complete analysis of transport in such

a flow, Rom-Kedar et al. [18] explores a combination of these two parameters but we will present two cases as application of theory presented and implemented in Lober. Due to the complicated nature of the vector field in Eqn. (2.59), we numerically compute the invariant manifolds using *globalization* (see [34]) technique and based on the benchmark algorithm in [35]. The two cases of manifold computation presented in Fig. 2.8 show differences in geometry of *turnstile*s when the manifolds have near-transverse or near-tangent intersections. Using the computed manifolds as inputs to Lober, we can identify the lobes, separatrix, pips and manifolds as shown in Fig. 2.5.1.

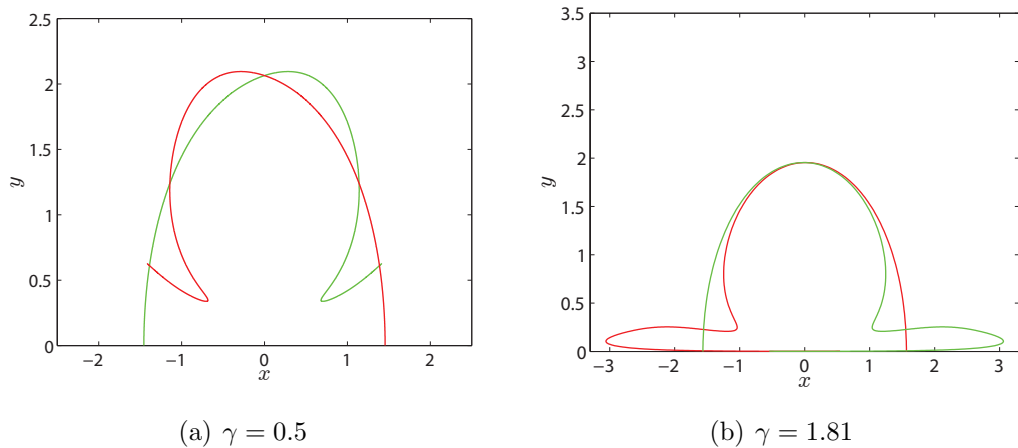


Figure 2.8: Computed unstable (red) and stable (green) manifolds of the hyperbolic fixed points for perturbation amplitude of $\epsilon = 0.1$. The manifolds are shown for qualitative comparison and a change in orientation for the γ values as predicted by Melnikov theory in Ref. [18].

In essence, the perturbation destroys the separatrix as a boundary defined as,

$$B(q) = \{W^s[p_{+, \epsilon}, q] \cup W^u[p_{-, \epsilon}, q]\} \cup \{W_{-, \epsilon}^s \cap W_{+, \epsilon}^u\} \quad (2.62)$$

and pieces of the stable and unstable manifolds of the hyperbolic fixed points $(p_{+, \epsilon}, p_{-, \epsilon})$ intersect to form lobes, which is the skeleton for transport across the boundary. Using a pip on these manifolds, we choose one to use as a *boundary intersection point* (bip) q which parametrizes a pair of entering and exiting lobes; called *turnstile*s by MacKay et al. [36].

The collection of turnstile lobes is defined in terms of the bip and its pre-image as [6]:

$$L_{1,2}(1) \cup L_{2,1}(1) = W^s[f^{-1}(q), q] \cup W^u[f^{-1}(q), q] \quad (2.63)$$

where, $L_{i,j}(n)$ denotes lobe in the region R_i that is mapped to the region R_j after n iterates.

Using the turnstiles, we can express the volume of species S_i that is transported in terms of intersection areas of the lobes and iterates of the Poincaré map. Following the theory described in [6], we use the following quantities of interest:

1. $a_{i,j}(n)$: Flux of species S_i from region R_i into region R_j on the n^{th} iterate.
2. $T_{i,j}(n)$: Total amount of species S_i contained in region R_j after the n^{th} iterate.

We have the following approaches (see Appendix. A.1 for usage details) for computing these quantities:

1. *Separatrix method*: Generate separatrices with q and its pre-images ($f^{-1}(q), f^{-2}(q), \dots$) as BIP. This can be performed by evolving the separatrix or executing *Lober* with different BIP index. This is shown in Fig. 2.9 and these curves are now used as input to the *light* option of *Lober*.
2. *Lobe method*: Obtain the turnstile lobes $L_{1,2}(1), L_{2,1}(1)$ and images of entering (in the sense of entering the region R_1 in the next iterate) lobe $L_{2,1}(1)$ or pre-images of exiting lobe $L_{1,2}(1)$. These are obtained from *Lober* as closed curves and given as input to the *light* option of *Lober* to compute intersection areas.

Using the Lemma 2.3 and Theorem 2.5 in [6], the quantity $a_{2,1}$ in terms of the turnstiles and intersection areas is expressed as,

$$a_{2,1}(n) = T_{2,1}(n) - T_{2,1}(n-1) = \mu(L_{2,1}(1)) - \sum_{m=1}^n \mu(L_{2,1}(1) \cap f^{m-1}(L_{1,2}(1))) \quad (2.64)$$

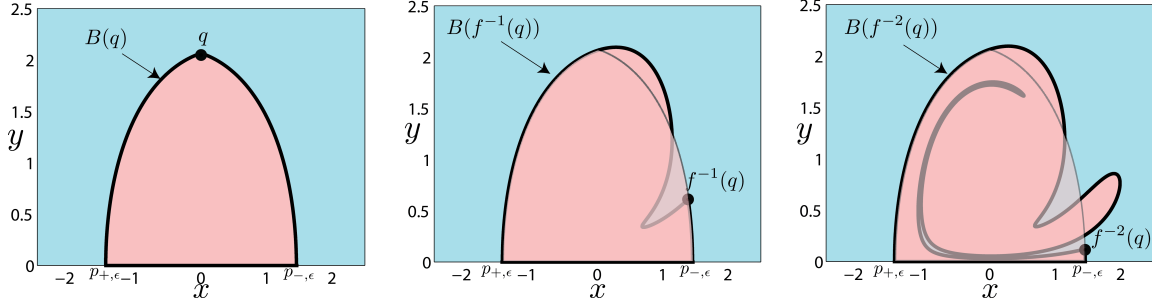


Figure 2.9: Showing the separatrix with q as a bip and its backward evolution with the pre-images of q as bips. The region R_1 is the transparent layer on the pre-images.

The quantity under the summation is the intersection area of the lobe $L_{2,1}(1)$ and pre-images of $L_{1,2}(1)$ that is shown in the Fig. 2.10 and demonstrates the difficulty in tracking lobe boundaries as stretching and folding generates thin filaments of curves with near-tangent intersections. While, the lobe method is a reduced order calculation for transport, separatrix

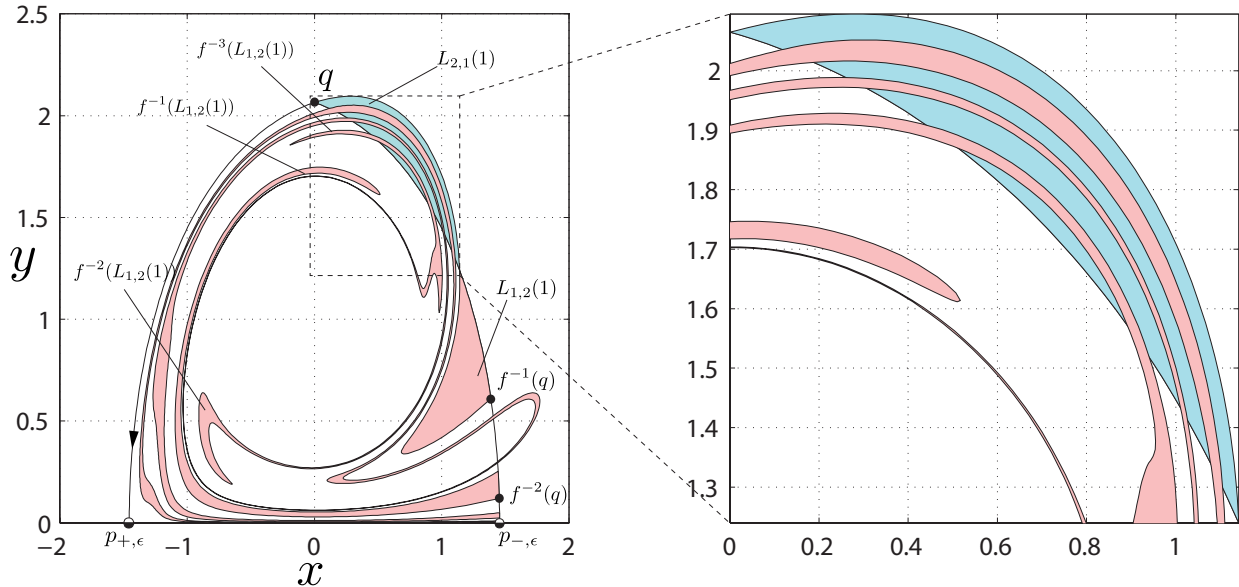


Figure 2.10: Showing the *turnstiles* in red(entraining lobe labeled $L_{1,2}(1)$) and cyan(detraining lobe labeled $L_{2,1}(1)$) for the OVP flow with parameters $\epsilon = 0.1, \gamma = 0.5$. The zoom-in view shows the intersection regions that are used in quantifying the transport.

method is useful when multilobe and self-intersecting turnstiles generate tangent intersections and tracking boundaries and even test points becomes expensive. In terms of the

boundary, the quantity $T_{1,2}(n)$ is given by

$$T_{1,2}(n) = [B(q) \setminus (B(q) \cap f^{-n}(B(q)))] \quad (2.65)$$

and the quantity $a_{1,2}(n)$ is

$$a_{1,2}(n) = T_{1,2}(n) - T_{1,2}(n - 1) \quad (2.66)$$

For validating `Lober` results, invariant manifolds of the hyperbolic fixed points $p_{+,\epsilon}, p_{-,\epsilon}$ are provided as input and the outputs are shown in Fig. 2.5.1. It clearly identifies the lobes, pips and separatrix parametrized by the pip at $q = (0.0, 2.065)$, and indexed as $\lfloor \#\text{pips}/2 \rfloor$.

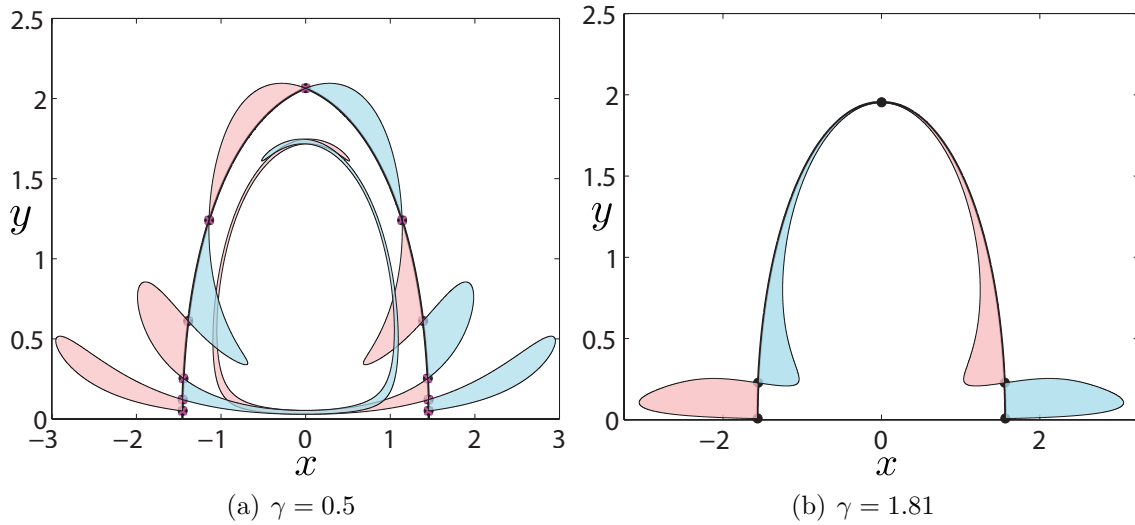


Figure 2.11: Output of `Lober` identifying the lobes, pips(filled black circle) and the separatrix(thick black line). For both the cases, $\epsilon = 0.5$.

Using the separatrix method, we obtain the lobe areas for different γ values and shown in Fig. 2.12(a). We will explore the advantages of the separatrix method for the next application where computing intersection of lobe areas can be more complicated. This can be used as an alternate method to express the transport quantities in lobe dynamics. However, for validation purpose we have performed the intersection of lobe area computations to obtain

a_{ij} in Eqn. (2.64) and show the results for first 7 iterations of the map f in Fig. (2.12(b)).

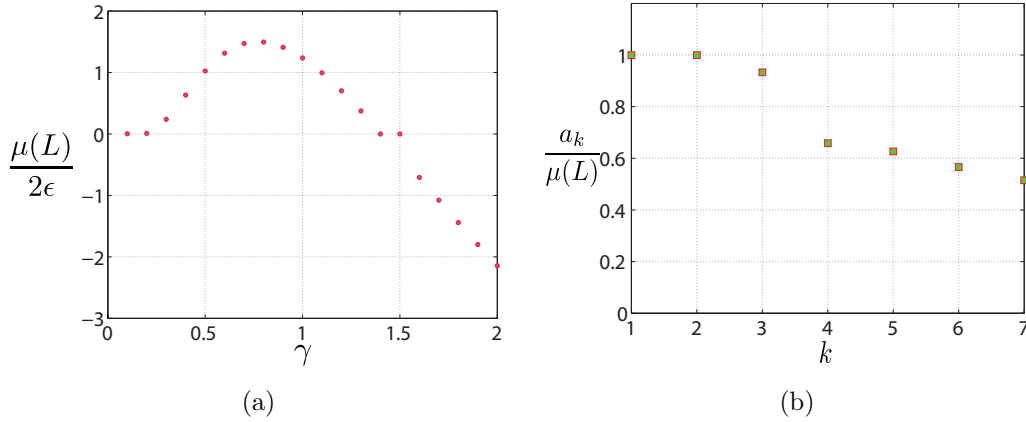


Figure 2.12: Fig. (a) Shows the area of lobes for $\epsilon = 0.1$ and different γ values. This agrees well with Fig.9 in [18] which compares the brute force method of lobe area calculations with Melnikov function. Fig. (b) Shows the normalized fluid volume for increasing iterates of the perturbation period.

2.5.2 Escape from a potential well

In this application of Lober, we will apply the geometric methods of phase space transport to a ship capsizing model to calculate escape rate from a potential well and combines transition state theory (ref chemical physics and atomic physics papers) and tube dynamics ((ref celestial mechanics papers)) to characterize non-capsizing criteria. We will consider a prototypical system in the form of a rescaled Lagrangian given by

$$\mathcal{L}(x, y, v_x, v_y) = \frac{1}{2}v_x^2 + \frac{1}{R^2}v_y^2 - V(x, y) \quad (2.67)$$

$$\text{and where,} \quad V(x, y) = \frac{1}{2}x^2 + y^2 - x^2y \quad (2.68)$$

is the corresponding potential function that arises in a coupled pitch and roll model of ship dynamics and the parameter $R = \omega_\theta/\omega_\phi$ is the ratio of natural pitch and roll frequencies (refer [37] and Ross2012 for the details). The ship's motion in absence of non-conservative,

time-varying sea waves is thus given by the first-order ODEs as

$$\left. \begin{aligned} \dot{x} &= v_x \\ \dot{y} &= v_y \\ \dot{v}_x &= -x + 2xy \\ \dot{v}_y &= -R^2y + \frac{1}{2}R^2x^2 \end{aligned} \right\} \quad (2.69)$$

which conserves the energy

$$E(x, y, v_x, v_y) = \frac{1}{2}v_x^2 + \frac{1}{R^2}v_y^2 + \frac{1}{2}x^2 + y^2 - x^2y \quad (2.70)$$

The projection of energy manifold

$$\mathcal{M}(e) = \{(x, y, v_x, v_y) | E(x, y, v_x, v_y) = e\}$$

onto configuration space is historically known as *Hill's region* and bounds the region that is energetically accessible as shown in Fig. 2.13. The nonlinear system of equations (Eqn. 2.69) have saddle equilibrium points at $(\pm 1, 0.5, 0, 0)$ and the realms of possible motion in configuration space between the saddles is called the *non-capsize realm* and all possible states beyond as *capsize realm*. The intersection of Hill's region and the non-capsize realm is the potential well from which escape identifies capsizes and escape rate is the percentage of trajectories that capsizes. When the energy is above its critical value, necks appear around the saddle points (Fig. 2.13(b)) that acts as a "threshold" for states in non-capsize region to escape. Traditionally, escape rate of trajectories from the non-capsize realm is computed using *tube dynamics* [21] and *transition state theory* [38] along with Monte-Carlo method to estimate area inside bounded curves ([39]).

However, we will use the implementation in *Lober* to compute the escape rate from area of closed curves and briefly summarize the steps involved in computing the curves of interest

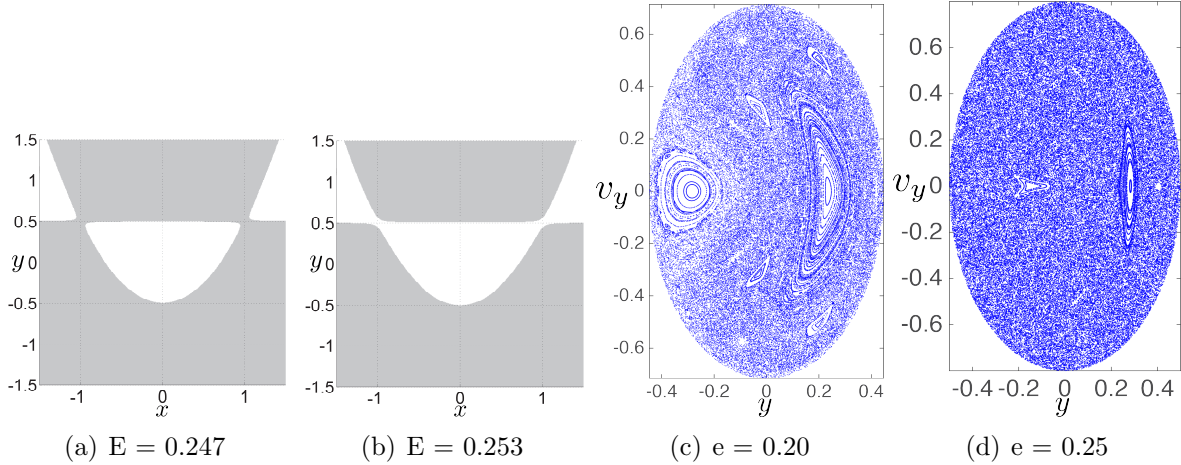


Figure 2.13: Realms of possible motion shown in white and energetically inaccessible region in grey for capsizes/critical energy, $E_c = 0.25$ and $R = 1.6$. Poincaré S-O-S defined by U_1 of the energy manifold.

(refer [34] for more details). *Firstly*, we select a suitable Poincaré Surface-Of-Section (S-O-S) which would be able to illustrate the transition dynamics and escape of trajectories. It is discussed in [40] as selecting a periodic orbit surface of section that can avoid pathological situations of intersection of manifolds and Poincaré S-O-S. However, we make an educated guess for the present system and define the S-O-S as

$$U_1 = \{(y, v_y) | x = 0, v_x(y, v_y; e) > 0\} \quad (2.71)$$

which defines a plane to capture motion of trajectories to the right saddle shown in Fig. 2.14. The $(y - v_y)$ surface-of-section captures the chaotic behavior that ensues when the energy is greater than the energy of the saddle or critical value and the KAM curves that begin to disappear as shown in Fig. 2.13. *Secondly*, we obtain the periodic orbit about the hyperbolic fixed point which for the symmetric configuration space is independent of the escape direction. The periodic orbit (p.o.) corresponding to a energy level $e + \Delta e$ is the bounding p.o. that touches the Hill's region boundary for that energy. *Thirdly*, we compute the invariant manifolds of the p.o. using globalization technique and obtain intersection of the tubes (manifolds are codimension-1 object and in 4D phase space represent 3D surfaces) with the

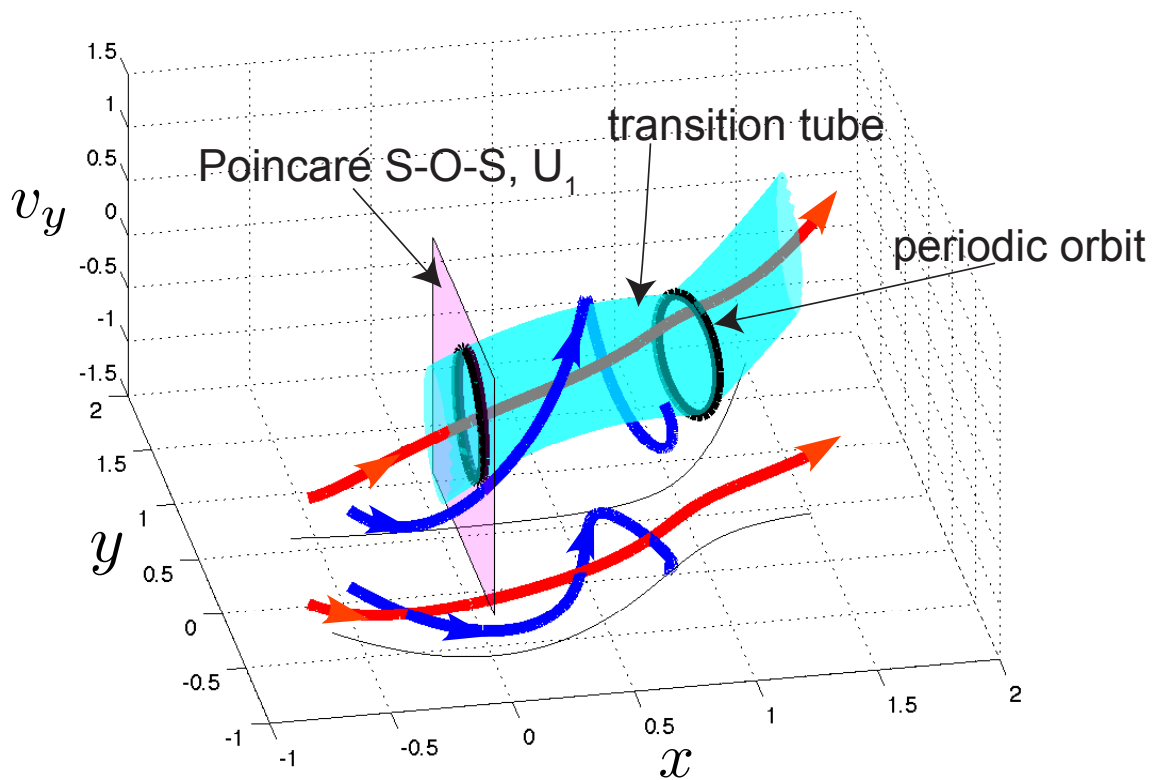


Figure 2.14: Showing the periodic orbit and corresponding stable manifold as transition tube for trajectory (red) escaping to the capsized realm and non-transit trajectory (blue) that remains bounded.

Poincaré surface-of-section given by Eqn. (4.2.13). Thus intersections are closed curves topologically equivalent to a S^1 and form *tiling*[[40]] for the surface-of-section. *Notation for tube intersection with the SOS:* To describe the intersection of the tube manifolds and S-O-S, U_1 we denote the manifolds by $W_{(\cdot)}^{(\cdot)}$ where the superscript is either s/u for the stable/unstable tube branch inside the well and the subscript is either C_L/C_R for the left/right critical point. The intersection of $W_{(\cdot)}^{(\cdot)}$ and U_1 is further denoted by $W_{(\cdot)}^{(\cdot)} \cap U_1$.

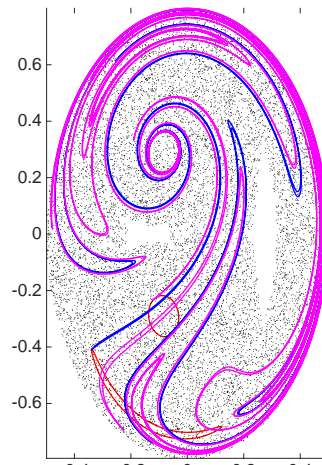
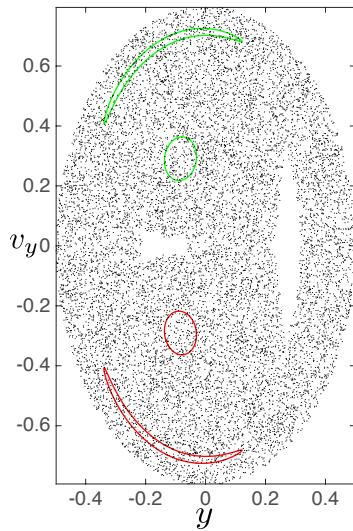
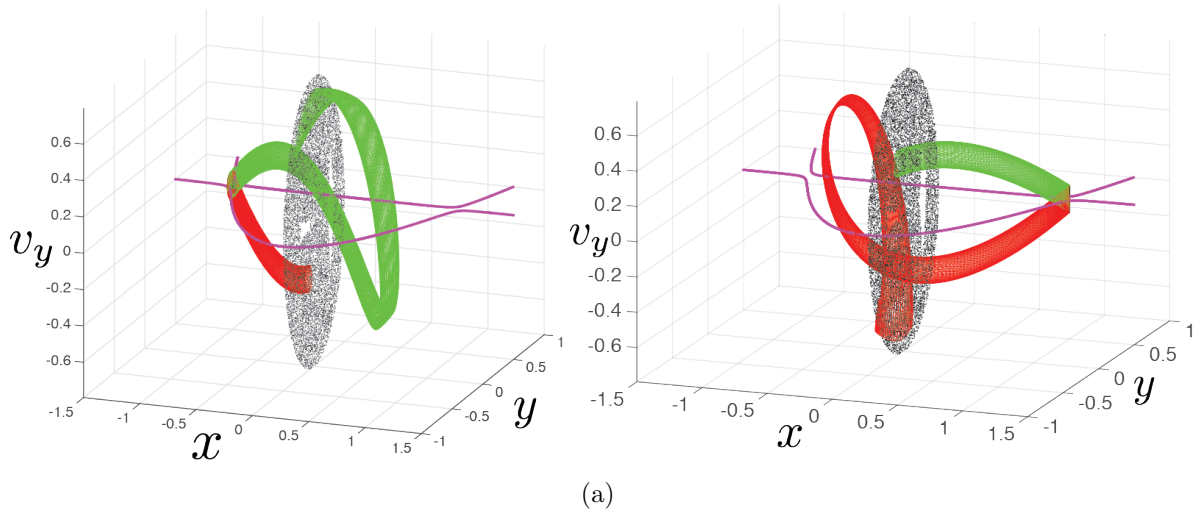


Figure 2.15: Tube manifolds of right and left critical points in (x, y, v_y) subspace of the 4D phase space for energy, $\Delta e = 0.00307$ above critical energy.

2.6 Conclusion

Lobe dynamics describes global transport in terms of lobes, parcels of phase space bounded by stable and unstable invariant manifolds associated to hyperbolic fixed points of the system. Escape from a potential well involves describes the study of phase space structures that lead to critical events by crossing of certain barriers. Both of these frameworks—in the circumstances where the dynamics are reduced to two-dimensional maps—require compu-

Exit via left after intersection #	Entrance via left	Entrance via right
1	0%	0%
2	0%	11.5%
3	2.93%	0.016%
4	1.87%	1.441%
Exit via right after intersection #	Entrance via left	Entrance via right
1	0%	0%
2	0%	0%
3	11.2%	2.90%
4	0.0246%	0.278%

Table 2.5: Percentage of trajectories escaping via left/right stable tube that entered via left and right unstable tubes.

tation of curves, intersection points, and area bounded by the curves to quantifying phase space transport.

In the paper, we presented a theory for classification of intersection points to compute the area bounded between the segments of the curves. This involves the partition of the intersection points into equivalence classes to apply a discrete form of Green’s theorem. An alternate method for curves with non-transverse intersections—related to identifying lobes by iterating the separatrix using the flow map—was also presented along with a method to insert points in the curve for densification. A software package *Curve_densifier* implements a interpolation and insertion method in MATLAB for increasing the number of points on a curve and is made available as open-source repository in Github (https://github.com/Shibabrat/curve_densifier). In this case, the notion of primary intersection point and secondary intersection point is not suitable and hence, we propose a generalization of the notion of lobes for two intersecting curves. We presented a numerical implementation of the approaches for computation of intersection points between two closed curves, lobes defined by these intersections, and the area of these lobes. The software package *Lober* based on the theory and numerical methods is made available as open-source repository in Github (<https://github.com/shibabrat/lober>). The framework described was applied to transport problems in fluid transport and escape from a potential well in

context of ship motion and capsizing.

2.7 Acknowledgements

This work was supported by the National Science Foundation under award 1150456 and 1537349.

References

- [3] S. Wiggins, *Chaotic Transport in Dynamical Systems* vol. 2 Interdisciplinary Appl. Math. Berlin-Heidelberg-New York: Springer, 1992
- [6] Stephen Wiggins, *Chaotic transport in dynamical systems*
- [8] Vered Rom-Kedar, *Part I: An Analytical Study of Transport, Mixing, and Chaos in an Unsteady Vortical Flow. Part II: Transport in Two Dimensional Maps*. PhD thesis California Institute of Technology, 1988
- [18] Vered Rom-Kedar, A. Leonard, and S. Wiggins, An analytical study of transport, mixing and chaos in an unsteady vortical flow, *J. Fluid Mech.*, 214 (1990), 347–394
- [19] D. Beigie, Multiple separatrix crossing in multi-degree-of-freedom Hamiltonian flows, English *Journal of Nonlinear Science*, 5.1 (1995), 57–103
- [20] Francois Lekien, Shawn C. Shadden, and Jerrold E. Marsden, Lagrangian coherent structures in n-dimensional systems, *Journal of Mathematical Physics*, 48.6, 065404 (2007), 1–19
- [21] M. Dellnitz, O. Junge, W. S. Koon, F. Lekien, M. W. Lo, J. E. Marsden, K. Padberg, R. Preis, S. D. Ross, and B. Thiere, Transport in dynamical astronomy and multibody problems, *Int. J. Bifurc. Chaos*, 15 (2005), 699–727

- [22] J Duan and S Wiggins, Lagrangian transport and chaos in the near wake of the flow around an obstacle: a numerical implementation of lobe dynamics, *Nonlinear Processes in Geophysics*, 4.3 (1999), 125–136
- [23] Roger M Samelson and Stephen Wiggins, *Lagrangian transport in geophysical jets and waves: the dynamical systems approach* vol. 31 Springer, 2006
- [24] Vered Rom-Kedar and S. Wiggins, Transport in two-dimensional maps, *Arch. Rat. Mech. Anal.*, 109 (1990), 239–298
- [25] Vered Rom-Kedar, Transport in a class of n -d.o.f. systems, *Hamiltonian Systems with Three or More Degrees of Freedom (S’Agaró, 1995)*, vol. 533 NATO Adv. Sci. Inst. Ser. C Math. Phys. Sci. Dordrecht: Kluwer Acad. Publ., 1999, 538–543
- [26] Björn Sandstede, Sanjeeva Balasuriya, Christopher K R T Jones, and Patrick Miller, Melnikov theory for finite-time vector fields, *Nonlinearity*, 13.4 (2000), 1357–1377
- [27] Sanjeeva Balasuriya, Approach for maximizing chaotic mixing in microfluidic devices, *Physics of Fluids*, 17.11 (2005), 118103
- [28] Sanjeeva Balasuriya, Cross-separatrix flux in time-a-periodic and time-impulsive flows, *Nonlinearity*, 19.12 (2006), 2775–2795
- [29] Sanjeeva Balasuriya, Gary Froyland, and Naratip Santitissadeekorn, Absolute flux optimising curves of flows on a surface, *Journal of Mathematical Analysis and Applications*, 409.1 (2014), 119–139
- [30] K. A. Mitchell, J. P. Handley, J. B. Delos, and S. K. Knudson, Geometry and topology of escape. II. Homotopic lobe dynamics, *Chaos*, 13.3 (2003), 892–902 arXiv: [0307020](https://arxiv.org/abs/0307020) [\[nlin.CD\]](#)
- [31] K. A. Mitchell, J. P. Handley, B. Tighe, J. B. Delos, and S. K. Knudson, Geometry and topology of escape. I. Epistrophes, *Chaos: An Interdisciplinary Journal of Nonlinear Science*, 13.3 (2003), 880

- [32] Kevin A. Mitchell and John B. Delos, A new topological technique for characterizing homoclinic tangles, *Physica D: Nonlinear Phenomena*, 221.2 (2006), 170–187
- [33] V Rom-Kedar and S Wiggins, Transport in two-dimensional maps, *Archive for Rational Mechanics and Analysis*, 109.3 (1990), 239–298
- [34] W. S. Koon, M. W. Lo, J. E. Marsden, and S. D. Ross, *Dynamical Systems, the Three-Body Problem and Space Mission Design* ISBN 978-0-615-24095-4: Marsden Books, 2008
- [35] Ana M. Mancho, Des Small, Stephen Wiggins, and Kayo Ide, Computation of stable and unstable manifolds of hyperbolic trajectories in two-dimensional, aperiodically time-dependent vector fields, *Physica D: Nonlinear Phenomena*, 182.3-4 (2003), 188–222
- [36] R. S. MacKay, J. D. Meiss, and I. C. Percival, Transport in Hamiltonian systems, *Physica D*, 13 (1984), 55–81
- [37] J. M. T. Thompson and J. R. de Souza, Suppression of escape by resonant modal interactions: in shell vibration and heave-roll capsize, *Proc. R. Soc. Lond. A*, 452 (1996), 2527–2550
- [38] Charles Jaffé, Shane D Ross, Martin W Lo, Jerrold Marsden, David Farrelly, and T Uzer, Statistical theory of asteroid escape rates, *Physical Review Letters*, 89.1 (2002), 011101
- [39] C. Jaffé, S. D. Ross, M. W. Lo, J. E. Marsden, D. Farrelly, and T. Uzer, Theory of asteroid escape rates, *Physical Review Letters*, 89 (2002), 011101
- [40] Jaffé, Charles and Farrelly, David and Uzer, T, Transition state in atomic physics, *Physical Review A*, 60.5 (1999), 3833

Appendix A

A.1 Usage and outputs

This section provides low level details for using *Lober* and processing the output of intersection points and curves. There are two implementation of the equivalence class approach to identifying intersection regions and points. This algorithm is the *-light* mod of Lober. The syntax is

```
lober -light <c1> <c2> <rslt> [ -DENS <nPass> <nDens> ]
```

where <c1> and <c2> are the names of the files containing respectively the curves C_1 and C_2 and <rslt> is the file to be created by Lober to output the results. The optional arguments of the built-in densifier (-DENS <nPass> <nDens>) are described in the next section. The curve are stored in the files in a *Tecplot* ASCII format, i.e.

```
VARIABLES='x','y'  
ZONE T='the curve C1'  
0.2    0.4  
0.23   0.45  
0.35   0.35  
...
```

The output file (`<rs1t>`) will contain one line with 4 numbers: the area of the lobes inside, the area of the lobes outside and the relative error on these two values. This is useful to get an estimate of the error involved in computing the area and provides a first order check of the output. In addition to this, *Lober 1.8* generates 6 output files in *Tecplot* ASCII format with one header line and points arranged in $N \times 2$ array of N points in \mathbb{R}^2 . The intersection points, if it exists and is identifiable for a given point density, are stored in files `c10.dat` and `c20.dat`. The set of points which are on the boundary of $C_1 \cap C_2$ and $C_2 \cap C_1$ are stored in `c11.dat` and `c22.dat` and those are on the boundary of $C_1 \setminus C_2$, $C_2 \setminus C_1$, are stored in `c12.dat` and `c21.dat`.

Chapter 3

Partial control of escaping dynamics: Application to ship roll motion and avoiding capsizes

In collaboration with Shane D. Ross

3.1 Introduction

The control of transient chaos has been of interest in both applied and theoretical studies in various natural and engineering sciences (cite Grebogi, Ott, Yorke and the book on controlling chaos). However, these controlled systems can still exhibit catastrophic events, without any sudden changes in the chaotic attractor, which would be desirable to avoid.

Ship dynamics and capsizes in rough seas has been studied by naval architects for quite some time now (refer some historic papers). More recently, Soliman et al. [41] used geometric techniques of nonlinear dynamics for transient capsizes phenomena and presented safety cri-

teria based on erosion of basin of attraction. While the marine control literature [42] aims at introducing advances in control theory to ship safety, the underlying technology is too sophisticated for use in fishing trawlers or less expensive ocean liners and ferry boats.

The dynamics of large amplitude roll motion involves the nonlinear coupling of a ship's inertia, damping, hydrodynamic resistance, wave and wind moments. Computational study of the underlying phase space structures has been proved to be insightful for the ship capsize and escape from potential well leading to undesirable states. However, it has also been claimed in Ref. [43] that these methods lack predictive ability in terms of *a priori* analytical formulae to avoid capsize.

The control of excessive roll motion of a ship leading to capsize can be traced back to William Froude's work during 1860 when bilge keels were first introduced and used on ship hulls to increase hydrodynamic resistance and act as a passive control mechanism to avoid capsize.

In this work, we attempt to learn if the method of partial control can be useful for feedback control of natural and engineering systems that exhibit escape from a potential well. We also present an approach of incorporating physically relevant forces as discrete disturbance which exacerbates the escape from the potential well. The same question for feedback control implemented using this approach, however, remains unanswered.

3.2 Description of ship roll motion

The full rigid body dynamics of a ship is governed by surge, sway, heave and roll, pitch, yaw as translational and rotational degrees of freedom respectively which are coupled to the surrounding fluid motion. However, in ocean engineering and naval architecture, ship motion and capsize is analyzed by considering roll (ϕ), pitch (θ) and heave (z) as coupled or independent degrees of freedom. This leads to a hierarchy of models, the simplest considering only the roll degree of freedom, with the more complex models considering coupled roll-pitch

motions or even roll-pitch-heave motions.

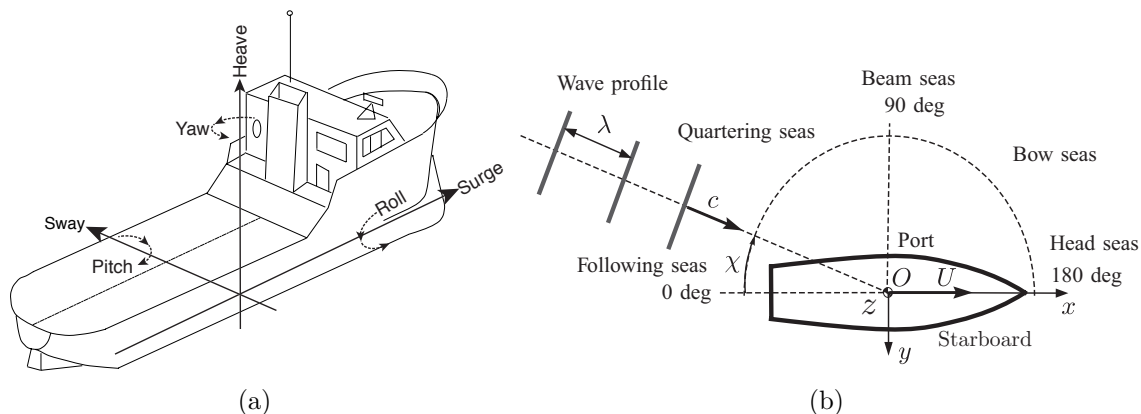


Figure 3.2.1: Schematic of the degrees of freedom of a ship in 4.1(a) and 4.1(b) illustrates the wave characteristics. Adapted from [42].

The dynamics of a ship near the onset of capsizing can be viewed as a large amplitude nonlinear rolling motion when approximations that are valid for the damped and forced system are considered [44]. Thus, considering only the roll degree-of-freedom (DOF) is an adequate assumption based on the fact that rolling motion is predominant over the other degrees of freedom when an observer, located at the center of the ship (pt. O in Fig. 4.1(b)), describes a capsizing ship's motion [45]. Besides, the single DOF model assumption will further our understanding of the methods for avoiding or delaying imminent capsizing in a fully nonlinear coupled model of roll, pitch, and heave. Thus, avoidance of capsizing in the roll DOF model is used as a preliminary step in application of the partial control approach.

In ship design, *capsizing* is defined as the exceeding of the roll angle of a ship when the righting moment, that is the restoring moment due to center of buoyancy and center of gravity, goes to zero. This roll angle is the *roll angle of vanishing stability*, denoted by ϕ_v , which depends on a ship's structural and dynamic parameters. For the purpose of this study, we will focus on a capsized Danish tanker [46], the *Edith Terkol*, and a roll model previously developed by Soliman et al. [41]. The restoring moment and roll angle of vanishing stability for the said ship is shown in Fig. 3.2(a). It is to be noted that capsizing prediction was based on the analysis of calm water characteristics like the restoring moment (typically called the GZ

curve) before dynamic stability analysis was introduced in [41]. The roll model, adopted in [41], is given by

$$\ddot{\phi} = -c_1\phi - c_2|\phi|\phi - c_3\phi^3 - c_4|\phi|\phi^3 - c_5\phi^5 - b_1\dot{\phi} - b_2|\dot{\phi}|\dot{\phi} + \frac{M(t)}{I} + \frac{W_M(t)}{I} \quad (3.2.1)$$

where the, b_i 's and c_i 's are damping and stiffness coefficients, respectively, and we use the specific values in [41] for the *Edith Terkol*: $b_1 = 0.0043$ 1/s, $b_2 = 0.0225$ 1/s², $c_1 = 0.384$ rad²/s², $c_2 = 0.1296$ rad²/s², $c_3 = 1.0368$ rad²/s², $c_4 = -4.059$ rad²/s², $c_5 = 2.4052$ rad²/s², and $I = 1174$ kg-m² is the moment of inertia about the roll axis. The wave and wind moments, $M(t)$ and $W_M(t)$, respectively, are generally modeled as stochastic processes, however, for the purpose of our analysis we first consider them as deterministic forcing. The regular (periodic) wave moment (for more details see [47, 45]) is modeled using

$$m_\phi^{\text{reg}}(t) = \frac{M(t)}{I} = \alpha_0\omega_\phi^2\pi\frac{H}{\lambda}\sin\chi\sin(\omega_e t + \epsilon) \quad (3.2.2)$$

and for which the wave period is given by $T_e = 2\pi/\omega_e$, $\omega_e = 0.527$ rad/s is the encounter frequency (see Sect. B.2 for definition), $\omega_\phi = \sqrt{c_1} = 0.62$ rad/s is the natural roll frequency of the ship, $\alpha_0 = 0.73$ is the (nondimensional) effective wave slope and is assumed constant, H is the wave height (in m) that will be used for parametric study, $\lambda = 221.94$ m is the wavelength of the sea, χ is the incident angle of the waves called encounter angle and ϵ is the phase of beam sea wave used to account for different positions of the ship in the traveling wave.

To motivate the present study, let us express (3.2.1) in non-dimensional form and express the restoring moment in the form of a potential energy. Let us use the natural roll frequency as the time-scale, $t_\phi = 1/\omega_\phi$, to obtain the new time variable \bar{t} as

$$\bar{t} = \frac{t}{t_\phi} = t\omega_\phi \quad (3.2.3)$$

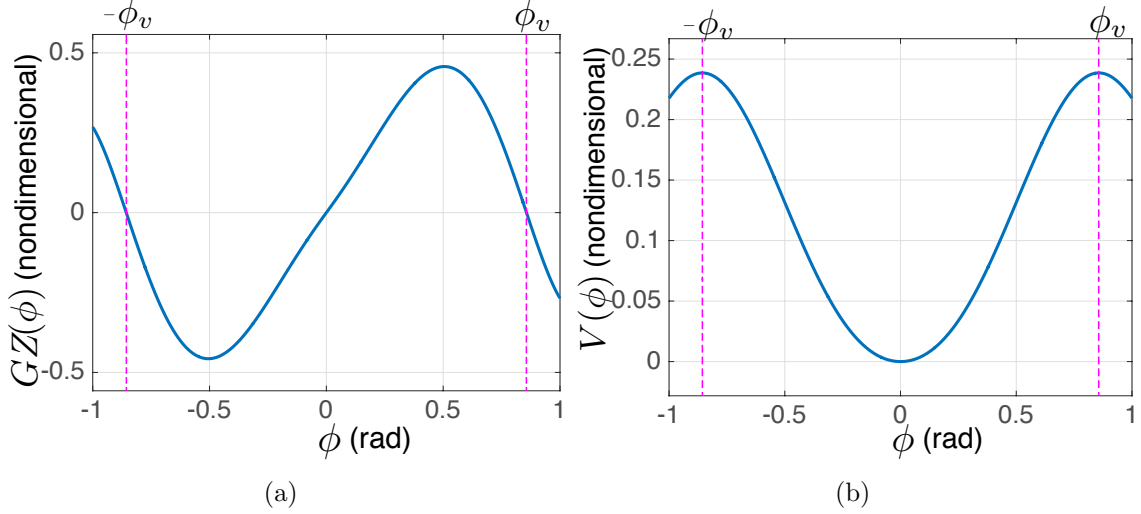


Figure 3.2.2: The restoring moment, $GZ(\phi)$, for the ship *Edith Terkol* is shown in (a) and the roll angle of vanishing stability, ϕ_v denotes the roll angle when the restoring moment goes to zero. The potential energy, $V(\phi)$, that underlies the restoring moment and the roll angle of vanishing stability is shown in (b).

and thus, the roll model becomes

$$\ddot{\phi} = -\phi - \bar{c}_2|\phi|\phi - \bar{c}_3\phi^3 - \bar{c}_4|\phi|\phi^3 - \bar{c}_5\phi^5 - \bar{b}_1\dot{\phi} - \bar{b}_2|\dot{\phi}|\dot{\phi} + \bar{H}\sin(\bar{\omega}t) \quad (3.2.4)$$

where $\dot{\phi} \equiv \frac{d\phi}{dt}$, $\ddot{\phi} \equiv \frac{d^2\phi}{dt^2}$, and the eight nondimensional parameters are $\bar{c}_i = c_i/\omega_\phi^2$ ($i = 2, 3, 4, 5$), $\bar{b}_1 = b_1/\omega_\phi$, $\bar{b}_2 = b_2$, $\bar{\omega} = \omega_e/\omega_\phi$, and $\bar{H} = \alpha_0\pi\frac{H}{\lambda}$. We can view the ϕ -dependent portion, that is the restoring moment $GZ(\phi)$, of the right-hand-side of (3.2.4) as coming from a potential energy,

$$V(\phi) = \frac{1}{2}\phi^2 + \frac{\bar{c}_2}{3}|\phi|\phi^2 + \frac{\bar{c}_3}{4}\phi^4 + \frac{\bar{c}_4}{5}|\phi|\phi^4 + \frac{\bar{c}_5}{6}\phi^6 \quad (3.2.5)$$

as in Fig. 3.2(b), so that (3.2.4) can be written as

$$\ddot{\phi} = -\frac{dV}{d\phi} - \bar{b}_1\dot{\phi} - \bar{b}_2|\dot{\phi}|\dot{\phi} + \bar{H}\sin(\bar{\omega}t) \quad (3.2.6)$$

Notice that from the symmetrical potential $V(\phi)$, there are symmetrical unstable equilibria

at $\phi_v = \pm 0.8561$ rad. This is slightly less than the value of ± 0.88 rad reported in [47]. While the unstable equilibria can be used as the threshold for stability of a ship, for the purpose of comparison, we use the value adopted in [47], [41]. We note that [41] merely claimed that they ‘chose’ $\phi_v = 0.88$ rad to correspond to capsize, not because it coincided with the unstable equilibrium, but because this was the roll angle at which the ship actually capsized. We can transform the ordinary differential equations (3.2.6) into first-order form given by

$$\begin{aligned}\dot{\phi} &= \omega \\ \dot{\omega} &= -\frac{dV}{d\phi} - \bar{b}_1\omega - \bar{b}_2|\omega|\omega + \bar{H}\sin(\bar{\omega}t).\end{aligned}\tag{3.2.7}$$

We will use one period of the wave forcing, $\bar{T} = 2\pi/\bar{\omega}$, to define a stroboscopic time- \bar{T} map f given by $(\phi(0), \omega(0)) \mapsto (\phi(\bar{T}), \omega(\bar{T}))$. Since $\phi \in S^1$ and $\omega \in \mathbb{R}$, the dynamical system lives on the cylinder, $S^1 \times \mathbb{R}$. However, we will only consider a subset, $D \subset S^1 \times \mathbb{R}$ (for example $D = [-\phi_v, \phi_v] \times \mathbb{R}$), based on the idea that motion beyond roll angle of vanishing stability has no relevance from the control of capsize perspective since at that point, unavoidable capsize has already occurred.

Let us consider the geometric picture of trajectories that lead to the inevitable capsize of a ship. This is typically studied in terms of an exit basin (cf. [48],) which shows regions of phase space that do not lead to capsize for a given time of the flow and will be denoted as the *non-capsize basin*. The erosion of non-capsize basin is the crux of transient capsize study in [41] who used 16 wave periods and different wave heights for predicting loss of ship’s stability. However, for a ship with limited control authority in periodic waves, we assume 1 wave period as the time scale to avoid capsize. Thus, we show the non-capsize basin for three different wave heights in Fig. 3.2.3 for the 1 wave period which agrees with the result of [41]. The non-capsize basin for 1 wave period provides the set of initial conditions for a ship to sustain the rolling motion in periodic waves. Thus, if we start a ship’s rolling motion in the non-capsize basin, the ship will not capsize during the next wave period and if the state

wanders off we should only then apply a control to bring it back into the non-capsize basin. Thus, the objective of keeping a ship safe, in presence of disturbance, can be understood

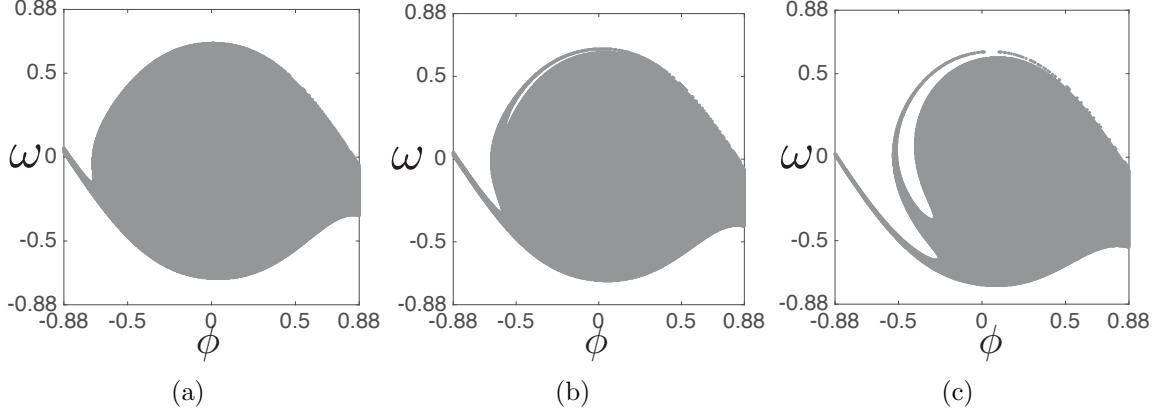


Figure 3.2.3: Non-capsize basin in the phase space of roll model where the gray region denotes initial conditions that do not lead to capsizing during $1 \bar{T}$ (nondimensional wave period) for wave heights $H = 3.28$ m, $H = 4.92$ m, and $H = 9.84$ m in Fig. 3.3(a)- 3.3(c). The parameters are for the ship *Edith Terkol* and it should be noted that in Fig. 3.2.3, the nondimensional wave period corresponds to beam seas ($\chi = 90$ deg), so the ship's forward speed has no effect on the encounter frequency which is equal to the wave frequency ([42, chap.2]) in beam seas. This means the non-capsize basin for waves of different heights are incident on the ship at same encounter frequency.

as keeping the states of rolling motion inside the non-capsize basin for a given wave height. If this approach can be repeated for all the successive wave periods, the ship can avoid inevitable capsizing. Hence, control strategies for capsizing will benefit from understanding the specific structure of the non-capsize basin. This can be explained using a geometric view of how regions get mapped out of the right and left boundaries which denote the roll angle of vanishing stability. First to verify the non-capsize basin, let us consider the boundaries

$$n_+ = \{(\phi_v, \omega) \mid -0.88 \leq \omega \leq 0.88\} \quad (3.2.8)$$

$$n_- = \{(-\phi_v, \omega) \mid -0.88 \leq \omega \leq 0.88\} \quad (3.2.9)$$

which are shown in Fig. 3.4(a). By definition of construction of the non-capsize basin shown as the gray set in Fig. 3.4(a), the pre-image of the left and right boundaries are the initial conditions that get mapped to the boundary. Thus, the non-capsize basin is outlined by the

pre-image, in $t = \bar{T}$, of points on the boundary and the stripes near the top and bottom of the domain denote regions which are mapped to the boundary in time, $t < \bar{T}$. Furthermore, to elucidate the phase space structure of the non-capsize basin, we can use the approach of lobe dynamics which was developed in [7, 6] for explaining chaotic transport in phase space. The theory of lobe dynamics is based on the intersection and segments of invariant manifolds of the perturbed saddle equilibrium points, which form lobes and their forward and backward iterates under the map. When we consider the unforced form of (3.2.7), the manifolds do not intersect and form the boundary between bounded and unbounded motion. The initial conditions in the region of bounded motion (basin of attraction of the center sink denoted as p_0 in Fig. 3.4(b)) corresponds to rolling motion that will eventually die out due to damping while those in the region of unbounded motion will lead to inevitable capsizes. However, with addition of periodic forcing, basin of attraction of the center sink, p_0 , gets eroded by successive fragmentation due to the lobes. This is shown in Fig. 3.4(c) as the lobe $L_{b,u}^t(1)$ between the intersection point, q^t , (boundary intersection point or *bip* with superscript denoting top segments of the manifolds) and the intersection point, q_1^t (primary intersection point or *pip*). The other lobe $L_{b,u}^b(1)$ is formed between the points q_1^b and $f^{-1}(q^b)$ from the bottom segments of the manifolds. In 1 forward iterate of the stroboscopic time- \bar{T} map f , regions inside the lobes will get mapped outside region of the bounded motion (region bounded by the perturbed manifolds intersecting at p_{\pm} , q^t and q^b) into region of unbounded motion. Since the present study is concerned with only regions inside the domain D and that leaves it in 1 forward iterate, we only get a subset of the second lobe that maps outside our domain. The forward mapping out of the domain using the two lobes is explained in the schematic Fig. 3.4(d). Thus, the invariant manifolds and lobe dynamics elucidate the geometric structure of non-capsize basin that forms the basis for avoiding capsizes. Next, we consider a much worse scenario where a random disturbance acts along with the harmonically varying regular wave forcing. Our objective is to adopt the approach of *partial control* for avoiding capsizes in the presence of a random disturbance using a control which is smaller

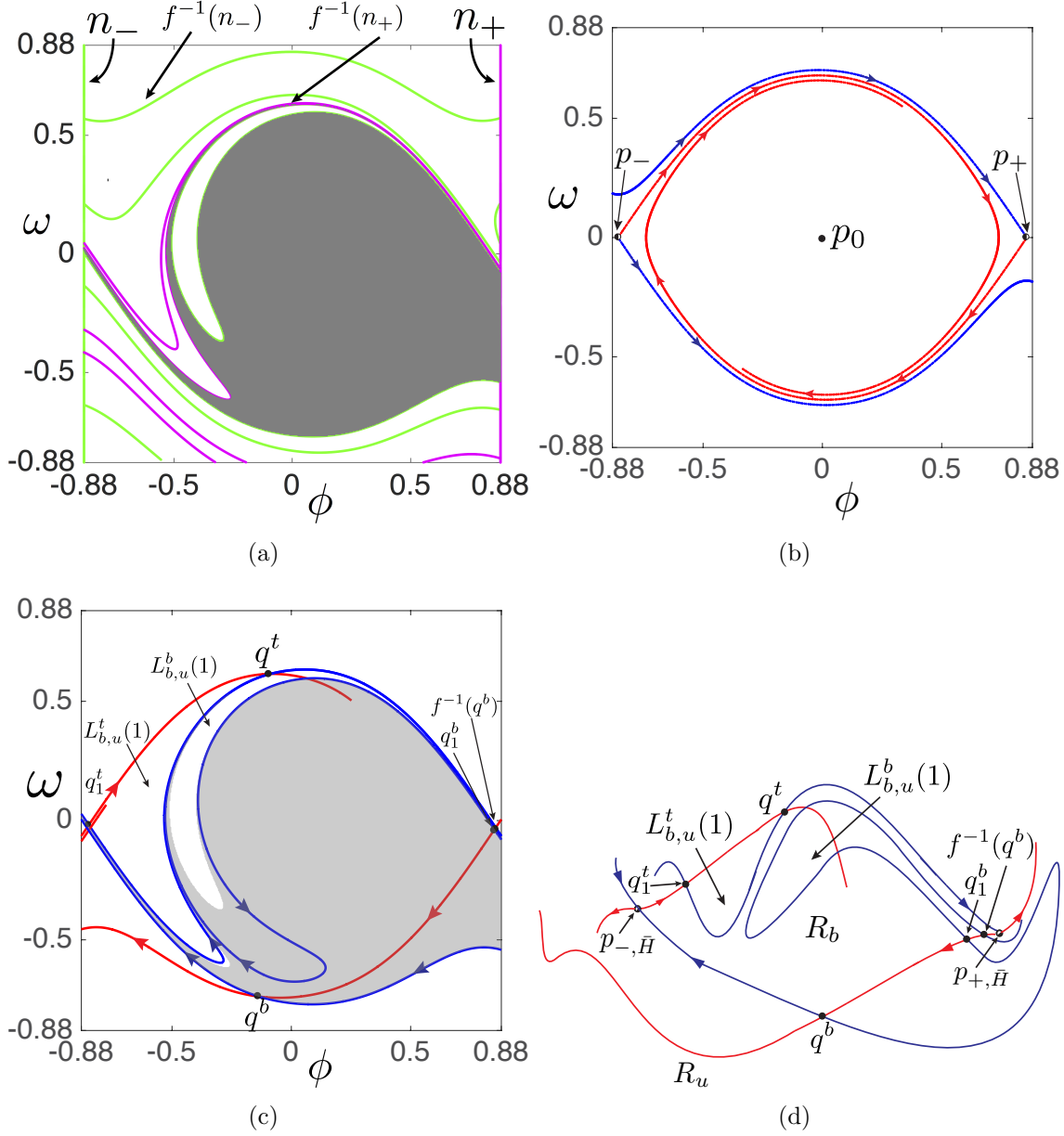


Figure 3.2.4: (a) Pre-image of the left (green) and right (magenta) boundaries for a wave height of $H = 9.84$ m and the non-capsizing basin shown as the gray region. (b) Invariant manifolds for the unforced form of roll model (3.2.7) where the red curves denote the unstable and blue denotes the stable manifolds of the saddle p_{\pm} , respectively. Due to damping, stable and unstable manifolds of the saddles are not connected by a heteroclinic orbit and instead unstable manifolds connect to the center sink at p_0 .

than the disturbance.

3.3 Partial control of escaping dynamics:

The model (3.2.7) for a ship's rolling motion does not take into account effects of higher order coupled fluid-structure interaction, nonlinear coupling of other degrees of freedom and the wind moment. However, in a practical situation, we can estimate an upper bound for these disturbances using information on sea conditions and a ship's response to such forcing. Once this upper bound is obtained, which we refer to as the upper bound on discrete disturbance magnitude ξ_{max} acting at the end of the time- \bar{T} map, it is of interest to ascertain the safety of a ship given an upper bound on the discrete feedback control, u_{max} , particularly for the case $u_{max} < \xi_{max}$. We note here that if $u_{max} \geq \xi_{max}$, one could merely apply a control to exactly cancel disturbances, $u_{max} = -\xi_{max}$, to guarantee safety, so we do not consider this case.

The case of smaller controls than disturbances is where the partial control framework (put forward in [49, 50, 51, 52]) can be applied. More importantly, we only need the upper bounds of a random disturbance, and control to obtain regions in the phase space domain D such that an appropriate control can be found which avoids capsizing for any possible sequence of the bounded disturbance. In fact, when this region in phase space exists it is referred to as the safe set, S .

We present a mathematical description of this framework for the sake of completeness (see also Sabuco *et al.* in [52, 51]). Let us consider we want to keep the dynamics in a closed and bounded domain Q , a subset of the domain D , which is in the phase space $\Omega \subset \mathbb{R}^k$. There is a map $f : \Omega \rightarrow \Omega$, acting on the points $\mathbf{q}_n \in \Omega$ such that the discrete map from time n to time $(n + 1)$ is

$$\mathbf{q}_{n+1} = f(\mathbf{q}_n) \tag{3.3.1}$$

We assume this iterate of the map is acted upon by a bounded disturbance vector, often considered to be derived from a random noise, ξ_n and an appropriately chosen feedback

control vector, \mathbf{u}_n . This generates the *admissible trajectory* and given by

$$\mathbf{q}_{n+1} = f(\mathbf{q}_n) + \boldsymbol{\xi}_n + \mathbf{u}_n \quad (3.3.2)$$

where, $\boldsymbol{\xi}_n \in \mathcal{B}_k(\xi_{max})$ and $\mathbf{u}_n \in \mathcal{B}_k(u_{max})$ are called the *admissible disturbance* and *admissible control* respectively where $\mathcal{B}_k(r)$ is the closed ball of radius r around the origin in \mathbb{R}^k , and where $u_{max} < \xi_{max}$. With the constraints on the disturbance and control, we call a set $S \subset Q$ *safe set* if for each initial point $\mathbf{q}_0 \in S$ there is an *admissible trajectory*, $\{\mathbf{q}_1, \mathbf{q}_2, \dots\}$ where $\mathbf{q}_n \in S$ for all $n \geq 1$. This safe set is computed using an iterative algorithm that converges to the safe set S . We show the pseudo-code in Procedure 1 (cf. [51]) and is called safe set sculpting. Once the safe set is computed, for a given ξ_{max} and u_{max} , using this procedure

Procedure 1 Safe set sculpting algorithm

Input: Set initial set, $C_1 = Q$, and $i = 1$, maximum iteration, i_{max} and number of bad points in Q , $N_{cut} \neq 0$

while $i \leq i_{max}$ **do**

Fatten the set, C_i by maximum control magnitude u_0 so, $C'_i = C_i + u_{max}$.

Shrink the set, C'_i by disturbance ξ_0 so, $C''_i = C'_i - \xi_{max}$.

Cut the unsafe subsets of the set, C_i . A subset is unsafe if there exists $q \in C_i$ such that $\mathbf{f}(q) \notin C''_i$.

Compute number of unsafe points removed in this iteration, N_{cut} and set $C_{i+1} = C_i$ and update, $i = i + 1$.

end while

we can obtain the control, \mathbf{u}_n , and controlled trajectory, $\mathbf{q}_n, n \geq 1$ for any sequence of the disturbance.

3.3.1 Tent map example

Before proceeding to a ship's rolling motion, let us consider the tent map, a prototypical example, from classical dynamical systems, to understand the main strategy of partial control.

The one-dimensional tent map is defined as $f : \mathbb{R} \rightarrow \mathbb{R}$, where

$$f(q) := 3 - 3|q| \quad \text{and} \quad q \in \mathbb{R}, \quad \text{so} \quad q_{n+1} = 3 - 3|q_n| + \xi_n + u_n$$

and we want the iterates of an initial condition to stay in a chosen set, $Q = [-3/2, 3/2]$. Since the iterates of any initial condition diverge to $-\infty$ in absence of control, it is non-trivial to keep the trajectory in the given Q . However, using the safe set sculpting algorithm we find the safe set to be $S = \{-1, 1\}$ in presence of disturbances with upper bound, $\xi_0 = 2$ and control upper bound, $u_0 = 1$. This means we can always keep the iterates of the initial conditions in $S \subset Q$ by applying u_n , where $|u_n| \leq u_0$, in presence of a disturbance ξ_n , where $|\xi_n| \leq \xi_0$. For a practitioner, the safe set S and the upper bounds are the *a priori* information that is required to avoid catastrophic events.

3.4 Application to ship rolling motion and capsizing

In this section, we develop the ingredients for applying partial control to avoid capsizing of a ship for two cases: (1) a regular sea (train of periodic waves) with some uncertainty in wave height and (ii) an irregular sea (train of random waves) that represents rough sea conditions. This study will be performed for the capsized Danish tanker *Edith Terkol* but the ingredients can be suitably altered for other capsized vessels to test the viability of partial control. Based on the earlier discussion on roll angle of vanishing stability, we will adopt the domain $D = [-0.88, 0.88] \times [-0.88, 0.88]$ for computation of the safe sets. This is chosen as such since roll angle exceeding the roll angle of vanishing stability will mean leaving the domain from either the left or right boundary.

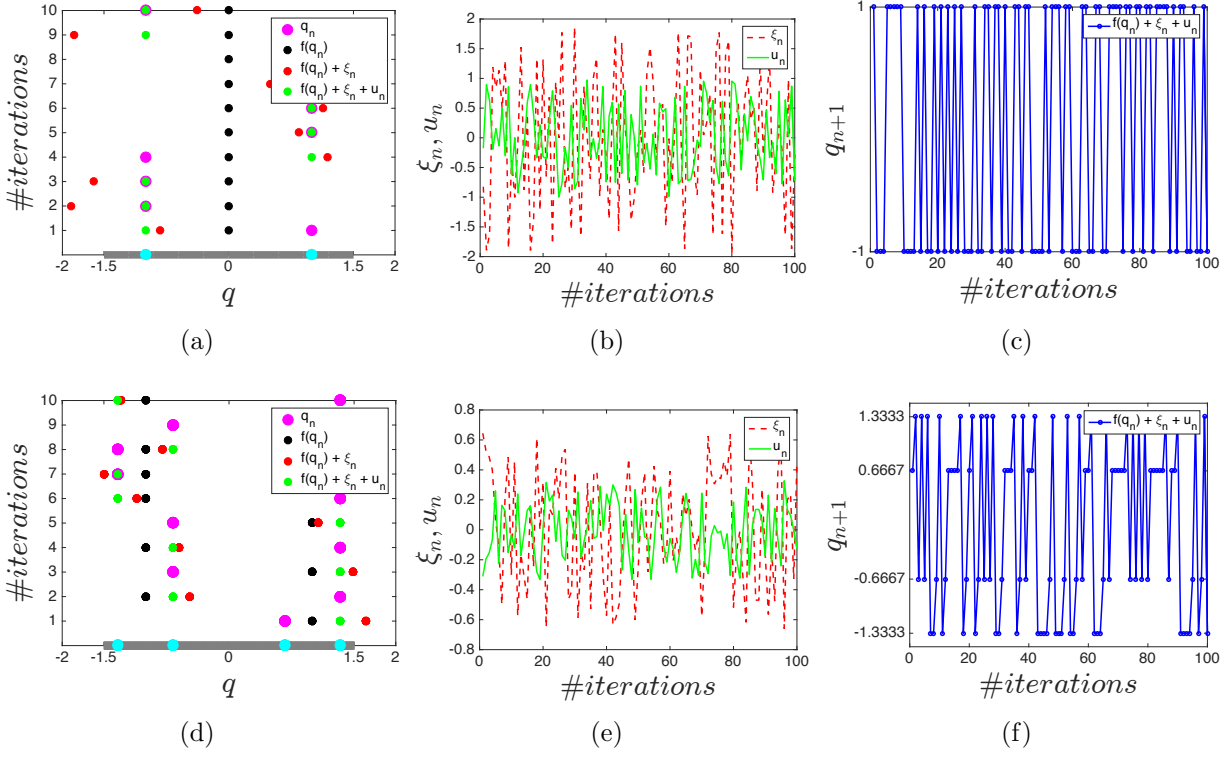


Figure 3.3.1: Partial control applied to slope-3 tent map with $Q = [-1.5, 1.5]$ as the region we want to keep the admissible trajectory. Figs. (a), (b), and (c) shows the first 10 iterations, the admissible disturbance that acts at each iteration and the admissible control that is applied at each iteration, and the obtained admissible trajectory for 100 iterations, respectively, for $\xi_{\max} = 2$, $u_{\max} = 1$. Figs. (d), (f), and (e) shows the same for $\xi_{\max} = 2/3$, $u_{\max} = 1/3$. Figs. (a) and (d) show Q as the grey closed set on \mathbb{R} , and the cyan dots are the safe set, S which is either $\{-1, 1\}$ or $\{-1 - 1/3, -1 + 1/3, 1 - 1/3, 1 + 1/3\}$ for the two cases, respectively. The black dot denote iterates of the tent map while the red dots denote points after disturbance has acted on the iterate. The admissible trajectory is shown as green dots which are in S and hence in Q , and obtained using control that is always less than the disturbance as shown in Figs. (b) and (e).

Regular sea

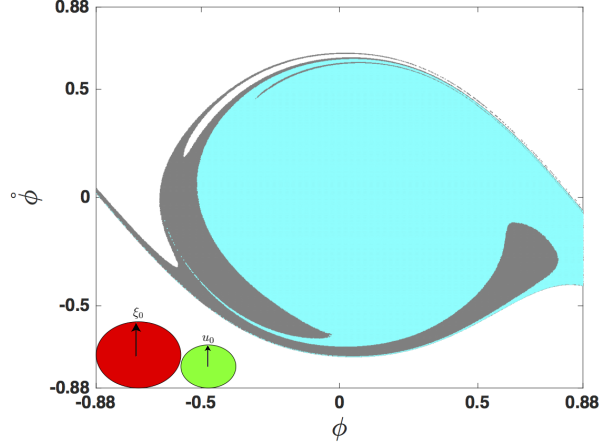
We consider the ship is experiencing a train of periodic waves at an encounter angle of $\chi = 90$ deg, typically called beam waves. In addition to the periodic forcing, we assume a disturbance of certain magnitude acts on the ship at the end of each wave period. This can be interpreted as the effect of small variations, which is distributed over the period, in the wave height. This scenario will eventually cause a ship to capsize, that is escape the

potential well, if appropriate control measures are not adopted. To this end, we apply the partial control approach to avoid escape from the potential well.

The basic ingredients for applying partial control is the map f , a region of the phase space where f acts, admissible disturbance and admissible control. We will resolve these ingredients one at a time. In the case of regular seas, the ship roll dynamics is converted into a two-dimensional map by considering the flow over 1 wave period. Furthermore, a ship capsizes when the roll angle exceeds the roll angle of vanishing stability, $\phi_v = 0.88$ rad and we are interested in the region where initial conditions do not lead to capsize in 1 wave period. Since, with the repetitive application of the discrete control we can keep the trajectory away from capsize.

This non-capsizing set constitutes the region where we want to sustain the ship's rolling motion with a given disturbance. This set is identical to the basin used in transient capsize analysis for 1 wave period except our goal is to keep a ship's motion in this set in presence of a disturbance. The initial set for a wave height of $H = 4.92$ m for *Edith Terkol* (refer section on description of roll model for other parameters) is shown in Fig. 3.4.1.

A point to note here is that the safe sets are computed for a given ξ_{\max} and u_{\max} and initial set, Q . To initialize the computations, we add ξ_{\max} to the map f such that all safe states in Q become unsafe. For this upper bound of disturbance, we initialize u_{\max} near ξ_{\max} and sculpt the safe set. This procedure is repeated with successive lower values of u_{\max} until there are no safe sets and the value of u_{\max} at which this occurs is called the minimum control required for the safe set to exist, u_{\max}^{\min} . Furthermore, when a trajectory is partially controlled the long term behavior is of interest as that denotes the region of the safe set that is visited by the admissible trajectory as $t \rightarrow \infty$.



(a) Initial set, Q

Figure 3.4.1: Fig. 3.1(a) shows the initial set (also referred in [41] as the safe basin) under the wave forcing for $1 T_e$, $H = 4.94$ m. Final safe set (blue region) shown here denote the initial conditions that are for a control upper bound, $u_{\max} = 0.096988$ and disturbance, $\xi_{\max} = 0.15314$ with safe ratio, $\rho = 0.63$. The grid resolution was 1001×1001 and the wave height $H = 4.92$ m. The control upper bound is very close to the minimum value of $u_0^{\min} = 0.096477$ below which the safe set vanishes.

Rough sea

In order to relate the notion of discrete disturbance, ξ_{\max} , with continuous random wave forcing, we need to accumulate the contribution over a time range in a systematic approach. When a ship encounters realistic high seas, which are aperiodic, the forcing can be interpreted as a sum of the system without any waves and the discrete disturbance, ξ_n applied at the end of a given time length. It is at this instant that the feedback control, u_n , is applied and just enough to avoid catastrophic event like capsize due to roll exceeding the angle of vanishing stability.

For the roll model, the random sea waves are generated from an energy spectrum and modeled as time-dependent angular accelerations affecting the roll DOF as

$$m_\phi(t) = \omega_\phi^2 \sin \chi \alpha_0 \frac{\sqrt{2d\omega}}{g} \sum_{i=1}^N \omega_i^2 \sqrt{S(\omega_i)} \sin(\omega_i t + \epsilon_i) \quad (3.4.1)$$

where, ω_ϕ is the natural roll frequency for a ship (here, *Edith Terkol*) and $S(\omega_i)$ is the

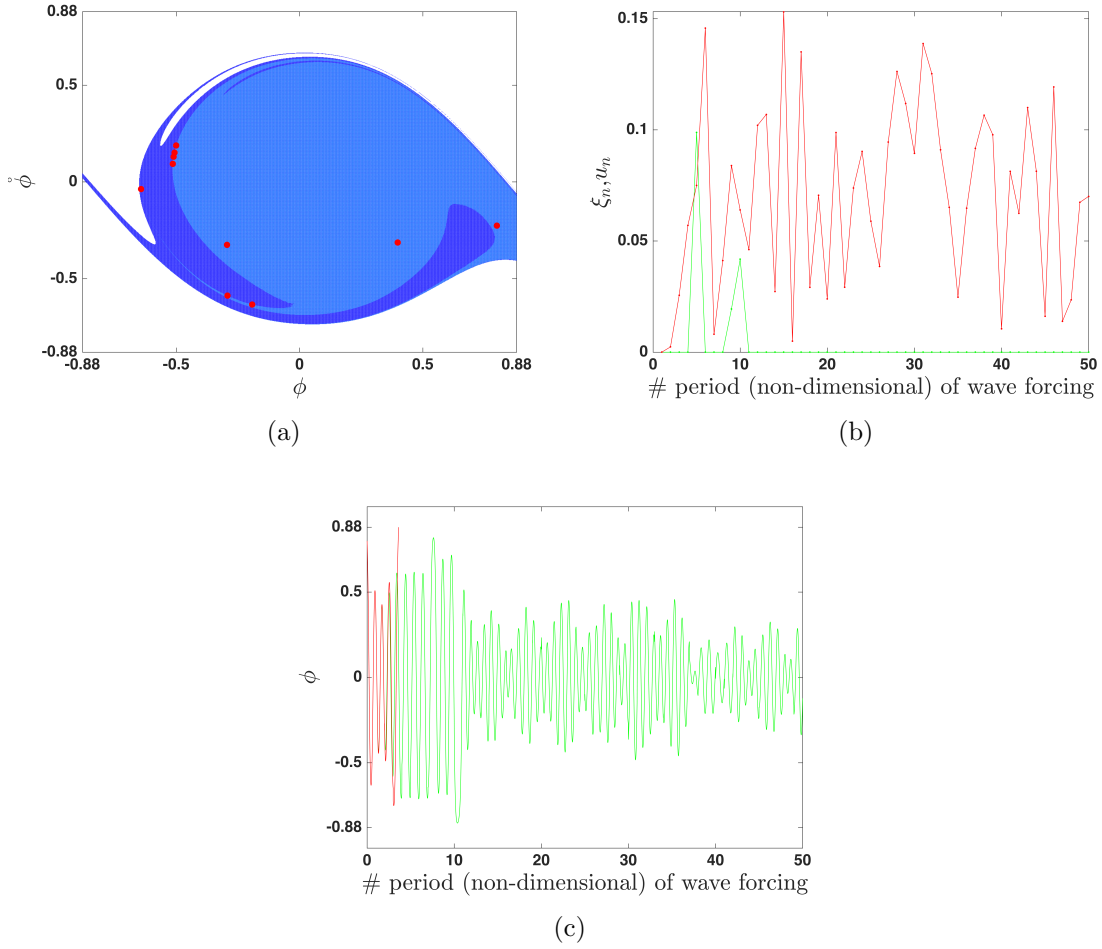


Figure 3.4.2: Fig. 3.2(a) shows the initial set, Q (as blue region), and the controlled trajectory (marked as black x). Q is the set of initial condition that don't lead to capsize over 1 period of the regular sea of 4.94 m wave height. The noise is assumed to be uniformly distributed with upper bound of $\xi_{\max} = 0.15314$ and acts at the end of every period as shown (in red) in Fig. 3.2(b).

wave energy spectrum, known as *Pierson-Moskowitz* spectrum [defined here](#), that generates a particular sea environment and is given by

$$S(\omega_i) = 0.11 H_s^2 \frac{\omega_z^4}{\omega_i^5} \exp\left(-0.44 \left(\frac{\omega_z}{\omega_i}\right)^4\right) \quad (3.4.2)$$

and shown in Fig. 4.4(a). The encounter frequency (frequency experienced by the ship's

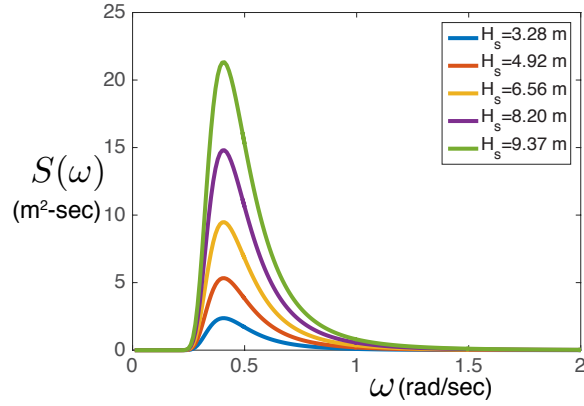


Figure 3.4.3: Ocean wave spectrum given by Eqn. (4.3.4) that is used to generate the continuous wave forcing in rough seas.

reference frame) is given by

$$\omega_{ie} = \omega_i - \frac{\omega_i^2 U}{g} \cos \chi \quad (3.4.3)$$

where, U is the ship's speed and χ is the heading angle of the waves with respect to the ship. Using a discrete approximation to the continuous spectrum, given by Eqn. (4.3.4), we generate a train of aperiodic signals that simulate a rough sea.

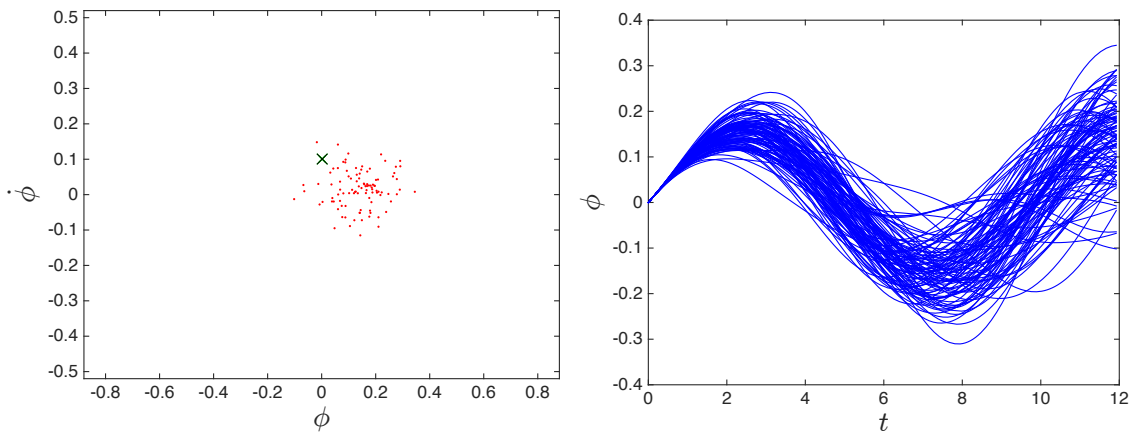


Figure 3.4.4: The wave energy spectrum of the rough sea used in the computations. A sample ensemble of trajectories for random sea waves of significant height, $H = 4.94\text{m}$

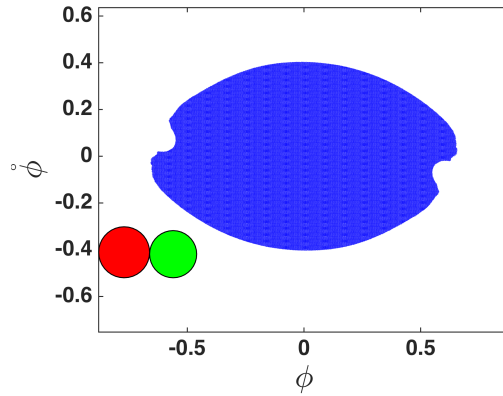


Figure 3.4.5: Safe set for rough seas of wave height $H_s = 4.94$ m while the partial control time, $t_{pc} = 2$ secs obtained for a safe ratio of 0.925

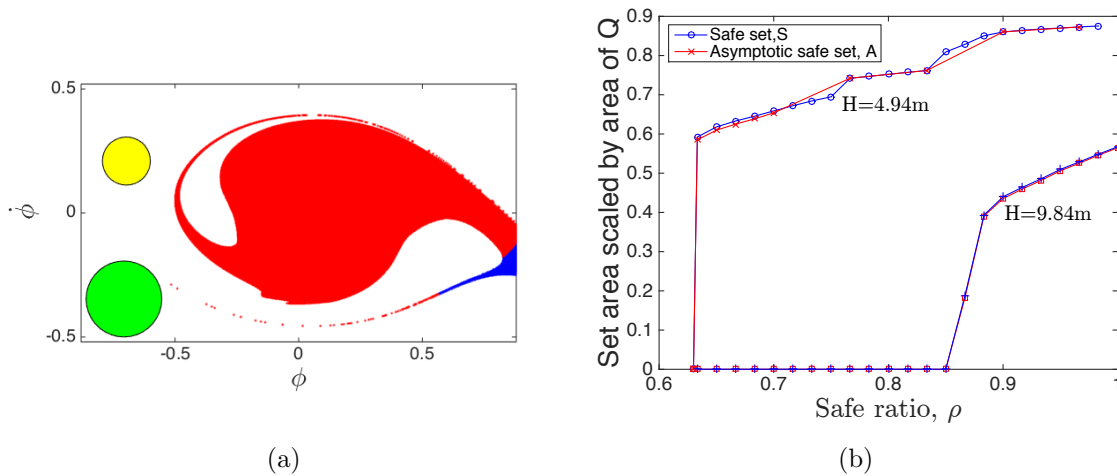


Figure 3.4.6: Figures showing the safe set and asymptotic safe set which is almost equal to the safe set.

3.5 Conclusions

In this article, we present geometric approach of understanding escape from a potential well in the context of a ship motion and capsize using a single degree of freedom model. This is a classical model in naval architecture and ocean engineering with promising results on predicting capsize of a ship in regular and rough sea. Our contribution is the consideration of disturbance, that accounts for unmodeled effects, on the non-capsize basin (typically called safe basin). We also present the application of a control approach that is based on avoiding capsize using a control smaller than the disturbance. This has implications for large amplitude roll motions, and can provide guiding principles for designing avoidance strategies in rough seas.

3.6 Acknowledgments

This work was supported by the National Science Foundation under award 1150456 and 1537349. The authors would like to thank Tom Battista, Craig Woolsey, Leigh McCue, and Michele Cooper for useful discussions.

References

- [6] Stephen Wiggins, *Chaotic transport in dynamical systems*
- [7] Vered Rom-Kedar, Anthony Leonard, and Stephen Wiggins, An analytical study of transport , mixing and chaos in an unsteady vortical flow, *Journal of Fluid Mechanics*, (1990)
- [41] Mohamed S. Soliman and J. M. T. Thompson, Transient and steady state analysis of capsize phenomena, *Applied Ocean Research*, 13.2 (1991), 82–92

- [42] Tristan Perez, *Ship Motion Control* Springer-Verlag
- [43] C. Jiang, A. W. Troesch, and S. W. Shaw, Capsize criteria for ship models with memory-dependent hydrodynamics and random excitation, *Philosophical Transactions of the Royal Society A: Mathematical, Physical and Engineering Sciences*, 358.1771 (2000), 1761–1791
- [44] Jeffrey M. Falzarano, Steven W. Shaw, and Armin W. Troesch, Application of global methods for analyzing dynamical systems to ship rolling motion and capsizing, *International Journal of Bifurcation and Chaos*, 2 (1992), 101–115
- [45] I. Senjanovic, G. Cipric, J. Parunov, and J. Senjanovic, I. and Cipric, G. and Parunov, Survival Analysis of Fishing Vessels Rolling in Rough Seas, *Philosophical Transactions: Mathematical, Physical and Engineering Sciences*, 358.1771 (2000), 1943–1965
- [46] Luis Perez-Rojas, Sara Sastre, and Ainara Martin, Review of the ship accidents investigations presented at the STAB presented at the STAB, *Proceedings of 10th International Ship Stability Workshop*, (2008), 219–233
- [47] LS McCue, Applications of finite-time Lyapunov exponents to the study of capsizing in beam seas, *Contemporary Ideas on Ship Stability and Capsizing in waves*, (2011), 1–9
- [48] Mattia Coccolo, Jesús M. Seoane, Samuel Zambrano, and Miguel a. F. Sanjuán, Partial Control of Escapes in Chaotic Scattering, *International Journal of Bifurcation and Chaos*, 23.01 (2013), 1350008
- [49] Juan Sabuco, Samuel Zambrano, Miguel A F Sanjuán, and James A Yorke, Finding safety in partially controllable chaotic systems, *Communications in Nonlinear Science and Numerical Simulation*, 17.11 (2012), 4274–4280
- [50] Juan Sabuco, Samuel Zambrano, and Miguel A F Sanjuán, Partial control of chaotic transients using escape times, *New Journal of Physics*, 12.11 (2010), 113038
- [51] Juan Sabuco, Miguel a F Sanjuán, and James a Yorke, Dynamics of partial control. *Chaos (Woodbury, N. Y.)*, 22.4 (2012), 047507

- [52] Juan Sabuco, Samuel Zambrano, Miguel a.F. Sanjuán, and James a. Yorke, Finding safety in partially controllable chaotic systems, *Communications in Nonlinear Science and Numerical Simulation*, 17.11 (2012), 4274–4280

Appendix B

B.1 Wave height parameter

The wave height parameters defined in ocean engineering and nonlinear dynamics literature for the modeling of regular waves need to be connected for comparing previously published results.

$$H_{ST} = \bar{H} = \alpha_0 \pi \frac{H}{\lambda} \quad (\text{B.1-1})$$

where, H_{ST} is the non-dimensional wave height parameter adopted in [41] as $H_{ST} = H_s h$. In case of regular waves, which are modeled as periodic/sine waves, the notion of significant wave height does not hold and we refer to H as wave height parameter and *double-amplitude* (brief description in Sect.2.2 in [42]) as the wave height.

B.2 Modeling wave excitation

If a ship is still relative to the waves, the sea wave frequency experienced by an observer in the ship is exactly as the wave frequency, ω_w . However, if the ship is moving with a velocity component in the direction of propagating wave, the observer experiences the *encounter*

frequency, ω_e due to Doppler effect and is given by

$$\omega_e = \omega_w - \frac{\omega_w^2 U}{g} \cos(\chi) \quad (\text{B.2-1})$$

where, U is the average velocity of the ship, and g is acceleration due to gravity.

B.3 Algorithm for obtaining initial set

For the ship capsize problem, a state is called **safe** if the instantaneous roll angle is less than the critical roll angle $|\phi_t| < \phi_{critical}$ in the next wave encounter cycle. Thus, a capsize state is when the roll angle $|\phi_t|$ exceeds or equals $\phi_{critical}$, which for the ship *Edith Terkol* is 0.88 rad. Based on the conclusion from the non-dimensional potential shown in Fig. 3.2.2, we consider the domain $[-0.88, 0.88] \times [-0.52, 0.52]$ where the ship remains safe under the disturbance ξ_n and using the control u_n . We define the closed and bounded initial set, Q , as the set of points p in the domain that are safe for all $t \in [0, 1 T_e]$. This step of the partial control algorithm is referred to as *grid generator* described in Alg. 2. and the initial set is shown in Fig. 3.1(a).

Procedure 2 Pseudo-code to obtain the initial set and its image

Set parameter values and no of grid points, N^2

for all $i \in 1 : N$ and $j \in 1 : N$ **do**

Set initial condition to $(\phi_i, \dot{\phi}_j)$ and integrate for time mT , with the event function $|\phi| - \phi_{critical}$

Check for all directions of the event crossing, terminate integration if satisfied.

If event state vector is not empty, $(\phi_i, \dot{\phi}_j)$ initial condition is in capsize/forbidden region.

end for

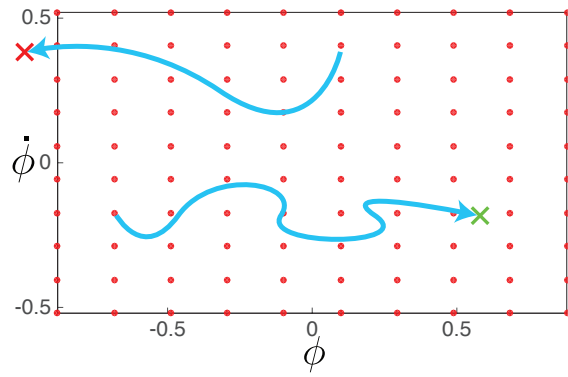


Figure B.3.1: Showing the algorithm 2 as a schematic for computing the initial set Q .

Chapter 4

Cylindrical manifolds and partial control: Application to coupled roll-pitch ship motion

In collaboration with Shane D. Ross

4.1 Introduction

Ship dynamics and modeling. Since ancient times ships have remained a crucial element in all arenas of life and society and hence the problem of ship capsizing has received considerable attention to avoid catastrophe while out at sea. Initially, this problem was tackled assuming a linear response, and stability of a ship was analyzed under steady state assumptions. However, the results from linear analysis only remain true for small amplitude motion and underestimate the critical conditions leading to capsizing, which are primarily large amplitude, complicated nonlinear phenomena [41]. The primary objective of analyzing such models for different sea states is to generate initial conditions that lead to imminent capsizing, or predict

a range of parameter values that should be avoided to retain stability [53]. These models are typically analyzed using the computational and semi-analytical approaches that use the geometric features of the phase space such as the *basin of attraction*, and *basin boundary*. These concepts give rise to tools for analyzing ship capsizes, such as the *transient capsize diagram*, the *index of capsizability*, and *integrity measure* [12]. The major traction for these concepts and tools is that they are conceptually simpler for obtaining initial conditions leading to capsizes, and they also provide realistic prediction of transient behavior of capsizes via the fractal like structure of the basin boundary as opposed to steady state analysis. For design engineers, this approach can serve as a first step towards a comprehensive investigation using either physical model tests or extensive numerical solutions of coupled fluid-vessel models. Furthermore, for control engineers, the geometric view point provides critical regions in the phase space that should be avoided for safety in rough seas.

Capsize criteria and analysis. Typically, a ship's static stability is governed by the GZ-curve which is dependent on the heel angle and provides a measure of the restoring moment experienced by the ship when disturbed from its equilibrium position. Hence, stability analysis based on the GZ-curve is an important first step for ship design. But this analysis ignores the nonlinear coupling with other dynamic degrees of freedom which are significant near capsizes, for example, roll-pitch, and pitch-heave [54], [44]. On the other hand, a complete mathematical model for the motion of a ship includes the six degrees of freedom (associated with a rigid body and as shown in Fig. 4.1(a)) coupled with the fluid dynamics of the sea. This description of the capsizes problem gives rise to an infinite dimensional model (or high dimensional reduced order model) which challenges the identification of critical behavior leading to capsizes. Hence, a middle ground of using multi-degree of freedom model that is simple and low dimensional for geometric analysis, but still captures the nonlinear behavior near capsizes, will lead to reliable criteria.

Roll-pitch nonlinear coupling. It was observed as early as 1863, by William Froude, that a ship's roll response shows undesirable behavior due to autoparametric resonance when the

pitch natural (free oscillation) frequency is twice that of roll natural frequency. To explain this observation, Ref. [55] first proposed that pitch motion can be modeled as a simple harmonic oscillator which then substituted in the roll equation results in a Mathieu-type equation. Thus, this model assumed that pitch affects roll dynamics just as an amplitude-frequency dependent parameter causes resonance in the Mathieu equation. Although this explained the observed parametric response, it also showed exponential instabilities that resulted from not considering the effect of roll on pitch dynamics. However, a more successful attempt at modeling the pitch and roll coupling which is crucial for capsize was proposed in Refs. [56, 57], and explored further in Ref. [58]. In this model, the coupling is introduced using a bilinear term in the equation of motion for roll, and via a quadratic term in the equation of motion for pitch. Even with this simple form of nonlinearity, the authors in Refs. [56, 57, 58] present an explanation for the undesirable roll motion and various roll-pitch resonance phenomena. The couplings of multiple state variables can significantly alter predictions of safety versus capsize, as emphasized in Refs. [59, 60]. Considering the success of the coupled roll-pitch model in predicting observed behavior, we adopt this model for analyzing the large amplitude motions in terms of the geometric view of the phase space for understanding ship capsize in rough seas. Thus, we attempt to introduce conceptual aids for multi-degree of freedom systems which help in systematic interpretation of dynamics that lead to capsize.

Geometric view and escaping dynamics. The main goal in studying capsize of a ship is to obtain initial conditions that lead to undesirable roll motion in the presence of waves. This can be done by performing capsize runs in laboratory experiments of dynamically similar test models [61] along with the prediction of response from the mathematical model. This is where taking a geometric view of the phase space for identifying capsize becomes insightful. First, this approach provides a *skeleton* on which the forced dynamics is built, and provides a classification of orbits that lead to imminent capsize. Secondly, one can use this understanding to provide control strategies in presence of wave forcing. This is done by

uncovering the potential energy underlying the coupled roll-pitch motion and then using it in the context of escaping dynamics which treats the motion as either bounded or unbounded. Furthermore, the theory of invariant manifolds reveals the pathways in phase space that form the skeleton, even in the presence of random forcing. Thus, the present study aims to adopt the nonlinear coupling of roll-pitch motion as an application of escaping dynamics and invariant manifolds, laying the foundation for a new approach to the avoidance of capsizing. More general applications to avoidance of escape in multi-degree of freedom systems can be made.

4.2 Description of coupled roll-pitch model

We consider the dynamics of the nonlinear coupling of the roll and pitch degrees of freedom of a ship that results in a 4-dimensional phase space of roll, pitch, roll velocity and pitch velocity. The two degree of freedom coupled roll-pitch system has received some attention using perturbation analysis [56, 57, 58, 62, 63]. However, we adopt a global geometric approach of the motion analysis, using techniques which have been successful in celestial mechanics and physical chemistry [11, 64, 65]. We start by describing the system in terms of Lagrange's equations of motion and then re-scaling the system appropriately to recast it into a form with the fewest parameters.

4.2.1 Equations of motion: Lagrangian approach

Based on Refs. [56, 57, 58], we consider the coupled roll and pitch equations of the form

$$\begin{aligned} I_{xx}\ddot{\phi} &= -K_{\phi}\phi - K_{\phi\theta}\phi\theta + \tau_{\phi}(t) \\ I_{yy}\ddot{\theta} &= -K_{\theta}\theta - \frac{1}{2}K_{\phi\theta}\phi^2 + \tau_{\theta}(t) \end{aligned}$$

where, ϕ and θ are roll and pitch angles (in radians), I_{xx} and I_{yy} are the sums of the second moments of inertia and hydrostatic inertia, K_ϕ and K_θ are the linear rotational stiffness related to square of the corresponding natural frequency, $K_{\phi\theta}$ is the nonlinear coupling coefficient. Further, $\tau_\phi(t)$ and $\tau_\theta(t)$ are generalized time-dependent torques in the roll and pitch directions, respectively, which do not necessarily arise from an effective potential energy (for example, damping and wind/wave forcing). These equations are equivalent to Lagrange's equations with the Lagrangian given by

$$\begin{aligned}\mathcal{L}(\phi, \theta, \dot{\phi}, \dot{\theta}) &= \mathcal{T}(\dot{\phi}, \dot{\theta}) - \mathcal{V}(\phi, \theta) \\ &= \left(\frac{1}{2} I_{xx} \dot{\phi}^2 + \frac{1}{2} I_{yy} \dot{\theta}^2 \right) - \left(\frac{1}{2} K_\phi \phi^2 + \frac{1}{2} K_\theta \theta^2 + \frac{1}{2} K_{\phi\theta} \phi^2 \theta \right)\end{aligned}$$

and the kinetic and potential energy denoted by $\mathcal{T}(\dot{\phi}, \dot{\theta})$, and $\mathcal{V}(\phi, \theta)$, respectively, and generalized non-conservative forces $\tau_\phi(t)$ and $\tau_\theta(t)$. The resulting Lagrange's equations of

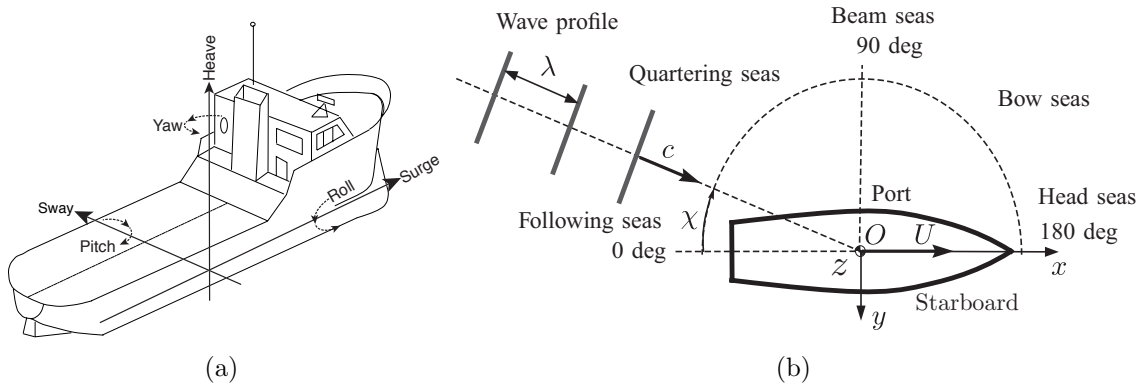


Figure 4.2.1: Schematic adapted from [66] illustrating the wave characteristics relative to ship motion using (x, y, z) as the body-fixed reference frame.

motion can be recast into a form

$$\begin{aligned}\ddot{\phi} &= -\omega_\phi^2 \phi + 2K_1 \phi \theta + m_\phi(t) \\ \ddot{\theta} &= -\omega_\theta^2 \theta + K_1 \frac{I_{xx}}{I_{yy}} \phi^2 + m_\theta(t)\end{aligned}\tag{4.2.1}$$

where the coefficients are

$$\omega_\phi = \sqrt{\frac{K_\phi}{I_{xx}}}, \quad \omega_\theta = \sqrt{\frac{M_\theta}{I_{yy}}}, \quad K_1 = -\frac{K_{\phi\theta}}{2I_{xx}}, \quad m_\phi(t) = \frac{\tau_\phi(t)}{I_{xx}}, \quad m_\theta(t) = \frac{\tau_\theta(t)}{I_{yy}}$$

Rescaled equations of motion. The conservative dynamics, when $m_\phi(t) = m_\theta(t) = 0$, of the system (4.2.1) is dependent on four parameters: the natural roll frequency (ω_ϕ), the natural pitch frequency (ω_θ), the nonlinear coupling constant (K_1), and the ratio of second moments of inertia (I_{xx}/I_{yy}). The conservative system has saddle equilibrium points at $(\pm\phi_e, \theta_e)$, where

$$\phi_e = \frac{\omega_\phi \omega_\theta}{K_1 \sqrt{2}} \sqrt{\frac{I_{yy}}{I_{xx}}}, \quad \theta_e = \frac{\omega_\phi^2}{2K_1}$$

and ϕ_e is also called the roll angle of vanishing stability and θ_e is the corresponding pitch angle. The coordinates of saddle equilibrium points (roll and pitch angles of vanishing stability) can now be used to rescale the original (ϕ, θ) coordinates to a nondimensional set (x, y) . Furthermore, the natural roll frequency can be used as the time scale to obtain nondimensional time, \bar{t} . We define

$$x = \frac{\phi}{\phi_e}, \quad y = \frac{\theta}{2\theta_e}, \quad \bar{t} = \omega_\phi t \tag{4.2.2}$$

and the equations of motion (4.2.1) become

$$\begin{aligned} \ddot{x} &= -x + 2xy + f_x(\bar{t}) \\ \ddot{y} &= -R^2 y + \frac{1}{2} R^2 x^2 + f_y(\bar{t}) \end{aligned} \tag{4.2.3}$$

where $(\dot{\cdot})$ denotes the time derivative with respect to the nondimensional time, \bar{t} and $R = \omega_\theta/\omega_\phi$ denotes the ratio of pitch to roll natural frequencies as the only system parameter for the conservative dynamics. From now on, we will drop the bar on \bar{t} and rescaled time will

be understood. These are Lagrange's equations of motion with rescaled Lagrangian

$$L(x, y, \dot{x}, \dot{y}) = \frac{1}{2}\dot{x}^2 + \frac{1}{2}\left(\frac{2}{R^2}\right)\dot{y}^2 - \left(\frac{1}{2}x^2 + y^2 - x^2y\right) \quad (4.2.4)$$

where the rescaled potential energy is given by

$$V(x, y) = \frac{1}{2}x^2 + y^2 - x^2y \quad (4.2.5)$$

which is independent of the only system parameter, R , and is shown graphically in Fig. 4.2(a).

The rescaling of the coordinates and time has made the nonlinear coupling term of the po-

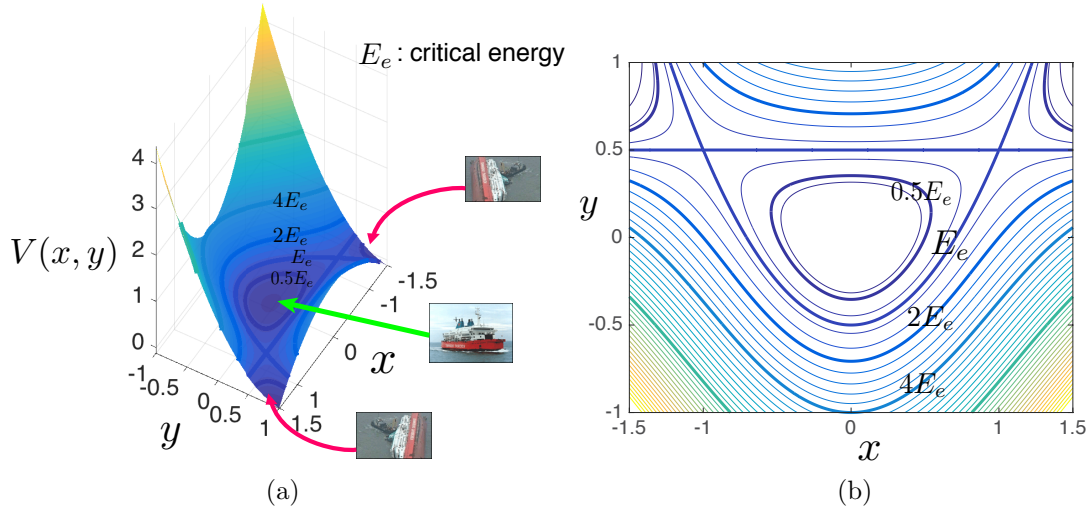


Figure 4.2.2: (a) Shows the effective potential energy with an upright ship in the region that corresponds to bounded motion inside the well and a capsized ship in the region that corresponds to unbounded motion. The total energy of the system can be considered as fixing a height of this potential well and shown here as contour lines of $0.5E_e$, E_e , $2E_e$, $4E_e$. (b) Shows the total energy as contour lines on the configuration space (x, y) for different values above and below the critical energy E_e .

tential into unity and the original coordinates can always be recovered using the transformation (4.2.2). We note that equations 4.2.3 are identical to those derived by Ref. [14], where they were called *symmetric internal resonance* equations. The potential energy (4.2.5) is also similar to the Barbaris potential studied by the chemistry community [67, 68, 69].

Conservative form. The equation of motion in the absence of damping and forcing ($f_x(t) =$

$f_y(t) = 0$) can be expressed in first order form as

$$\begin{aligned}
\dot{x} &= v_x \\
\dot{y} &= v_y \\
\dot{v}_x &= -x + 2xy \\
\dot{v}_y &= -R^2y + \frac{1}{2}R^2x^2
\end{aligned} \tag{4.2.6}$$

which conserves the total energy

$$E(x, y, v_x, v_y) = \frac{1}{2}v_x^2 + \frac{1}{R^2}v_y^2 + \frac{1}{2}x^2 + y^2 - x^2y \tag{4.2.7}$$

Non-conservative form. Any non-potential and time-varying generalized forces ($f_x(t)$, $f_y(t)$) on the right hand side of (4.2.8)

$$\begin{aligned}
\dot{x} &= v_x \\
\dot{y} &= v_y \\
\dot{v}_x &= -x + 2xy + f_x(t) \\
\dot{v}_y &= -R^2y + \frac{1}{2}R^2x^2 + f_y(t)
\end{aligned} \tag{4.2.8}$$

can be written in terms of the original angular accelerations ($m_\phi(t)$, $m_\theta(t)$), that is,

$$f_x(t) = \frac{K_1 \sqrt{2}}{\omega_\phi^4 R} \sqrt{\frac{I_{xx}}{I_{yy}}} m_\phi(t), \quad f_y(t) = \frac{K_1}{\omega_\phi^4} m_\theta(t) \tag{4.2.9}$$

When $f_x(t)$ and $f_y(t)$ are non-zero, the total energy changes with time according to

$$\dot{E} = v_x f_x(t) + \frac{2}{R^2} v_y f_y(t) = \langle \mathbf{v}, \mathbf{f} \rangle \tag{4.2.10}$$

where $\langle \cdot \rangle$ denotes the dot product of the velocity vector, $\mathbf{v} = (v_x, v_y)$, and the augmented

force vector, $\mathbf{f} = (f_x, (2/R^2)f_y)$. This energy evolution equation acts as the constraint on how quickly the dynamics can qualitatively change and go from below the critical energy (energy of the saddle points) to above when capsize is possible. In particular, if we consider including any damping forces linear in \mathbf{v} of the form

$$f_i = -k(x, y, v_x, v_y)v_i \quad \text{where, } k(x, y, v_x, v_y) \geq 0 \quad (4.2.11)$$

then such forces can only lead to a decrease in energy while a generalized time-dependent forcing, in particular an arbitrary signal $f_i(t)$, such as encountered during random waves, can lead to increase or decrease in energy. We should note here that in the non-conservative form, energy can still be kept constant if the velocity vector (v_x, v_y) is orthogonal to $(f_x, (2/R^2)f_y)$.

4.2.2 Energy surface

Let $\mathcal{M}(e)$ be the energy surface given by setting the integral (4.2.7) equal to a constant, i.e.,

$$\mathcal{M}(e) = \{(x, y, v_x, v_y) | E(x, y, v_x, v_y) = e\} \quad (4.2.12)$$

where e denotes the constant value of energy. For a fixed energy e , one can consider the surface $\mathcal{M}(e)$ as a three-dimensional surface embedded in the four-dimensional phase space, \mathbb{R}^4 and thus, co-dimension 1. Furthermore, if we take a cross-section of this three-dimensional surface, we obtain a two-dimensional Poincaré surface-of-section (SOS). The SOS can be used to define a two-dimensional return map ($\mathbb{R}^2 \rightarrow \mathbb{R}^2$) for a constant energy, e . This is shown for successively increasing energy in Fig. 4.2.3, and $R = 1.6$, for the SOS defined as

$$U_1 = \{(y, v_y) | x = 0, v_x(y, v_y; e) > 0\}, \quad \text{motion to the right} \quad (4.2.13)$$

$$U_2 = \{(y, v_y) | x = 0, v_x(y, v_y; e) < 0\}, \quad \text{motion to the left} \quad (4.2.14)$$

where, $v_x > 0$ is used to enforce a directional crossing of the surface. The energy of the equilibrium points is called the critical energy (or escaping energy) which is given by $E_e = 0.25$. As the trajectories approach this energy from below, capsize becomes inevitable and this can be interpreted in terms of the potential energy well. Since the potential energy (4.2.5) is independent of any system parameter, the discussion based on this potential well will be more general.

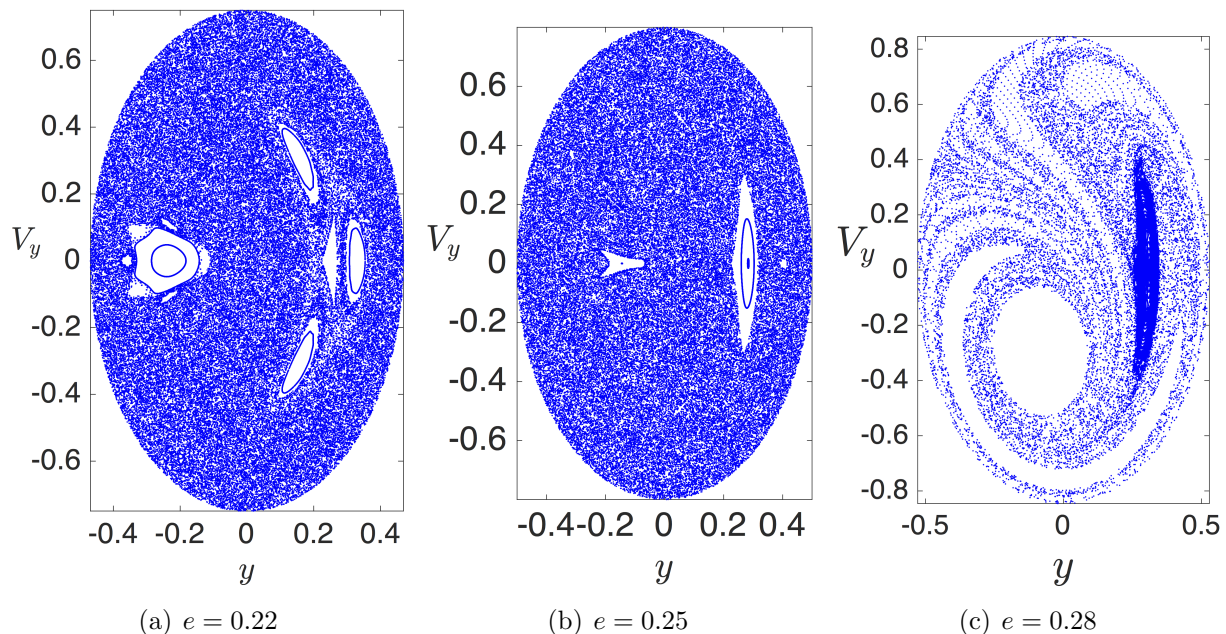


Figure 4.2.3: Poincaré surface-of-section (SOS) of the energy surface, showing orbits of the return map for different energy values. In the absence of damping and wave forcing, the system conserves energy and for energy below the critical value, E_e , all the trajectories intersect the SOS (4.2.13) as shown in (a) and (b) for $e = 0.22$ and $e = 0.25$. When the energy is above the critical value, trajectories leading to capsize do not intersect the surface (4.2.13) any longer and hence less return orbits are shown in (c)

Potential well and critical energy

We recall that the total energy (4.2.7) of the conservative system can be fixed at a constant value, i.e., $E(x, y, v_x, v_y) = e$, and this is equivalent to fixing a height in the plot of the effective potential, $V(x, y)$. Considering the configuration space, (x, y) , projection of effective potential in Fig. 4.2(b), we note that there are two equilibrium points (they are rank-1

saddles, as we will show later) in the (x, y) plane at $(\pm 1, 1/2)$ which are symmetrically located about the y -axis. Furthermore, the total energy of the system can be shown as a height on the potential surface and for a conservative system all possible states can only explore the surface below this value. For example, we show the contour lines of $0.5E_e, E_e, 2E_e, 4E_e$ in Fig. 4.2(a) and 4.2(b). Thus, the critical energy divides the motion into two energy cases which can simplify the understanding even when forcing is added.

1. **Case 1**, $E(x, y, v_x, v_y) < E_e$: If the energy is below E_e , the ship is safe against capsize as the state can not move from the region of bounded motion (surrounding the origin) to the region of unbounded motion i.e., capsize (beyond the saddles). See Fig. 4.4(a)
2. **Case 2**, $E(x, y, v_x, v_y) > E_e$: If the energy is just above E_e , two “bottlenecks” between the region of unbounded motion and bounded motion open up around the saddle points, permitting trajectories to move between the two realms. We will show in the next section that the transport through the bottlenecks connecting the two adjacent regions is controlled by invariant manifolds associated with the saddle points. See Fig. 4.4(c)

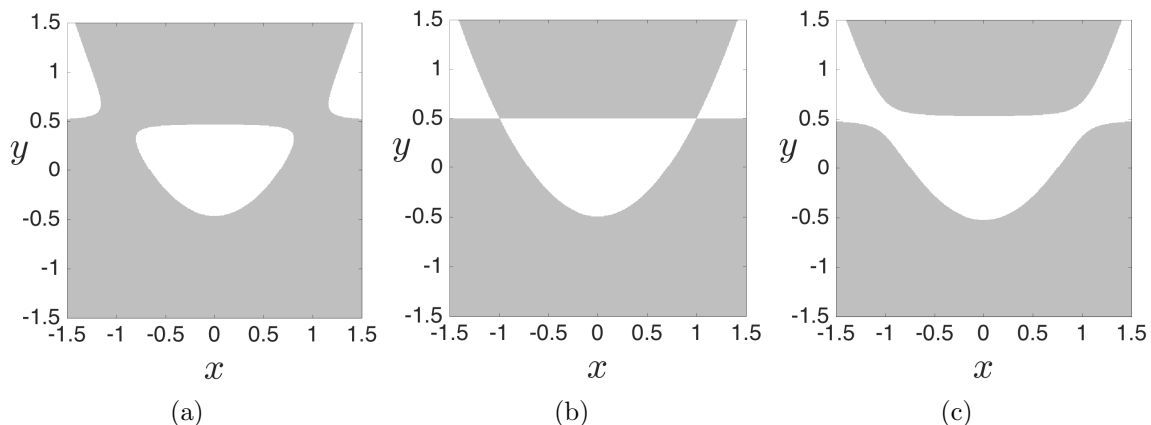


Figure 4.2.4: (a), (b), and (c) show the Hill’s region for $e < E_e$, $e = E_e$, and $e > E_e$ where E_e denotes the critical energy. The white region is the energetically accessible region bounded by the zero velocity curve and while the gray region is the energetically forbidden realm where kinetic energy is negative and motion is impossible.

Hill's region and zero velocity curve

The projection of energy surface into configuration space, (x, y) plane, is the region of energetically possible rolling and pitching motion of a ship of energy e . Let $M(e)$ denote this projection defined as

$$M(e) = \{(x, y) | V(x, y) \leq e\} \quad (4.2.15)$$

where $V(x, y)$ is the potential energy as in (4.2.5). The projection (4.2.15) of energy surface is known historically in mechanics as the *Hill's region*. The boundary of $M(e)$ is known as the *zero velocity curve*, and plays an important role in placing bounds on the ship's motion for a given energy. The zero velocity curves are the locus of points in the (x, y) plane where the kinetic energy, and hence the angular velocity vector vanishes, that is

$$E(x, y, v_x, v_y) = e = \frac{1}{2} \left(v_x^2 + \frac{2}{R^2} v_y^2 \right) + V(x, y) \quad (4.2.16)$$

$$v_x^2 + \frac{2}{R^2} v_y^2 = 2(e - V(x, y)) = 0 \quad (4.2.17)$$

From (4.2.15), it is clear that the ship's state is only able to move on the side of this curve for which the kinetic energy is positive. The other side of the curve, where the kinetic energy is negative and motion is impossible, will be referred to as the *energetically forbidden realm*.

4.2.3 Symmetries of the conservative equations of motion

We note the symmetries in the conservative system (4.2.6), when $f_x = 0$ and $f_y = 0$, by substituting $(-x, -v_x)$ for (x, v_x) which implies reflection about the y -axis and expressed as

$$s_x : (x, y, v_x, v_y, t) \rightarrow (-x, y, -v_x, v_y, t) \quad (4.2.18)$$

Thus, if $(x(t), y(t), v_x(t), v_y(t))$ is a solution to (4.2.6), then $(-x(t), y(t), -v_x(t), v_y(t))$ is another solution. The conservative system also has time-reversal symmetry

$$s_t : (x, y, v_x, v_y, t) \rightarrow (x, y, -v_x, -v_y, -t) \quad (4.2.19)$$

So, if $(x(t), y(t), v_x(t), v_y(t))$ is a solution to (4.2.6), then $(x(-t), y(-t), -v_x(-t), -v_y(-t))$ is another solution. These symmetries can be used to decrease the number of computations, and to find special solutions. For example, any solution of the conservative system will move so as to keep the energy E given by (4.2.7) constant. For fixed energy, there will be zero velocity curves corresponding to $V(x, y) = e$, the contours shown in Fig. 4.2(b). Any trajectory which touches the zero velocity curve at time t_0 must retrace its path in configuration space (i.e., $q = (x, y)$ space),

$$q(-t + t_0) = q(t + t_0) \quad \dot{q}(-t + t_0) = -\dot{q}(t + t_0) \quad (4.2.20)$$

We note that $y = v_y = 0$ is not an invariant manifold of the system, due to the nonzero coupling term (i.e., $K_1 = 0$), so no pure motion in roll (ϕ) is possible. However, $x = v_x = 0$ is an invariant manifold, so pure motion in pitch (θ) is possible.

4.3 Invariant manifolds and ship capsizing

4.3.1 Conservative dynamics

Tubes and transport. The global geometric view of capsizing of a ship is to say the trajectories will escape the potential well for energy states above the critical energy. This has been known as *escaping dynamics* and can be systematically understood using invariant manifolds which act as pathways for switching between capsizing and non-capsizing regions of the phase space. When the phase space is \mathbb{R}^4 , as in the dynamical system considered here,

the invariant manifolds are co-dimension 1 in the phase space and topologically equivalent to $\mathbb{S}^1 \times \mathbb{R}^1$. Due to this cylindrical geometry, they are referred to as *cylindrical manifolds or tubes* [70] and the geometric framework they imply as *tube dynamics*. The physical property of the tube manifold is that all motion that crosses a saddle equilibrium point must occur through the interior of the corresponding tube manifold. Thus, the global transport of states between the capsize and non-capsizes realms in the phase space is mediated by the tubes.

Numerical approach. The invariant manifolds are global objects in the sense that they exist in the entire phase space and can be numerically computed for infinite time. However, the invariant manifolds are associated with the unstable periodic orbits in the equilibrium regions around each saddle. This poses two challenges for the computation: saddle directions cause periodic orbit to be unstable, and exponential separation of trajectories on the manifolds. Hence, we need approaches that use the linearized behavior near the equilibrium points to generate the geometric structure of manifolds, and target periodic orbits of specified energy. This is where the theory of invariant manifolds of a periodic orbit and numerical approach of globalization of manifolds can be useful.

We adopt the method for computing periodic orbits from [70]. The main idea of the computation is to obtain a guess for the initial condition on the periodic orbit by using the eigenvector in the center direction of the saddle equilibrium point. Then, using this initial guess a shooting type numerical procedure called *differential correction* is performed to correct the initial guess. This shooting and correcting process is done iteratively with a specified tolerance ($\approx 10^{-8}$) until the initial condition for a periodic orbit of small amplitude ($\approx 10^{-4}$) is obtained. Then we begin the targeting step which aims for a specified energy of the periodic orbit using *numerical continuation* and successively increases the amplitude of the periodic orbit until the tolerance for energy of the orbit is satisfied.

Algorithm for computing tube manifolds leading to imminent capsizing

In this section, we go through the steps of computing tube manifolds that lead to imminent capsizing.

Step 1: Select an appropriate energy. We begin by deciding and selecting the total energy of the ship at an initial instant and in absence of forcing, this total energy (4.2.7) is conserved. Depending on whether the instantaneous energy is above or below the critical value, E_e , the bottleneck around the equilibrium points either exist or do not exist. For the purpose of our computations, we use values of $E = 0.253, 0.28$ or $\Delta E = 0.003, 0.03$, respectively, where $\Delta E = E - E_e$, which correspond to energy at which bottlenecks exist and tubes lead to imminent capsizing. Furthermore, we will see in the following discussion that the magnitude of ΔE is related to the width of the bottleneck and hence is very relevant to the number of trajectories that lead to capsizing.

Step 2: Compute the periodic orbit about the critical point of interest. Next, we analyze the linearized dynamics near the saddle equilibrium points which extends to the full nonlinear system due to the generalization of Lyapunov's theorem by [71]. On one hand this analysis simplifies the types of orbits that exist in the full phase space (see Appendix C.2 for details) and on the other hand, this is also a straightforward procedure to compute periodic orbits around the equilibrium points. We compute the non-trivial equilibrium points for the conservative form of the system at $(\pm 1, 0.5, 0, 0)$. In the present discussion, we will generally denote the left and right equilibrium points by $(x_e, y_e, 0, 0)$ and call them as C_1 and C_2 , respectively, for specific notation.

Obtain guess for initial condition. The stability of these equilibrium point can be obtained by linearizing the system about it and computing the eigenvalues. This computation is shown in Appendix C.2 and we obtain eigenvalues (C.2-3) of the form $\pm\lambda$ and $\pm i\nu$. The complex eigenvalue and its corresponding eigenvector can now be used to generate a guess for initial condition on the periodic orbit and its period T , which will be close to $2\pi/\nu$.

Next, considering the saddle equilibrium point, C_2 , we construct the initial condition using the general solution (C.2-8) of the linearized system (C.2-1). The initial conditions of a periodic orbit (p.o.) of x -amplitude $A_x > 0$ can be computed by letting $t = \alpha_1 = \alpha_2 = 0$ and $\beta = -A_x/2$. This is now transformed back into the original coordinates and yields an initial condition

$$\bar{x}_0 = \left(1, \frac{1}{2}, 0, 0\right) + 2Re(\beta w_1) \quad (4.3.1)$$

where $\beta = A_x/2$ is a small amplitude. Thus, using the formula (C.2-6) we obtain the initial guess as

$$\bar{x}_0 = \left(1 + A_x, \frac{1}{2} + \frac{A_x R^2}{R^2 - \nu^2}, 0, 0\right) \quad (4.3.2)$$

Differential correction and numerical continuation. Now, with the guess for initial condition in hand, we consider a shooting method for computing the periodic orbits around C_2 (and equivalently C_1). This approach begins with small “seed” periodic orbits obtained from the linearized equations of motion near C_2 , and uses differential correction and numerical continuation to generate the desired p.o. corresponding to the selected energy, e . The initial condition given in (4.3.2) will only yield a good approximation to a p.o. in the nonlinear equations (4.2.6) in the case $A_x \ll 1$ which corresponds to a much smaller energy than we selected in step 1. For the p.o. corresponding to the selected energy, e , the amplitude is larger than A_x and thus to obtain such an amplitude, we proceed as follows. Let $A_{x_1} < A_{x_2} \ll 1$ be two small amplitudes with corresponding guess initial conditions $\bar{x}_{0,g}^{(1)}$ and $\bar{x}_{0,g}^{(2)}$, respectively, where g denotes that this is an initial guess to a true periodic solution of (4.2.6).

We will use differential correction, described in Appendix C.4, to produce initial condition that converge to a periodic orbit of energy e in the nonlinear equations which are accurate to some specified tolerance d . The convergence criteria is based on the property of a periodic orbit that it returns to the starting point after a given period. The computation of periodic orbits and the corresponding period, for general time-dependent nonlinear systems, is a

numerical field in its own right but we can use the knowledge of the center subspace to initialize a shooting type procedure. Thus, if $\bar{x}_{po} \equiv \bar{x}_0$ is a true initial condition on a p.o., $x_{po}(t)$, of period T , the convergence criteria requires

$$\|\bar{x}_{po}(T) - \bar{x}_{po}(0)\| < d \quad (4.3.3)$$

for a specified tolerance, $d \approx 10^{-6}$. Differential correction uses the analytical expression of the first guess in an iterative process which shoots for the end point, checks the error and updates the initial condition while keeping some values constant. In our case, we want to keep the x -value constant and update the y -value of the guess initial condition for the periodic orbit. Thus, the correction term (see C.4 for derivation) is given by

$$\delta y_0 = \left(\Phi_{32} - \Phi_{42} \frac{\dot{v}_{x_1}}{\dot{v}_{y_1}} \right)^{-1} v_{x_1}$$

and hence to satisfy the tolerance on v_{x_1} , we let

$$y_0 \rightarrow y_0 - \delta y_0$$

This process of adding *small corrections*, hence the name **differential correction**, converges to $|v_{x_1}| < d$ within a few iterations, typically 10-20 for the tolerance, $d \approx 10^{-10}$. The above procedure yields an accurate initial condition for a periodic orbit from the starting guess. If our initial guess came from a linear approximation near the equilibrium point (C.2-8), it has been observed numerically that we can only use this procedure for small amplitude around the critical point, C_i , and this corresponds to energy much lower than the critical energy. But for computation of bottlenecks around these critical points, we want an orbit of arbitrarily large amplitude (which is in one-to-one correspondence with the energy e), we resort to **numerical continuation** to generate the family of periodic orbits which reaches the appropriate energy, e .

To this end, we proceed as follows. Suppose we find two small nearby periodic orbit initial conditions, $\bar{x}_0^{(1)}$ and $\bar{x}_0^{(2)}$, correct to within the tolerance d , using the differential correction procedure described above. We can generate a family of periodic orbits with successively increasing amplitudes around C_i in the following way. Let

$$\begin{aligned}\Delta &= \bar{x}_0^{(2)} - \bar{x}_0^{(1)} \\ &= [\Delta x_0, \Delta y_0, 0, 0]^T\end{aligned}$$

A linear extrapolation to an initial guess of slightly larger amplitude, $\bar{x}_0^{(3)}$ is given by

$$\begin{aligned}\bar{x}_{0,g}^{(3)} &= \bar{x}_0^{(2)} + \Delta \\ &= \left[(x_0^{(2)} + \Delta x_0), (y_0^{(2)} + \Delta y_0), 0, 0 \right]^T \\ &= \left[x_0^{(3)}, y_0^{(3)}, 0, 0 \right]^T\end{aligned}$$

Thus, keeping $x_0^{(3)}$ fixed, we can use differential correction on this initial condition to compute an accurate solution $\bar{x}_0^{(3)}$ from the initial guess $\bar{x}_{0,g}^{(3)}$ and repeat the process until we have a family of solutions. We can keep track of the energy of each periodic orbit and when we have two solutions, $\bar{x}_0^{(k)}$ and $\bar{x}_0^{(k+1)}$, whose energies bracket the appropriate energy, e , we can refine our continuation until we find a periodic orbit of energy e to within a specified tolerance. Thus, the result is a periodic orbit of desired energy e and of some period T with initial condition X_0 .

Step 3: Compute the tube manifolds of the periodic orbit. First, we find the local approximation to the unstable and stable manifolds of the periodic orbit from the eigenvectors of the monodromy matrix. Next, the local linear approximation of the unstable (or stable) manifold in the form of a state vector is integrated in the nonlinear equations of motion to produce the approximation of the unstable (or stable) manifolds. This procedure is known as **globalization of the manifolds** and we proceed as follows:

First, the state transition matrix $\Phi(t)$ along the periodic orbit with initial condition X_0 can be obtained numerically by integrating the variational equations along with the equations of motion from $t = 0$ to $t = T$. This is known as the monodromy matrix $M = \Phi(T)$ and the eigenvalues can be computed numerically. For Hamiltonian systems (see [72] for details), tells us that the four eigenvalues of M are of the form

$$\lambda_1 > 1, \quad \lambda_2 = \frac{1}{\lambda_1}, \quad \lambda_3 = \lambda_4 = 1$$

The eigenvector associated with eigenvalue λ_1 is in the unstable direction, the eigenvector associated with eigenvalue λ_2 is in the stable direction. Let $e^s(X_0)$ denote the normalized (to 1) stable eigenvector, and $e^u(X_0)$ denote the normalized unstable eigenvector. We can compute the manifold by initializing along these eigenvectors as:

$$X^s(X_0) = X_0 + \epsilon e^s(X_0)$$

for the stable manifold at X_0 along the periodic orbit, as illustrated in Fig. 4.3.1, and as

$$X^u(X_0) = X_0 + \epsilon e^u(X_0)$$

for the unstable manifold at X_0 . Here the small displacement from X_0 is denoted by ϵ and its magnitude should be small enough to be within the validity of the linear estimate, yet not so small that the time of flight becomes too large due to asymptotic nature of the stable and unstable manifolds. Ref. [73] suggests typical values of $\epsilon > 0$ corresponding to nondimensional position displacements of magnitude around 10^{-6} . By numerically integrating the unstable vector forwards in time, using both ϵ and $-\epsilon$, for the forward and backward branches respectively, we generate trajectories shadowing the two branches, W_+^u and W_-^u , of the unstable manifold of the periodic orbit. Similarly, by integrating the stable vector backwards in time, using both ϵ and $-\epsilon$, for forward and backward branch respectively,

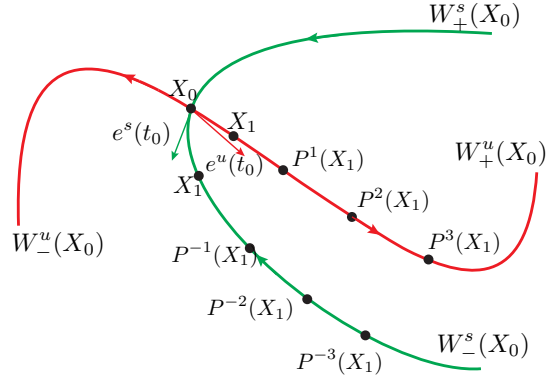


Figure 4.3.1: Schematic of the globalization of invariant manifolds that computes an approximation of the two branches of the unstable (W_{\pm}^u) and stable (W_{\pm}^s) manifolds of a periodic orbit. The two branches are computed using the positive and negative directions of the eigenvectors $e^u(t_0)$ and $e^s(t_0)$, respectively, after an initial displacement of small magnitude from X_0 to X_1 . Then, the unstable (stable) manifold is computed using successive forward (backward) iterate of the map P which marches along the half manifold.

we generate trajectories shadowing the stable manifold, $W_{+,-}^s$. This numerical procedure is shown schematically in Fig. 4.3.1. For the manifold at $X(t)$, one can simply use the state transition matrix to transport the eigenvectors from X_0 to $X(t)$:

$$X^s(X(t)) = \Phi(t, 0)X^s(X_0)$$

It is to be noted that since the state transition matrix does not preserve the norm, the resulting vector must be normalized.

The globalized invariant manifolds associated with rank-1 saddles are known as Conley-McGehee tubes [74] and give insight into capsizing criteria or control of capsizing when a generalized wave moment is acting on a ship. These *tubes* form the skeleton of escape dynamics by leading the states inside them to unbounded motion and the states outside to stay bounded in the potential well.

Step 4: Obtain the intersection of Poincaré surface-of-section and the globalized manifolds. We adopt the Poincaré surface-of-sections U_1 and U_2 defined as two-dimensional

surfaces in (4.2.13) and (4.2.14), respectively. In this form, $v_x(y, v_y; e)$ means v_x is constrained by the energy (4.2.7) for a trajectory that intersects the surface U_1 with positive v_x (or U_2 with negative v_x). Thus, the Poincaré section acts as a surface on which trajectories leading to capsize can be studied, and this is shown in Fig. 4.3.2. The two surfaces differ only in the direction of motion of the trajectories passing through them.

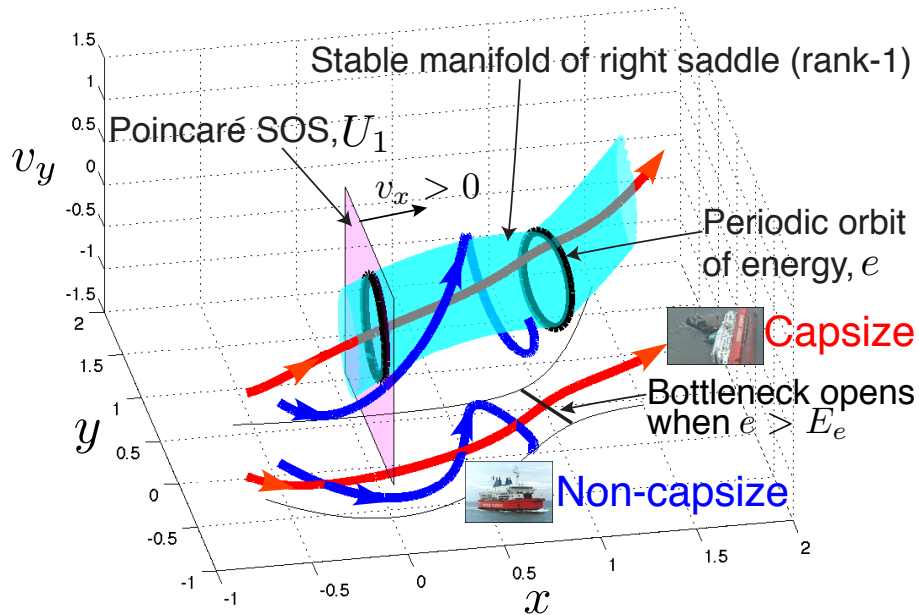


Figure 4.3.2: Shows the Poincaré surface-of-section, U_1 (4.2.13), as the magenta plane and the stable manifold of right saddle is shown as the cyan surface for a given energy e . The manifold is codimension-1 in the phase space of \mathbb{R}^4 with geometry $\mathbb{R}^1 \times \mathbb{S}^1$ that is cylindrical, and hence the name *tube manifold*. The stable manifold of a saddle up to its first intersection with U_1 is the pathway that leads to imminent capsize. The trajectory that leads to escape from the potential well and corresponds to the imminent capsize of a ship, for example the red trajectory, lies in the interior of the tube. Similarly, a trajectory that stays inside the potential well and corresponds to an upright ship lies outside the tube. These example trajectories are shown in the $x - y - v_y$ space for a given energy e and also as projection in the configuration space.

The surfaces U_i are strategically placed, allowing us to get cross-sections of the flow within the three-dimensional energy surface $\mathcal{M}(e)$. Referring to the Fig. 4.3(a), where we use $R = 1.6$ and $\Delta E = 0.03$, if we integrate backwards (in time) the stable manifold of the periodic orbit around the right critical point until it intersects U_1 , we obtain an elliptical region that is

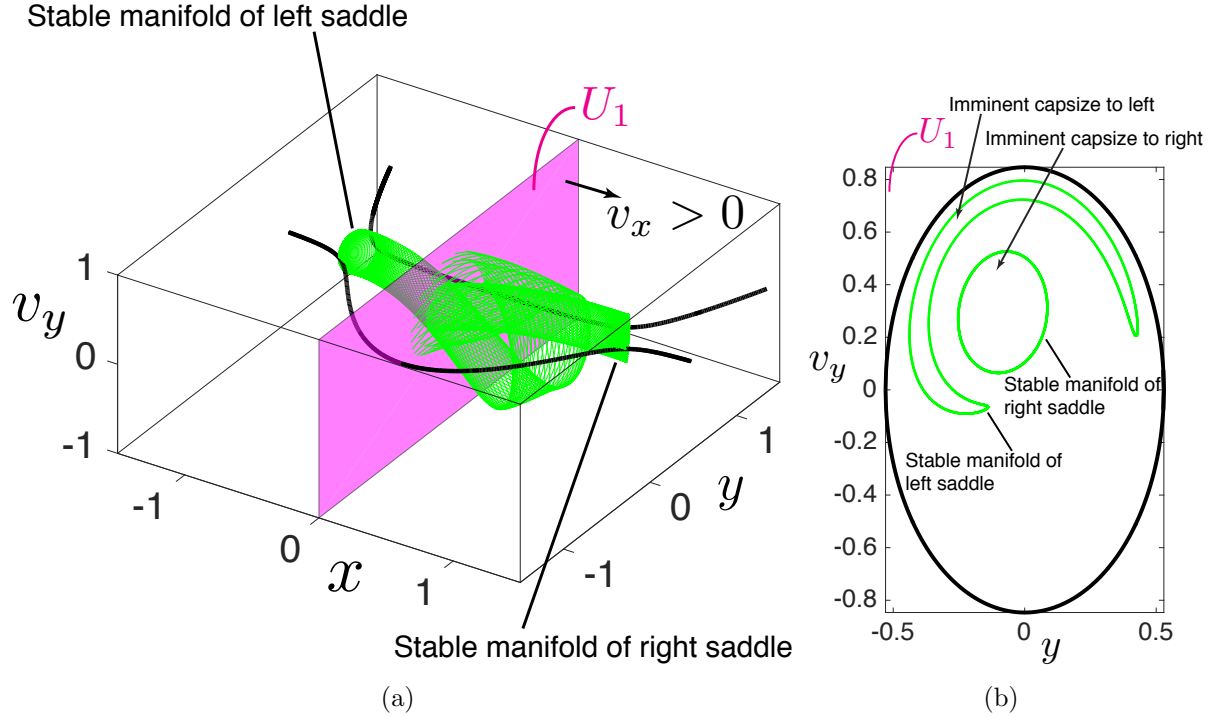


Figure 4.3.3: (a) Shows the tubes that lead to imminent capsize to left and right, and the SOS, U_1 (4.2.13), is shown as the magenta plane. These are the stable manifolds of the left and right saddles, and are cylindrical, that is $\mathbb{R}^1 \times \mathbb{S}^1$ geometry. (b) Shows the intersection of the stable manifolds with the SOS U_1 as regions with green boundary, and the black boundary corresponds to intersection of the energy surface (4.2.12) with the SOS U_1 . where the boundary of the region leading to imminent capsize is the intersection of the stable manifolds with the SOS.

topologically a circle, \mathbb{S}^1 , shown in y vs. v_y coordinates. Although the stable manifold does not stop here, being a global object, we know the initial conditions inside this ellipse will lead to imminent capsize through the bottleneck on the right side. Furthermore, if we pick an initial condition on U_1 , but which is outside of this ellipse, and integrate forward, it will not lead to capsize, and will instead 'bounce back' from the neck region, since it a non-transit orbit. It is to noted that for a smaller energy above critical, for example $\Delta E = 0.003$, the tube manifold has a smaller width and its intersection with Poincaré sections has a smaller width and hence its intersection with U_1 is a smaller elliptical region.

4.3.2 Non-conservative dynamics

Motion in rough sea. Ocean waves are typically modeled as realizations of a stationary and homogeneous Gaussian stochastic process with zero mean [66]. This stochastic process is represented by a standard formula for the power spectral density (PSD) of the sea surface elevation that describes the energy content of the ocean waves distributed over the frequency domain. We adopt the *Pierson-Moskowitz* wave spectrum given by

$$S(\omega) = 0.11H_s^2 \frac{\omega_z^4}{\omega^5} \exp\left(-0.44 \left(\frac{\omega_z}{\omega}\right)^4\right) \quad (4.3.4)$$

where $S(\omega)$ is the wave energy spectrum that denotes the PSD for a particular sea environment, H_s is the significant wave height (which is defined as the average of the heights of largest 1/3rd of the waves), $\omega_z = 0.527$ rad/s is the characteristic frequency, ω is the wave frequency. The wave frequency is typically sampled over discrete frequencies over the range $\omega_1 = d\omega$ to $\omega_N = 2$ rad/s using a step size of $d\omega = 0.02$ rad/s and $N = 100$. The wave energy spectrum for different significant wave heights is shown in Fig. 4.4(a) and justifies the range of frequency since almost all the energy is contained within $\omega_N = 2$ rad/s.

Using this discretization of the continuous spectrum along with uniformly distributed random phases ϵ_i on $[0, 2\pi]$, we generate a train of random waves that simulate the forcing due to the rough sea environment [66, 75]. This is typically expressed as time-dependent angular accelerations in (4.2.1) and then rescaled using (4.2.9) to obtain random forcing. The form of time-dependent angular accelerations considered here is also treated in Refs. [45, 43, 76] and is given by

$$m_\phi(t) = \omega_\phi^2 \sin \chi \alpha_0 \frac{\sqrt{2d\omega}}{g} \sum_{i=1}^N \omega_i^2 \sqrt{S(\omega_i)} \sin\left(\frac{\omega_{ie}}{\omega_\phi} t + \epsilon_i\right) \quad (4.3.5)$$

$$m_\theta(t) = \omega_\theta^2 \cos \chi \alpha_0 \frac{\sqrt{2d\omega}}{g} \sum_{i=1}^N \omega_i^2 \sqrt{S(\omega_i)} \sin\left(\frac{\omega_{ie}}{\omega_\phi} t + \epsilon_i\right) \quad (4.3.6)$$

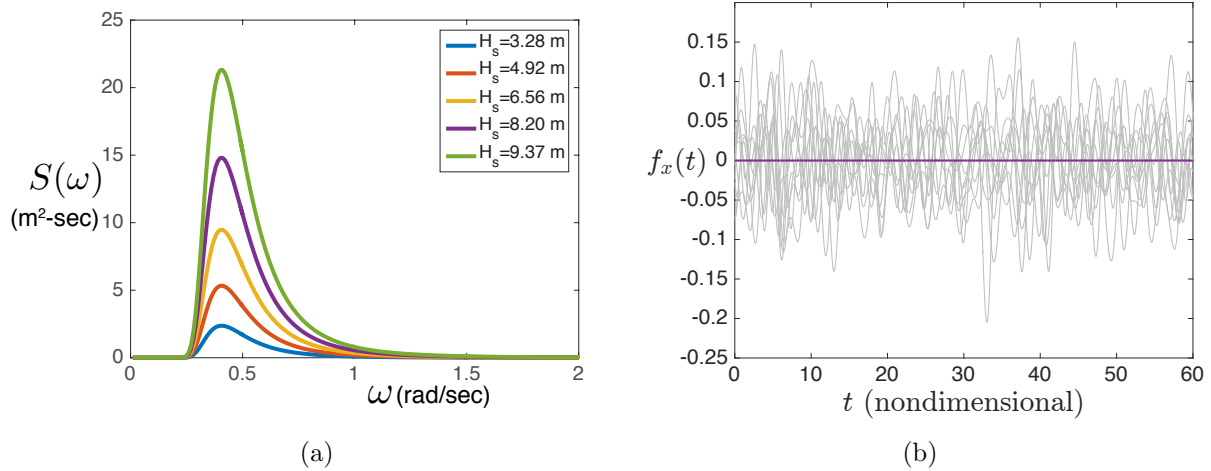


Figure 4.3.4: (a) Shows the wave energy spectrum, called the *Pierson-Moskowitz*, for different significant wave height. The peak energy is centered at the same frequency and the max energy increases with increasing significant wave height. This is used to sample the wave forcing for simulating a ship rolling and pitching in rough sea. (b) Shows 10 samples of forcing, $f_x(t)$ in beam sea of significant wave height, $H_s = 4.92$ m and the mean of 10^5 ensembles as the zero line which demonstrates the underlying stochastic process has zero mean.

where t is the non-dimensional time measured in the units of natural roll frequency (4.2.2), ω_ϕ and ω_θ are the natural roll and pitch frequencies for a ship, χ is the heading angle of the waves with respect to the ship, α_0 is the effective wave slope being 0.73, ω_e is the encounter frequency (frequency experienced in the ship's reference frame) given by

$$\omega_e = \omega - \frac{\omega^2 U}{g} \cos \chi \quad (4.3.7)$$

and U is the ship's speed. The heading angle and speed of the ship is illustrated in Fig. 4.1(b) along with different incident wave directions. We use the speed of the boat $U = 2.06$ m/s, and heading angle $\chi = 90^\circ$ (beam sea) in our simulations. In first order form, the equations of motion are given by (4.2.8) and the generalized time-dependent forcing is given by (4.2.9) and shown in Fig. 4.4(b).

In the phase space of $\xi = (x, y, v_x, v_y)$, that is \mathbb{R}^4 , we classified trajectories that lead to capsize in absence of forcing in terms of the geometry of solutions near the equilibria (see Appendix C.2 for details). We discovered the regions of the phase space that lead to capsize

through the bottleneck around critical points C_1 (right equilibrium point) or C_2 (left equilibrium point) as shown in Fig. 4.3.2. Now, we test the robustness of the tubes, a geometric structure in conservative dynamics, in presence of a random forcing. For simplifying the discussion, let us consider the case of imminent capsizing for the critical point C_1 , which in terms of tube dynamics means the first intersection of the stable manifold of C_1 with the SOS, U_1 (4.2.13).

In the conservative case, trajectories leading to imminent capsizing via C_1 reside completely inside the boundary of intersection of the stable manifold of C_1 with SOS, U_1 . Thus, in terms of capsizing probability this means all the trajectories inside tube intersection have probability = 1 and all trajectories outside the tube have probability = 0. Now, if we consider rough seas in the form of wave forcing (4.2.9), each initial condition on the SOS U_1 generates an ensemble of realizations of the random dynamical system (4.2.8). When we consider a large number of these realizations (say, 400), each initial condition can be assigned a probability of capsizing. This is simply the number of realizations that lead to capsizing divided by the total number of realizations. Thus, we obtain a distribution of capsizing probability for all starting conditions on the SOS, U_1 , and is shown in the contour plot of Fig. 4.3.5 for $H_s = 4.92$ m and $H_s = 9.84$ m, when $\Delta E = 0.003$. This corresponds to a low total energy above the critical/escaping energy while the random forcing can be considered as moderate and high in terms of significant wave heights [66]. Furthermore, when we consider a higher total energy above the critical/escaping energy, we observe tube dynamics to be more prominent as the boundary now covers the region with higher capsizing probability. The numerical demonstration shows that the tubes are robust to a general time-dependent forcing even though they are geometric structures derived from the conservative form. This is observed for both low and high total energy, as shown in Fig. 4.3.5 and Fig. 4.3.6, respectively, and also across moderate and high significant wave heights. Thus, the tube dynamics form the skeleton in predicting capsizing probability even when random forcing is introduced. Thus, it provides a geometric framework to study escaping dynamics in presence of a general time-

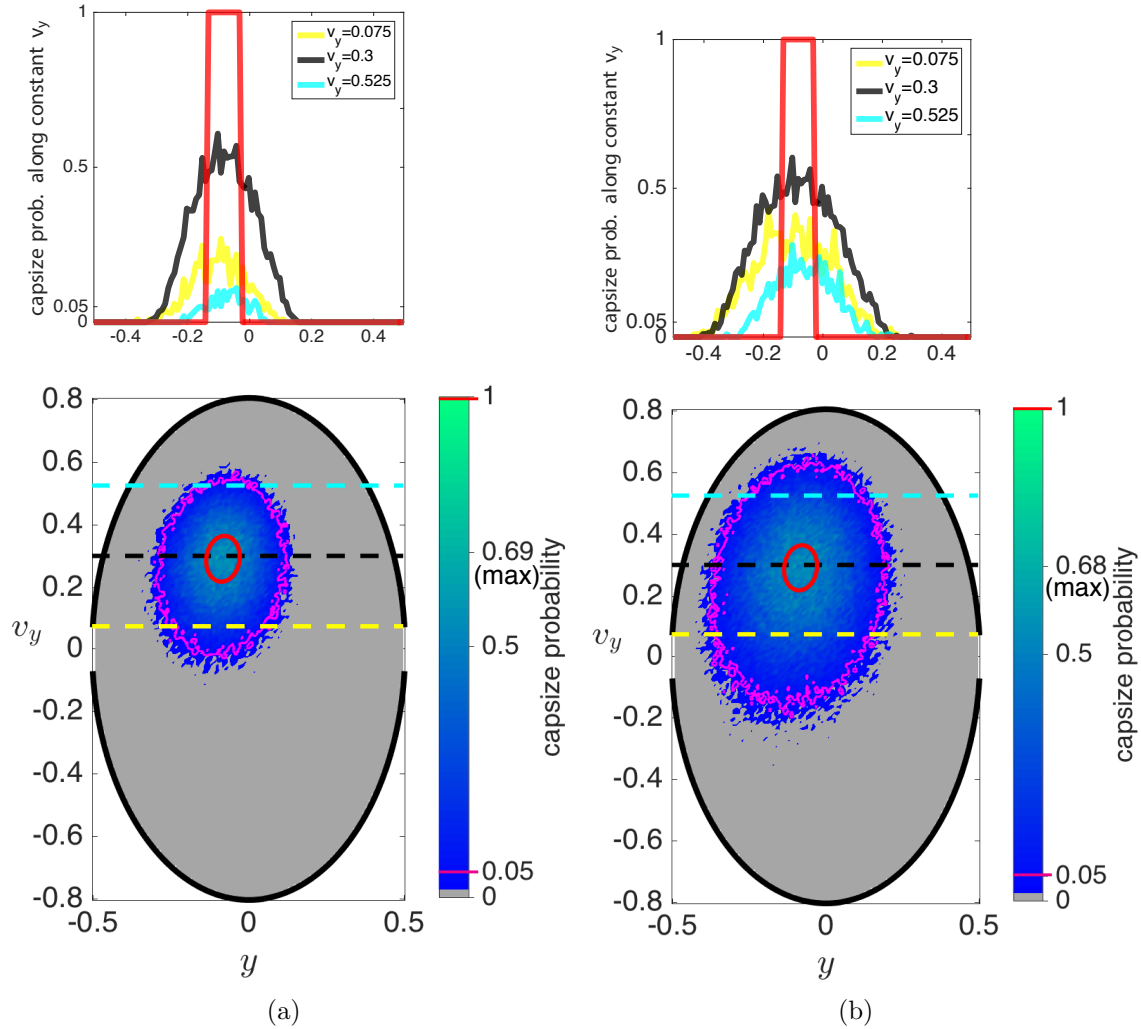


Figure 4.3.5: (a) Shows the distribution of capsizing probability as the contour plot with region that does not lead to capsizing, that is starting conditions with 0 probability of imminent capsizing, shown as grey region for $H_s = 4.92$ m and $\Delta E = 0.003$. (b) Shows the same for $H_s = 9.84$ m and $\Delta E = 0.003$. In both figures, the black boundary is the intersection of the energy ellipsoid (see Appendix C.5 for details) with the Poincaré SOS and the magenta curve is the boundary of the region that has capsizing probability greater than 0.05. In absence of random forcing, the boundary of the region with 1 probability is given by the tube intersection, shown as red curve. The dotted lines denote the cross-section of the distribution at a constant v_y , and shown at the top of the contour plot. The red bar of sharp unit probability corresponds to the tube intersection at its maximum width; while the spread out distribution correspond to the dotted lines with different v_y values.

dependent forcing.

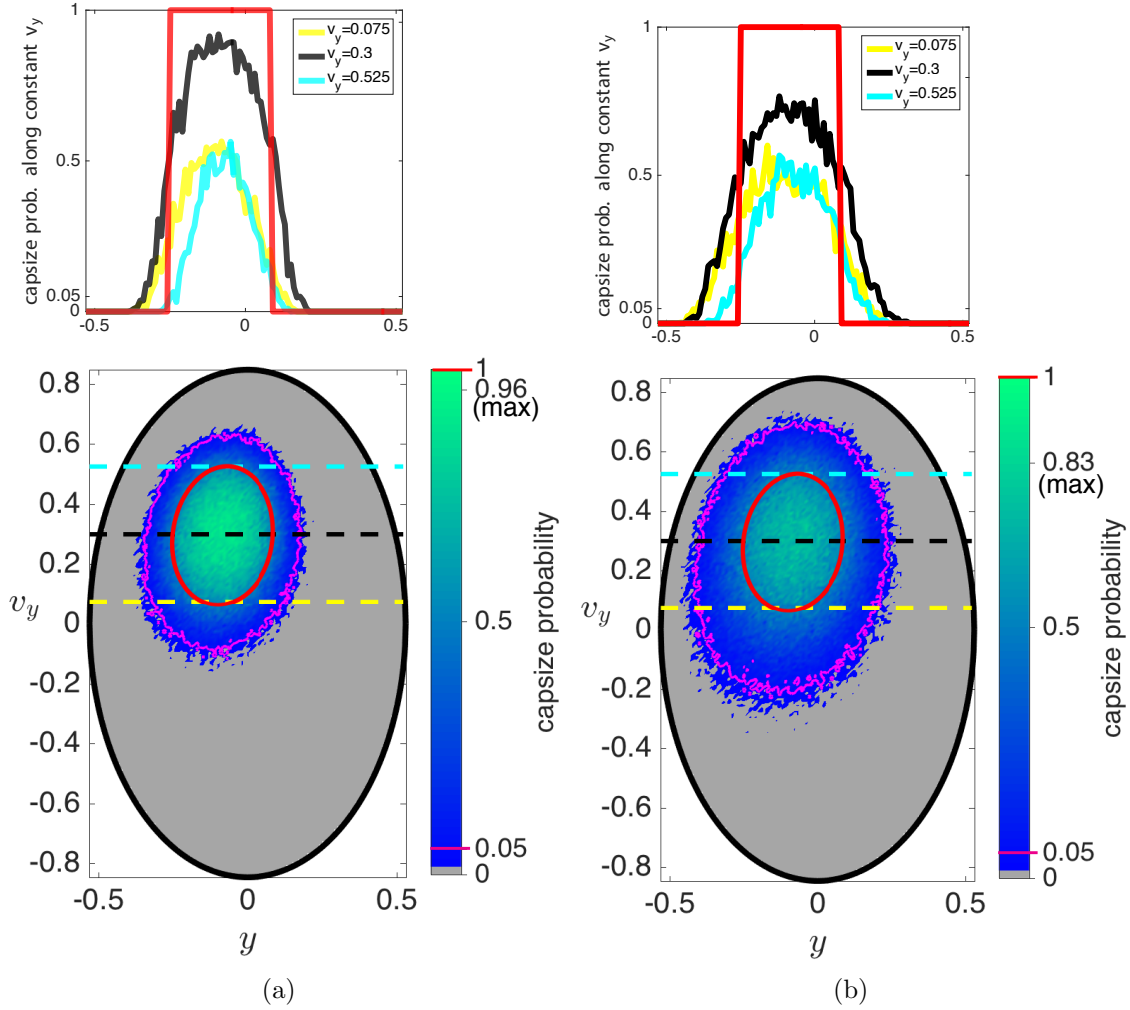


Figure 4.3.6: (a) Shows the distribution of capsizing probability as the contour plot with region that does not lead to capsizing, that is starting conditions with 0 probability of imminent capsizing, shown as grey region for $H_s = 4.92$ m and $\Delta E = 0.03$. (b) Shows the same for $H_s = 9.84$ m and $\Delta E = 0.03$.

4.4 Partial control and ship capsizing

We observe from the computational study that on the surface-of-section U_1 there is a region, called *escaping zone*, that leads a trajectory to escape from the potential well and hence capsizing. In absence of wave forcing, the escaping zone has a distinct boundary given by the intersection of stable manifold of the critical points with U_1 , and in presence of rough seas, the escaping zone is enlarged and the boundary can now be defined using a threshold for capsizing probability. Thus, avoidance of capsizing can be achieved by controlling the trajectory

from entering the escaping zone on U_1 , and this surface-of-section can be considered as the space of *actuated state variables*. This is where the recently developed approach of *partial control* ([77, 78, 79]) can be adopted to avoid capsize in the presence of disturbance and more importantly using a smaller control.

The scenario for applying partial control is as follows: Let us consider a compact domain Ω in the phase space where a continuous map f can be defined such that

$$\mathbf{q}_{n+1} = f(\mathbf{q}_n) \tag{4.4.1}$$

where, $\mathbf{q}_n \in \mathbb{R}^k$ are the k -coordinates, and not all the phase space variables, and n denotes iteration of the map. In this domain, we have a closed and bounded region Q from which the trajectories eventually escape due to repulsion from a zero-measure set called chaotic saddle (transient chaos [80]), or exit via the stable manifolds of a periodic orbit (tube dynamics [70]). Our objective is to stay in the region Q by avoiding escape with infinite iteration of the map in presence of a disturbance $\boldsymbol{\xi}_n \in \mathbb{R}^k$ which is acting along with the escaping dynamics. Furthermore, we want to do this avoidance by applying a feedback control $\mathbf{u}_n \in \mathbb{R}^k$ such that the *partially controlled* trajectory stays in the region Q . Thus, we have

$$\mathbf{q}_{n+1} = f(\mathbf{q}_n) + \boldsymbol{\xi}_n + \mathbf{u}_n \tag{4.4.2}$$

and the following assumption:

- There is a bound $\xi_0 > 0$ such that $\|\boldsymbol{\xi}_n\| \leq \xi_0$, and we call $\boldsymbol{\xi}_n$ *admissible* disturbances.
- There is a bound $u_0 > 0$ such that $\|\mathbf{u}_n\| \leq u_0$, and we call \mathbf{u}_n *admissible* controls.
- And the upper bound on control is smaller than the upper bound on disturbances
 $u_0 < \xi_0$

It is to noted that the chosen feedback control \mathbf{u}_n is dependent on where a trajectory lands

in the domain after a disturbance ξ_n has acted. This choosing of the control is performed by computing a set, let us say $S \in Q$, called *safe set* by using the safe set sculpting algorithm proposed in [78].

The sculpting algorithm is based on the idea of a safe point defined as

$$\max_{\mathbf{q} \in S, \|\xi_n\| \leq \xi_0} \text{dist}(f(\mathbf{q}) + \xi_n, Q) = u_0 < \xi_0 \quad (4.4.3)$$

and shown schematically in Fig. 4.4. The algorithm begins with the region Q which has both

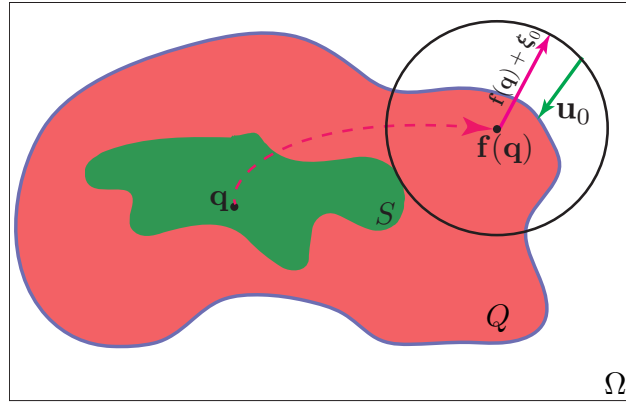


Figure 4.4.1: Schematic of a **safe** point \mathbf{q} in the final safe set, S . \mathbf{q} is mapped to $f(\mathbf{q})$ and the disturbance, ξ_0 takes it to the boundary of the disk which is at most u_0 distance .

safe and unsafe points in it. We proceed by cutting out points that are unsafe according to the above definition and obtain a new set $C_1 \subset Q$. If C_1 is a safe set in Q then all points in C_1 should be safe, otherwise the sculpting algorithm proceeds to the next iteration, and cuts out unsafe points to obtain a new set $C_2 \subset Q$. Thus, we have the iterative procedure which ends with a set C_n such that all point are safe according to Eqn. 4.4.3. We call C_n final safe set S . This iterative algorithm is called *safe-set sculpting* and computes a set of points S in the region Q which can be controlled using a control upper bound of u_0 in presence of a disturbance upper bound of ξ_0 where $u_0 < \xi_0$. The trajectory obtained by using the safe set is called *admissible*, and is given by (4.4.2). This can be summarized as algorithm shown as Procedure 3 of sculpting points, which are unsafe according to (4.4.3).

The iterative procedure converges to the safe set $S \subset Q$ for a given ξ_0 , u_0 , and Q .

Procedure 3 Safe set sculpting algorithm

Input: Set initial set, $C_1 = Q$, and $i = 1$, maximum iteration, i_{max} and number of bad points in Q , $N_{cut} \neq 0$

while $i \leq i_{max}$ **do**

Fatten the set, C_i by maximum control magnitude u_0 so, $C'_i = C_i + u_{max}$.

Shrink the set, C'_i by disturbance ξ_0 so, $C''_i = C'_i - \xi_{max}$.

Cut the unsafe subsets of the set, C_i . A subset is unsafe if there exists $q \in C_i$ such that $\mathbf{f}(q) \notin C''_i$.

Compute number of unsafe points removed in this iteration, N_{cut} and set $C_{i+1} = C_i$ and update, $i = i + 1$.

end while

4.4.1 Computational approach to finding safe sets

We need a suitable definition for a map, its image and *escaping zone* on the domain Ω to compute safe sets for a dynamical system. Although, the numerical procedure is stated in terms of sets in \mathbb{R}^n , our computational study is based on the implementation in \mathbb{R}^2 . In order to apply the sculpting operator in \mathbb{R}^2 , we define a Poincaré return map, f , on the SOS, U_1 as defined by (4.2.13), for the flow given by (4.2.6). We know from the geometric view that a SOS should be such that intersection of trajectories are near transverse, and trajectories cross the SOS at least once before escaping from the potential well to the realm of capsize via the right and left bottlenecks. Thus, we adopt the two surfaces U_1 and U_2 as defined in (4.2.13) and (4.2.14), respectively, and define the intersection with the energy surface (4.2.7) as the domain Ω . Now, we need to define a region Q in Ω that excludes a zone that lead to escape from the potential well; we call it the *escaping zone* and denote it by E_{zone} . In this section, we propose two approaches based on defining the region Q and the return map f for partial control of ship capsize.

Step 1: Construct the region Q and define the map f . We begin by selecting the total energy e , which is above the critical energy E_e , and is the necessary, but not sufficient,

condition for capsizing. The value of energy e also defines the boundary $\partial\Omega$, which is the intersection of the energy surface with the SOS. Thus, the boundary $\partial\Omega$ is given by

$$\partial\Omega := \frac{(v_y - 0)^2}{(R\sqrt{e})^2} + \frac{(y - 0)^2}{(\sqrt{e})^2} = 1 \quad (4.4.4)$$

The closed and bounded set Q is the region $\Omega - E_{zone}$, and denotes the set where we want to keep the admissible trajectory (4.4.2). The set Q is shown in Fig. 4.2(c) as the grey region inside the black boundary $\partial\Omega$ with the escaping zone $E_{zone} = f^{-1}(\Gamma_{O,R})$ as the white region inside $\partial\Omega$. It is to be noted that the necessary and sufficient condition for a trajectory, that leads to imminent capsizing, is its crossing of SOS inside the first intersection of the stable manifold of the right/left saddle points. However, for an open dynamical system, like the one at hand, the map of initial points inside the escaping zone will never return to the SOS. Hence, we define the escaping zone as the pre-image of the first intersection of the stable manifold with the SOS.

Thus, we construct the map f , which is required in the *cutting* step of the sculpting algorithm, as the return map in the following two ways:

$$\Sigma_{U_1U_1} : U_1 \rightarrow U_1 \quad (4.4.5)$$

which is to say trajectories return to the plane $y - v_y$ with $v_x > 0$, and

$$\Sigma_{U_1U_2} : U_1 \rightarrow U_2 \quad (4.4.6)$$

which denotes the return map from the SOS with $v_x > 0$ to SOS with $v_x < 0$. Next, we discretize the region Q using a grid of points which act as the initial condition for the return map and obtain the image of these points.

Step 2: Obtain a discrete representation of continuous wave forcing. One of the interesting questions that arises in application of partial control is how to connect the upper

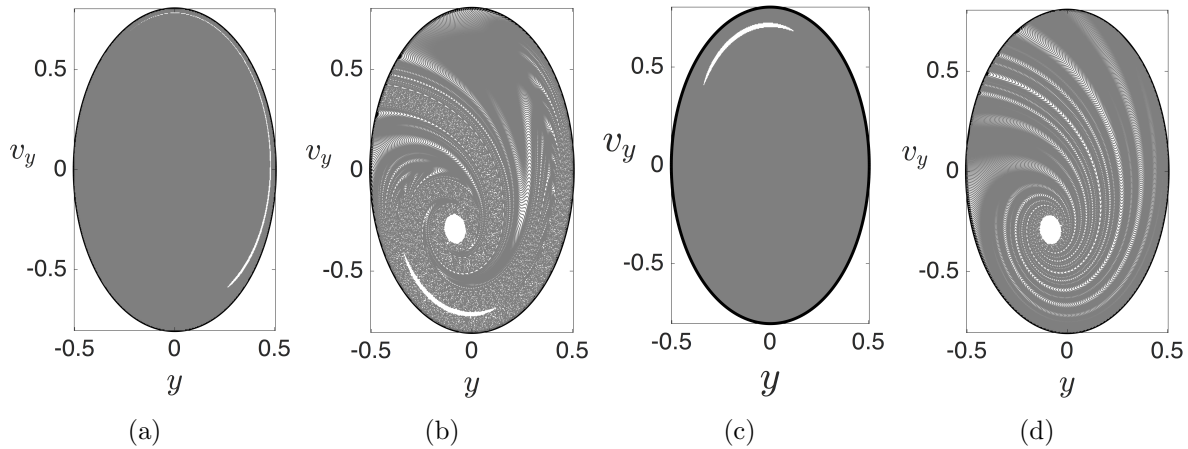


Figure 4.4.2: Shows the region Q and its image under the map f (4.4.5) in (a) and (b), respectively. The same is shown for the map f (4.4.6) in (c) and (d), respectively. These two approaches of defining the map f form the basis of obtaining safe sets in the partial control framework.

bound of disturbance with the environmental noise acting on the system. For a ship in rough sea, the random forcing due to waves can be treated as noise on the conservative motion. As we have shown in Sect. 4.3.2, the effect of rough seas can be very drastic, yet the geometric structure of the conservative system can still act as the skeleton for the exit basin. Furthermore, it has been discussed [81] that with increase in the intensity of noise, given by significant wave height H_s , the exit time increases until a critical value and then decays rapidly which is related to the preservation of KAM tori near low noise intensity. Thus, the noise affects the trajectory continuously but the accumulated effect on the return map can be captured by considering the noisy Poincaré map [81]. We call the effect of the continuous random forcing on the dynamics of the Poincaré map as the *discrete disturbance*.

To relate the significant wave height H_s with the upper bound on the disturbance ξ_0 , we adopt an ensemble average approach. We begin with a grid of sample initial points in our domain which is meant to capture different return times for the map f . Some of these initial points will land inside the stable manifold's intersection, and will never return to the surface, and hence are discarded. Next, we assign an ensemble of 100 (say) trajectories to each of the sample points and obtain the distribution of image points $f_{noise}(p)$ on the surface. Since

the mean of this distribution $\langle f_{noise}(p) \rangle$ has been found to coincide with the image $f(p)$ in absence of random forcing, we consider the difference as an accumulated effect of the noise and thus, a measure of the discrete disturbance ξ_0 .

Step 3: Safe set computations With the region Q and map f defined, and the obtained upper bound on the disturbance, we can use the *safe set sculpting* algorithm described as Procedure 3 to obtain safe sets. The sculpting algorithm works in an iterative process

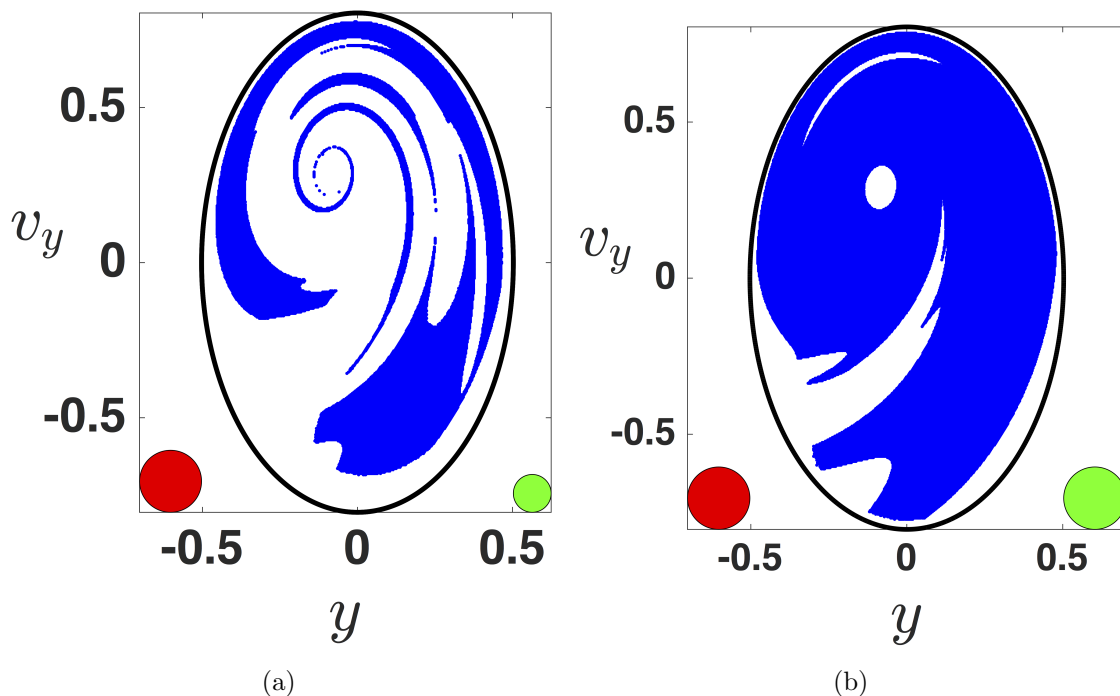


Figure 4.4.3: Using the safe set sculpting algorithm, we compute sets in the region Q (shown in (c)) and the map f (4.4.6) for the disturbance upper bound of $\xi_0 = 0.1$ and control upper bounds of $u_0 = 0.061$ (shown in (a)) and $u_0 = 0.1$ (shown in (b)). The red and green disks are the size of disturbance and control, respectively, which are used in the safe set sculpting algorithm and shown here for scale. When obtaining a *partially controlled* trajectory, we sample values ξ_n from $[-\xi_0, \xi_0]$ and obtain \mathbf{u}_n by computing distance from the safe set. Safe set in Fig.(a) corresponds to the minimum control (in the sense of upper bound) that is needed for the given disturbance, and below $u_0 = 0.061$ the safe set does not exist. This is a critical value for partial control, however, this approach guarantees safety with $u_0 < \xi_0$ *ad infinitum*.

4.5 Discussion and Conclusions

Ship motion exemplifies a field where the application of phase space transport to higher dimensions is sorely needed, but where a conceptual framework for dealing with multi-degree of freedom problems has been lacking [76, 53]. Ship motion can be analytically modeled generally as a 6 degree of freedom system. Despite this, many models of ship dynamics focus on single-degree-of-freedom, reduced order models. But such models can be vulnerable to neglecting crucial dynamics. The ease of visualization of low dimensional dynamics has been part of their appeal. But couplings of multiple state variables can significantly alter predictions of safety versus capsizes, as emphasized by Refs. [59, 60, 82], and thus 2 or more degrees of freedom should be included.

In this study, we attempted to introduce conceptual aids for multi-degree degree of freedom systems which may help in the interpretation of dynamics which lead to capsizes.

Our approach was as follows.

- We considered first the dynamics of the underlying conservative system, which is itself non-trivial. These dynamics determine the phase space ‘skeleton’ upon which non-conservative forces, including random waves, are additional effects.
- In the simplest case of only two degrees of freedom, the phase space is of dimension four and the boundary between non-capsizes and capsizes states is given by a well-defined *transition state* (to use language borrowed from chemistry, but which has greater applicability [83, 11, 84]).
- The set of all states leading to capsizes can be understood as residing within a hyper-cylindrical manifold or tube, as in Fig. 4.3.2. This tube is the set of all states which will soon reach the transition state [64, 85]. From a probabilistic point of view, states in the tube will reach capsizes with probability 1, while those outside have probability 0.

- With the addition of random wave forcing, the ensemble of trajectories leading to capsizes is seen to be a smoothed probability distribution which shadows the underlying conservative system, as in as in Figs. 4.3.5 and 4.3.6. The peak probabilities match those from the conservative case. In the ensemble limit, small amplitude random waves are effectively noise, albeit bounded noise.
- However, this behavior also persists even for large amplitude random forcing (Fig. 4.5(b) and 4.6(b)), and hence provides a more general framework to study escaping dynamics.

An appealing aspect of this approach is that, while results for $N = 2$ degrees of freedom were shown for ease of discussion, the approach is completely scalable to higher degrees of freedom, as has been demonstrated in other contexts [84]. For example, when $N > 2$ periodic orbits are \mathbb{S}^{2N-3} and will need computation of their associated invariant manifolds. This is key, as it makes the approach attractive for the systematic analysis of multi-degree of freedom ship motions [53], up to and including all the degrees of freedom. Moreover, the tubes are also robust in the sense of predicting high probability regions of escape even in the presence of random forcing.

The foregoing study lays the foundation for a new approach to the avoidance of capsizes. For instance, avoidance of capsizes can be achieved by controlling a trajectory just enough to avoid entering the escaping zone on the surface-of-section. Future work will on control will be forthcoming.

4.6 Acknowledgments

This work was supported by the National Science Foundation under award 1150456 and 1537349. The authors would like to thank Tom Battista, Craig Woolsey, Leigh McCue, and Michele Cooper for useful discussions.

References

- [11] Charles Jaffé, Shane Ross, Martin Lo, Jerrold Marsden, David Farrelly, and T. Uzer, Statistical Theory of Asteroid Escape Rates, *Physical Review Letters*, 89.1 (2002), 011101
- [12] J M T Thompson and M S Soliman, Fractal Control Boundaries of Driven Oscillators and their Relevance to Safe Engineering Design, *Proceedings of the Royal Society A: Mathematical, Physical and Engineering Sciences*, 428.1874 (1990), 1–13
- [14] J. M. T. Thompson and J. R. D. Souza, Suppression of Escape by Resonant Modal Interactions: In Shell Vibration and Heave-Roll Capsize, *Proceedings of the Royal Society A: Mathematical, Physical and Engineering Sciences*, 452.1954 (1996), 2527–2550
- [41] Mohamed S. Soliman and J. M. T. Thompson, Transient and steady state analysis of capsize phenomena, *Applied Ocean Research*, 13.2 (1991), 82–92
- [43] C. Jiang, A. W. Troesch, and S. W. Shaw, Capsize criteria for ship models with memory-dependent hydrodynamics and random excitation, *Philosophical Transactions of the Royal Society A: Mathematical, Physical and Engineering Sciences*, 358.1771 (2000), 1761–1791
- [44] Jeffrey M. Falzarano, Steven W. Shaw, and Armin W. Troesch, Application of global methods for analyzing dynamical systems to ship rolling motion and capsizing, *International Journal of Bifurcation and Chaos*, 2 (1992), 101–115
- [45] I. Senjanovic, G. Cipric, J. Parunov, and J. Senjanovic, I. and Cipric, G. and Parunov, Survival Analysis of Fishing Vessels Rolling in Rough Seas, *Philosophical Transactions: Mathematical, Physical and Engineering Sciences*, 358.1771 (2000), 1943–1965
- [53] K. J. Spyrou and J. M. T. Thompson, The nonlinear dynamics of ship motions: a field overview and some recent developments, *Philosophical Transactions of the Royal*

- Society A: Mathematical, Physical and Engineering Sciences*, 358.1771 (2000), 1735–1760
- [54] Huan Lin and Solomon C S Yim, Chaotic roll motion and capsize of ships under periodic excitation with random noise, *Applied Ocean Research*, 17.3 (1995), 185–204
- [55] J. Randolph Paulling and R. M. Rosenberg, On Unstable Ship Motions Resulting From Nonlinear Coupling, *Journal of Ship Research*, 3 (1959), 36–46
- [56] Ali H. Nayfeh, Dean T. Mook, and Larry R. Marshall, Nonlinear Coupling of Pitch and Roll Modes in Ship Motions, *Journal of Hydronautics*, 7.4 (1973), 145–152
- [57] Ali H. Nayfeh, Dean T. Mook, and Larry R. Marshall, Perturbation-Energy Approach for the Development of the Nonlinear Equations of Ship Motion, *Journal of Hydronautics*, 8.4 (1974), 130–136
- [58] Dean T Mook, Larry R Marshall, and All H Nayfeh, Subharmonic and Superharmonic Resonances in the Pitch and Roll Modes of Ship Motions, *Journal of Hydronautics*, 8.1 (1974), 32–40
- [59] Leigh S. McCue and Armin W. Troesch, The effect of coupled heave/heave velocity or sway/sway velocity initial conditions on capsize modeling, *Proceedings of the 8th International Conference on Stability of Ships and Ocean Vehicles, Madrid, Spain, 2003*, 521–529
- [60] Leigh McCue and Armin Troesch, Probabilistic determination of critical wave height for a multi-degree of freedom capsize model, *Ocean Engineering*, 32.13 (2005), 1608–1622
- [61] L. McCue, C. Bassler, and W. Belknap, Real-time Identification of Behavior Leading to Capsize, *Proceedings of the 9th International Conference on Stability of Ships and Ocean Vehicles, Rio de Janeiro, Brazil, 2006*
- [62] Marcelo A.S. Neves and Claudio A. Rodríguez, On unstable ship motions resulting from strong non-linear coupling, *Ocean Engineering*, 33.14-15 (2006), 1853–1883

- [63] Marcelo A.S. Neves and Claudio A. Rodríguez, A coupled non-linear mathematical model of parametric resonance of ships in head seas, *Applied Mathematical Modelling*, 33.6 (2009), 2630–2645
- [64] Wang Sang Koon, Martin W. Lo, Jerrold E. Marsden, and Shane D. Ross, Heteroclinic connections between periodic orbits and resonance transitions in celestial mechanics. *Chaos (Woodbury, N. Y.)*, 10.2 (2000), 427–469
- [65] Wang-Sang Koon, Jerrold E Marsden, Shane D Ross, Martin Lo, and Daniel J Scheeres, Geometric mechanics and the dynamics of asteroid pairs. *Annals of the New York Academy of Sciences*, 1017 (2004), 11–38
- [66] Tristan Perez, *Ship Motion Control*. Advances in Industrial Control London: Springer-Verlag, 2005 chap. 2
- [67] Miguel Angel Sepulveda and Eric J. Heller, Semiclassical analysis of hierarchical spectra, *The Journal of Chemical Physics*, 101.9 (1994), 8016
- [68] Dmytro Babyuk, Robert E. Wyatt, and John H. Frederick, Hydrodynamic analysis of dynamical tunneling, *The Journal of Chemical Physics*, 119.13 (2003), 6482
- [69] R Barrio, F Blesa, and S Serrano, Bifurcations and safe regions in open Hamiltonians, *New Journal of Physics*, 11.5 (2009), 053004
- [70] Wang Sang Koon, Martin W Lo, Jerrold E Marsden, and Shane D Ross, Dynamical systems, the three-body problem and space mission design, 21 (2011), 327
- [71] Jurgen Moser, On the generalization of a theorem of A. Liapounoff, *Communications on Pure and Applied Mathematics*, XI (1958), 257–271
- [72] K. R. Meyer, G. R. Hall, and D. Offin, *Introduction to Hamiltonian Dynamical Systems and the N-Body Problem* Springer, 2009

- [73] Wang Sang Koon, Martin W. Lo, Jerrold E. Marsden, and Shane D. Ross, Heteroclinic connections between periodic orbits and resonance transitions in celestial mechanics. *Chaos (Woodbury, N. Y.)*, 10.2 (2000), 427–469
- [74] Jerrold E. Marsden and Shane D. Ross, New methods in celestial mechanics and mission design, *Bulletin of the American Mathematical Society*, 43.1 (2006), 43–73
- [75] Tristan Perez and Mogens Blanke, Ship roll motion control, *Proceedings of the 8th IFAC Conference on Control Applications in Marine Systems, Rostock, Germany*, 2010, 1–12
- [76] Shang-Rou Hsieh, Armin W. Troesch, and Steven W. Shaw, A Nonlinear Probabilistic Method for Predicting Vessel Capsizing in Random Beam Seas, *Proceedings of the Royal Society A: Mathematical, Physical and Engineering Sciences*, 446.1926 (1994), 195–211
- [77] Juan Sabuco, Samuel Zambrano, Miguel A F Sanjuán, and James A. Yorke, Finding safety in partially controllable chaotic systems, *Communications in Nonlinear Science and Numerical Simulation*, 17.11 (2012), 4274–4280
- [78] Juan Sabuco, Miguel a F Sanjuán, and James a Yorke, Dynamics of partial control. *Chaos (Woodbury, N. Y.)*, 22.4 (2012), 047507
- [79] Samuel Zambrano, Miguel a. F. Sanjuán, and James a. Yorke, Partial control of chaotic systems, *Physical Review E*, 77.5 (2008), 055201
- [80] Ying-Cheng Lai and Tamás Tél, *Transient Chaos* vol. 48 1 Springer-Verlag, 2010, 146–146
- [81] Mattia Coccolo, Jesús M Seoane, Samuel Zambrano, and Miguel a. F Sanjuán, Partial Control of Escapes in Chaotic Scattering, *International Journal of Bifurcation and Chaos*, 23.01 (2013), 1350008
- [82] Y.-W. Lee, L. S. McCue, M. S. Obar, and A. W. Troesch, Experimental and numerical investigation into the effects of initial conditions on a three degree of freedom capsize model, *Journal of Ship Research*, 50.1 (2006), 63–84

- [83] C Jaffé, D Farrelly, and T Uzer, Transition state in atomic physics, *Phys Rev A*, 60.5 (1999), 3833–3850
- [84] Frederic Gabern, Wang S. Koon, Jerrold E. Marsden, and Shane D. Ross, Theory and computation of non-RRKM lifetime distributions and rates in chemical systems with three or more degrees of freedom, *Physica D: Nonlinear Phenomena*, 211.3-4 (2005), 391–406
- [85] F. Gabern, W. S. Koon, J. E. Marsden, S. D. Ross, and T. Yanao, Application of tube dynamics to non-statistical reaction processes, *Few-Body Systems*, 38.2-4 (2006), 167–172

Appendix C

C.1 The Linearized Hamiltonian system

The geometry of motion near the rank-1 saddle is explained by writing the Hamiltonian in its normal form which is obtained using a linear transformation and in this section, we present the details of this method. We note that the Hamiltonian for the rescaled system can be obtained via the usual Legendre transformation of the Lagrangian (4.2.4) and is given by

$$H(x, y, p_x, p_y) = \frac{1}{2}p_x^2 + \frac{1}{2}\left(\frac{R^2}{2}\right)p_y^2 + \frac{1}{2}x^2 + y^2 - x^2y \quad (\text{C.1-1})$$

We know the canonical form of the equations of motion in terms of the Hamiltonian for n degrees of freedom is given by

$$\begin{Bmatrix} \dot{\mathbf{q}} \\ \dot{\mathbf{p}} \end{Bmatrix} = J\nabla H \quad (\text{C.1-2})$$

$$\text{where, } J = \begin{bmatrix} 0_n & I_n \\ -I_n & 0_n \end{bmatrix} \quad (\text{C.1-3})$$

is the symplectic $2n \times 2n$ matrix, $\{\mathbf{q}, \mathbf{p}\} = \{q_1, q_2, \dots, q_n; p_1, p_2, \dots, p_n\} \in \mathbb{R}^{2n}$ are the generalized coordinates, 0_n is the zero matrix of size $n \times n$, and I_n is the identity matrix of size

$n \times n$. The equations of motion associated the Hamiltonian (C.1-1) are given by

$$\begin{aligned}
 \dot{x} &= \frac{\partial H}{\partial p_x} = p_x \\
 \dot{y} &= \frac{\partial H}{\partial p_y} = \frac{R^2}{2} p_y \\
 \dot{p}_x &= -\frac{\partial H}{\partial x} = -x + 2xy \\
 \dot{p}_y &= -\frac{\partial H}{\partial y} = -2y + x^2
 \end{aligned}
 \tag{C.1-4}$$

Eigenvalues and eigenvectors. The saddle equilibrium points are at $(\pm 1, 1/2, 0, 0)$ and the center equilibrium point is at $(0, 0, 0, 0)$. The linearization of the equations of motion is given by

$$\mathbb{J}_{(x,y,p_x,p_y)} = \begin{bmatrix} 0 & 0 & 1 & 0 \\ 0 & 0 & 0 & R^2/2 \\ -1 + 2y & 2x & 0 & 0 \\ 2x & -2 & 0 & 0 \end{bmatrix}
 \tag{C.1-5}$$

which are evaluated at the equilibrium points $(1, 1/2, 0, 0)$ becomes

$$\mathbb{J}_{(x,y,p_x,p_y)} = \begin{bmatrix} 0 & 0 & 1 & 0 \\ 0 & 0 & 0 & R^2/2 \\ 0 & 2 & 0 & 0 \\ 2 & -2 & 0 & 0 \end{bmatrix} = M
 \tag{C.1-6}$$

The characteristic polynomial is given by

$$\begin{aligned}
p(\beta) = \det(M - \beta I) &= \begin{vmatrix} -\beta & 0 & 1 & 0 \\ 0 & -\beta & 0 & R^2/2 \\ 0 & 2 & -\beta & 0 \\ 2 & -2 & 0 & -\beta \end{vmatrix} \\
&= -\beta \begin{vmatrix} -\beta & 0 & R^2/2 \\ 2 & -\beta & 0 \\ -2 & 0 & -\beta \end{vmatrix} + 1 \begin{vmatrix} 0 & -\beta & R^2/2 \\ 0 & 2 & 0 \\ 2 & -2 & -\beta \end{vmatrix} \\
&= -\beta(-\beta(\beta^2 - 0) + R^2/2(0 - 2\beta)) + 1(\beta(0 - 0) + R^2/2(0 - 4)) \\
&= -\beta(-\beta^3 - 2\beta(R^2/3)) + (-2R^2) \\
p(\beta) &= \beta^4 + R^2\beta^2 - 2R^2
\end{aligned}$$

Let $\alpha = \beta^2$, then the roots of $p(\alpha) = 0$ are as follows

$$\alpha_1 = \frac{-R^2 + R\sqrt{8 + R^2}}{2} \quad (\text{C.1-7})$$

$$\alpha_2 = \frac{-R^2 - R\sqrt{8 + R^2}}{2} \quad (\text{C.1-8})$$

Since $R > 0$ always, being the ratio of frequencies, and the $\sqrt{8 + R^2} > R$, we know $\alpha_1 > 0$ and $\alpha_2 < 0$. Thus, let us define $\lambda = \sqrt{\alpha_1}$ and $\nu = \sqrt{-\alpha_2}$.

Now, we want to find the eigenvectors of matrix (C.1-6) and use them to construct a symplectic linear change of variables which will cast (C.1-1) into its real normal form.

Let us assume the eigenvector to be $v = (k_1, k_2, k_3, k_4)$ and thus, $M\beta = \beta v$ gives the following

equations:

$$\begin{aligned}
 k_3 &= \beta k_1 \\
 \frac{R^2}{2} k_4 &= \beta k_2 \\
 2k_2 &= \beta k_3 \\
 2k_1 - 2k_2 &= \beta k_4
 \end{aligned}$$

Let $k_1 = 1$, then the eigenvector has a form $(1, k_2, \beta, \frac{2\beta k_2}{R^2})$. Thus using the third and fourth equations for the eigenvalue $\beta = \lambda$ and $\beta = -\lambda$, we get

$$\begin{aligned}
 2k_2 &= \lambda^2 \\
 1 - k_2 &= \frac{\lambda^2}{R^2} k_2 \\
 2k'_2 &= (-\lambda)^2 \\
 1 - k'_2 &= \frac{(-\lambda)^2}{R^2} k'_2
 \end{aligned}$$

which implies $k_2 = k'_2$ and let $k_2 = \sigma$, using the last equation we get

$$\sigma = \frac{R^2}{R^2 + \lambda^2} \tag{C.1-9}$$

Thus, using the third and fourth equations for the eigenvalue $\beta = i\nu$ and $\beta = -i\nu$, we get

$$\begin{aligned}
 2k_2 &= -\nu^2 \\
 1 - k_2 &= -\frac{\nu^2}{R^2} k_2 \\
 2k'_2 &= (-i\nu)^2 \\
 1 - k'_2 &= \frac{(-i\nu)^2}{R^2} k'_2
 \end{aligned}$$

which again implies $k_2 = k'_2$ and let $k_2 = \tau$, using the last equation we get

$$\tau = \frac{2\nu}{R^2 - \nu^2}$$

Thus, the eigenvectors associated with eigenvalues $\pm\lambda$ becomes

$$u_\lambda = \left[1, \frac{R^2}{R^2 + \lambda^2}, \lambda, \frac{2\lambda}{R^2 + \lambda^2} \right]$$

$$u_{-\lambda} = \left[1, \frac{R^2}{R^2 + \lambda^2}, -\lambda, -\frac{2\lambda}{R^2 + \lambda^2} \right]$$

and for the eigenvalue $i\nu$, we separate the real and imaginary parts as $u_\nu + iv_\nu$ to obtain the two eigenvectors

$$u_\nu = \left[1, \frac{R^2}{R^2 - \nu^2}, 0, 0 \right]$$

$$v_\nu = \left[0, 0, \nu, \frac{2\nu}{R^2 - \nu^2} \right]$$

Symplectic change of variables. Next, we consider the transformation given by the matrix C which is formed using the eigenvectors as the basis and is given by

$$C = [u_\lambda, u_\nu, -u_{-\lambda}, v_\nu] \tag{C.1-10}$$

To check whether this transformation is symplectic, that is the transformed Hamiltonian is in the normal form, we check the condition $C^T J C = J$ to obtain

$$C^T J C = \begin{bmatrix} 0_n & D \\ -D & 0_n \end{bmatrix} \quad \text{where,} \quad D = \begin{bmatrix} d_\lambda & 0 \\ 0 & d_\nu \end{bmatrix} \tag{C.1-11}$$

where 0_n is the zero matrix of size $n \times n$. The resulting structure can be obtained if we note that the factor $1 + \frac{2R^2}{(R^2 - \nu^2)(R^2 + \lambda^2)} = 0$ when the values of $\lambda = \sqrt{\alpha_1}$ and $\nu = \sqrt{-\alpha_2}$

is substituted from (C.1-7) and (C.1-8). Thus, the transformation matrix C is symplectic when scaled using the factors $s_1 = \sqrt{2d_\lambda}$ and $s_2 = \sqrt{d_\nu}$. These are given by

$$d_\lambda = \lambda + \frac{R^2}{R^2 + \lambda^2} \frac{2\lambda}{R^2 + \lambda^2} \quad (\text{C.1-12})$$

$$d_\nu = \nu + \frac{R^2}{R^2 - \nu^2} \frac{2\nu}{R^2 - \nu^2} \quad (\text{C.1-13})$$

and it is easy to check $d_\lambda > 0$, $d_\nu > 0$. This implies that the final change is given by the symplectic transformation matrix C

$$\begin{bmatrix} 1/s_1 & 1/s_2 & -1/s_1 & 0 \\ \frac{R^2}{s_1(R^2+\lambda^2)} & \frac{R^2}{s_2(R^2-\nu^2)} & -\frac{R^2}{s_1(R^2+\lambda^2)} & 0 \\ \lambda/s_1 & 0 & \lambda/s_1 & \nu/s_2 \\ \frac{2\lambda}{s_1(R^2+\lambda^2)} & 0 & \frac{2\lambda}{s_1(R^2+\lambda^2)} & \frac{2\nu}{s_2(R^2-\nu^2)} \end{bmatrix} \quad (\text{C.1-14})$$

which transforms the coordinates (x, y, p_x, p_y) into (q_1, q_2, p_1, p_2) and that casts Hamiltonian into its normal form given by

$$H(q_1, q_2, p_1, p_2) = \lambda q_1 p_1 + \frac{\nu}{2}(q_2^2 + p_2^2) \quad (\text{C.1-15})$$

Thus, the linearized equations of motion near the saddle $(1, 1/2, 0, 0)$ are

$$\begin{aligned} \dot{q}_1 &= \lambda q_1 & \dot{p}_1 &= -\lambda p_1 \\ \dot{q}_2 &= \nu p_2 & \dot{p}_2 &= -\nu q_2 \end{aligned} \quad (\text{C.1-16})$$

and the solutions of the equations (C.1-16) is written as

$$\begin{aligned} q_1(t) &= q_1^0 e^{\lambda t} & p_1(t) &= p_1^0 e^{-\lambda t} \\ q_2(t) + ip_2(t) &= (q_2^0 + ip_2^0) e^{-i\nu t} \end{aligned} \quad (\text{C.1-17})$$

where the constants $q_1^0, p_1^0, q_2^0 + ip_2^0$ are the initial conditions. These linearized equations

admit integrals in addition to the Hamiltonian function; namely, the functions $q_1 p_1$, $q_2^2 + p_2^2$ are constant along solutions.

C.2 Geometry of solutions near equilibria

The geometric view of the solutions near the equilibria, C_1 and C_2 , is studied using the eigenbases for linearized equations of motion around these points. Let us consider the right equilibrium point, C_2 , and the results for left equilibrium point, C_1 , follows from symmetry, s_x .

Eigenvalues and eigenvectors. We compute the Jacobian of the vector field about this point and the linear system is now given by

$$\begin{pmatrix} \dot{x} \\ \dot{y} \\ \dot{v}_x \\ \dot{v}_y \end{pmatrix} = D\mathbf{f}|_{(x_e, y_e, 0, 0)} \begin{pmatrix} x \\ y \\ v_x \\ v_y \end{pmatrix} = \begin{bmatrix} 0 & 0 & 1 & 0 \\ 0 & 0 & 0 & 1 \\ 0 & 2 & 0 & 0 \\ R^2 & -R^2 & 0 & 0 \end{bmatrix} \begin{pmatrix} x \\ y \\ v_x \\ v_y \end{pmatrix} \quad (\text{C.2-1})$$

for which the eigenvalues are obtained by solving the characteristic polynomial

$$\beta^4 + R^2 \beta^2 - 2R^2 = 0 \quad (\text{C.2-2})$$

Due to the simpler form of the above 4th order polynomial, the roots can be written as

$$\beta^2 = \frac{-R^2 \pm \sqrt{R^4 - 4(-2R^2)}}{2}$$

$$\beta = \pm \sqrt{\frac{R^2}{2} \left(-1 \pm \sqrt{1 + \frac{8}{R^2}} \right)}$$

Thus, the eigenvalues are of the form $\pm\lambda$ and $\pm i\nu$, where

$$\lambda = \sqrt{\frac{R^2}{2} \left(\sqrt{1 + \frac{8}{R^2}} - 1 \right)} \quad \nu = \sqrt{\frac{R^2}{2} \left(\sqrt{1 + \frac{8}{R^2}} + 1 \right)} \quad (\text{C.2-3})$$

These eigenvalues classify the equilibrium point C_2 (and C_1 due to symmetry s_x) as rank-1 saddle which, in general, means they possess one saddle direction and are center in all other directions. Thus, the eigenvectors corresponding to $\pm\lambda$ are of saddle type and the eigenvalues corresponding to $\pm i\nu$ are of center type that is periodic motion.

Let $v = (k_1, k_2, k_3, k_4)$ denote the eigenvector corresponding to the eigenvalue λ and the Jacobian matrix at C_2 is denoted by $A = D\mathbf{f}|_{(x_e, y_e, 0, 0)}$, then $Av = \alpha v$ gives

$$\begin{aligned} k_3 &= \lambda k_1 & k_4 &= \lambda k_2 \\ 2k_2 &= \lambda k_3 & R^2(k_1 - k_2) &= \lambda k_4 \end{aligned}$$

Let $k_1 = 1$, then using the first set of equations, the eigenvector is of the form $(1, k_2, \lambda, \lambda k_2)$ and we can solve λ, k_2 for different eigenvalues. For the real eigenvalues $\pm\lambda$, we obtain:

$$u_1 = \left(1, \frac{R^2}{R^2 + \lambda^2}, \lambda, \frac{\lambda R^2}{R^2 + \lambda^2} \right) \quad (\text{C.2-4})$$

$$u_2 = \left(1, \frac{R^2}{R^2 + \lambda^2}, -\lambda, -\frac{\lambda R^2}{R^2 + \lambda^2} \right) \quad (\text{C.2-5})$$

For the complex conjugate eigenvalues $\pm i\nu$, we obtain:

$$w_1 = \left(1, \frac{R^2}{R^2 - \nu^2}, i\nu, \frac{i\nu R^2}{R^2 - \nu^2} \right) \quad (\text{C.2-6})$$

$$w_2 = \left(1, \frac{R^2}{R^2 - \nu^2}, -i\nu, -\frac{i\nu R^2}{R^2 - \nu^2} \right) \quad (\text{C.2-7})$$

where, λ and ν are positive constants given by (C.2-3). Thus, the general solution of the

linear system C.2-1 is given by

$$\mathbf{x}(t) = \{x(t), y(t), v_x(t), v_y(t)\} = \alpha_1 e^{\lambda t} u_1 + \alpha_2 e^{-\lambda t} u_2 + 2\text{Re}(\beta e^{i\nu t} w_1) \quad (\text{C.2-8})$$

where, α_1, α_2 are real and $\beta = \beta_1 + i\beta_2$ is complex. However, we can use the eigenvectors to define a coordinate system that makes this picture more clearer.

Eigenvectors as axes for new coordinate system. To better understand the orbit structure on the phase space, we make a linear change of coordinates with the eigenvectors: u_1, u_2, w_1, w_2 , as the axes of the new system. Using the corresponding new coordinates $(\xi, \eta, \zeta_1, \zeta_2)$, the equations of motion near the equilibrium points assume the simple form:

$$\begin{aligned} \dot{\xi} &= \lambda \xi \\ \dot{\eta} &= -\lambda \eta \\ \dot{\zeta}_1 &= \nu \zeta_2 \\ \dot{\zeta}_2 &= -\nu \zeta_1 \end{aligned} \quad (\text{C.2-9})$$

and the energy integral for the linearized system becomes

$$E_l = \lambda \xi \eta + \frac{\nu}{2} (\zeta_1^2 + \zeta_2^2) \quad (\text{C.2-10})$$

Thus, the solutions of the equations (C.2-9) can be written as

$$\begin{aligned} \xi(t) &= \xi^0 \exp^{\lambda t} \\ \eta(t) &= \eta^0 \exp^{-\lambda t} \\ \zeta(t) &= \zeta_1(t) + i\zeta_2(t) = \zeta^0 \exp^{-i\nu t} \end{aligned} \quad (\text{C.2-11})$$

where, the constants ξ^0, η^0 , and $\zeta^0 = \zeta_1^0 + i\zeta_2^0$ are the initial conditions. These linearized equations admit integrals in addition to the energy function (C.2-10); namely the functions

$\xi\eta$ and $|\zeta|^2 = \zeta_1^2 + \zeta_2^2$ are both constant along solutions.

Local integrals in equilibrium region. The geometric view of solution near the equilibrium points is based on expressing the Hamiltonian in normal form which is based on Moser's Theorem. We present the discussion from [70] for the sake of completeness. Suppose we have a time-dependent, analytic Hamiltonian system of differential equations with two degrees of freedom. Suppose these equations have a non-degenerate equilibrium point with one pair of real and one pair of imaginary eigenvalues, $\pm\lambda$ and $\pm i\nu$. We can assume, without loss of generality, that the phase space coordinates (q_1, q_2, p_1, p_2) are chosen so that the Hamiltonian function assumes the following form:

$$H(q, p) = \lambda q_1 p_1 + \frac{\nu}{2}(q_2^2 + p_2^2) + \mathcal{O}_3(q, p),$$

where $q = (q_1, q_2)$, $p = (p_1, p_2)$ and the symbol $\mathcal{O}_n(\cdot, \cdot)$ denotes terms of order n or higher in the variables. In particular, the equilibrium point has coordinates $p = q = 0$ and the differential equations are obtained from H as

$$\begin{aligned} \dot{q}_1 &= H_{p_1} = \lambda q_1 + \mathcal{O}_2(q, p) \\ \dot{q}_2 &= H_{p_2} = \nu p_2 + \mathcal{O}_2(q, p) \\ \dot{p}_1 &= -H_{q_1} = -\lambda p_1 + \mathcal{O}_2(q, p) \\ \dot{p}_2 &= -H_{q_2} = \nu q_2 + \mathcal{O}_2(q, p) \end{aligned} \tag{C.2-12}$$

The linearized equations are similarly obtained from a Hamiltonian function which consists of the quadratic terms of H , or equivalently, by dropping the terms of order two or higher in the above equations. Solution of these linearized equations are conveniently written as

$$\begin{aligned} q_1(t) &= q_1^0 e^{\lambda t} & p_1(t) &= p_1^0 e^{-\lambda t} \\ q_2(t) + ip_2(t) &= (q_2^0 + ip_2^0) e^{-i\nu t} \end{aligned} \tag{C.2-13}$$

where the constants q_1^0 , p_1^0 , and $q_2^0 + ip_2^0$ are the initial conditions. These linearized equations admit integrals in addition to the Hamiltonian function; namely, the functions $q_1 p_1$ and $q_2^2 + p_2^2$ are constant along solutions. A generalization of Lyapunov's theorem in [71] states that the full non-linear equations admit "local" integrals analogous to these via power series in q and p that start with quadratic terms $q_1 p_1$ and $q_2^2 + p_2^2$. It is also shown in [71] that the power series converges in some neighborhood of $q_1 = p_1 = 0$ and such that the corresponding functions are constants along pieces of solutions lying in the domain of convergence.

Moser's theorem. Let $q = p = 0$ correspond to a critical point as described above, then there exists a (real) analytic, transformation

$$\begin{aligned} q_1 &= \xi + \mathcal{O}_2(\xi, \eta, \zeta, \bar{\zeta}), \\ p_1 &= \eta + \mathcal{O}_2(\xi, \eta, \zeta, \bar{\zeta}), \\ q_2 + ip_2 &= \zeta + \mathcal{O}_2(\xi, \eta, \zeta, \bar{\zeta}) \end{aligned} \tag{C.2-14}$$

as well as power series α and β in the variables $\chi = \xi\eta$ and $|\zeta|^2$ of the form

$$\begin{aligned} \alpha &= \lambda + \mathcal{O}_1(\chi, |\zeta|^2) \\ \beta &= -i\nu + \mathcal{O}_1(\chi, |\zeta|^2) \end{aligned} \tag{C.2-15}$$

such that solutions of the transformed equations are given by

$$\begin{aligned} \xi(t) &= \xi^0 e^{t\alpha} & \eta(t) &= \eta^0 e^{-t\alpha} \\ \zeta(t) &= \zeta^0 e^{t\beta} & \bar{\zeta}(t) &= \bar{\zeta}^0 e^{-t\beta} \end{aligned} \tag{C.2-16}$$

where, ξ^0 , η^0 , and ζ^0 are determined from the initial conditions and $\bar{\zeta}$ is the complex conjugate of ζ . Furthermore, the coefficients of α and β are real and complex, respectively, from which it follows that the functions $\xi\eta = q_1 p_1 + \mathcal{O}_3(q, p)$ and $|\zeta|^2 = q_2^2 + p_2^2 + \mathcal{O}_3(q, p)$ are local integrals, as are α and β . Thus, the transformation of the Hamiltonian function has the

form

$$\Gamma(\xi, \eta, \zeta, \bar{\zeta}) = H(q, p) = \lambda\xi\eta + \frac{1}{2}|\zeta|^2 + \mathcal{O}_2(\chi, |\zeta|^2) \quad (\text{C.2-17})$$

and in particular depends only on the variables $\chi = \xi\eta$ and $|\zeta|^2$.

Flow in the equilibrium region. Consider a neighborhood of C_i , for $i = 1$ or $i = 2$ and fixed energy e , in the energy surface, then we refer to this neighborhood as the **equilibrium region** and denote it by \mathcal{R} on the energy surface. The position space configuration will be denoted by R .

For positive e_l and c , the region \mathcal{R} , which is determined by

$$E_l = e_l \quad \text{and,} \quad |\eta - \xi| \leq c \quad (\text{C.2-18})$$

which is homeomorphic to the product of a two-sphere and an interval; that is, for fixed value of $\eta - \xi$ on the interval $I = [-c, c]$, the equation $E_l = e_l$ defines the two-sphere

$$\frac{\lambda}{4}(\eta + \xi)^2 + \frac{\nu}{2}(\zeta_1^2 + \zeta_2^2) = e_l + \frac{\lambda}{4}(\eta - \xi)^2 \quad (\text{C.2-19})$$

The bounding sphere of \mathcal{R} for which $\eta - \xi = -c$ will be called n_1 , and where $\eta - \xi = c$, will be called n_2 . We shall call the set of points on each bounding sphere where $\eta + \xi = 0$ as the *equator*, and the sets where $\eta + \xi > 0$ or $\eta + \xi < 0$ will be called the *north* and *south* hemispheres, respectively.

To analyze the flow in \mathcal{R} one simply considers the projections on the $\eta - \xi$ plane and ζ planes, respectively. In the first case, we see the standard picture of an unstable equilibrium point, and in the second, of a center. Fig. C.2.1 illustrates the flow in the $\eta - \xi$ plane with the coordinate axes tilted by 45° . In Fig. C.2.1(b), \mathcal{R} itself projects to a set bounded on two sides by the hyperbola $\eta - \xi = e/\lambda$, denoted by thick solid hyperbolic segments on the top

and bottom. \mathcal{R} is bounded on two other two sides by the line segments $\eta - \xi = \pm c$, denote by dotted vertical lines on the left and right, which correspond to the bounding spheres, n_1 and n_2 , respectively. Since $\eta\xi$ is an integral of the equations in \mathcal{R} , the projections of orbits

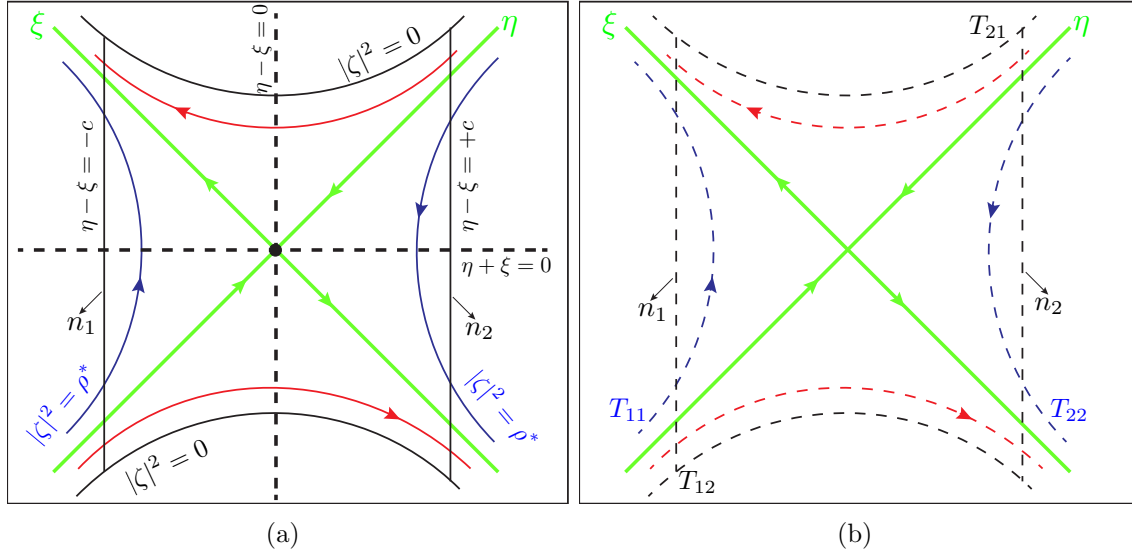


Figure C.2.1: The projection onto the $\eta - \xi$ plane of orbits near the equilibrium point; the $\eta - \xi$ axis is rotated by 45° . (a) Shows the equilibrium region, \mathcal{R} , is bounded by the thick hyperbolic segments at top and bottom and the dotted vertical segments at left and right. At the origin is the periodic orbit in \mathcal{R} . The thick lines with arrows pointing toward or away from the origin are trajectories asymptotically winding onto the periodic orbit. (b) Shows four additional trajectories. The label T_{ij} denotes the path of a particle which entered \mathcal{R} through n_i and exited through n_j . Two transit orbits, T_{12} and T_{21} , and two non-transit orbits, T_{11} and T_{22} , are shown.

in the $\eta - \xi$ plane move on the branches of the corresponding hyperbolas $\eta\xi = e/\lambda$, except in the case $\eta\xi = 0$. If $\eta\xi > 0$, the branches connect the bounding line segments $\eta - \xi = \pm c$ and if $\eta\xi < 0$, they have both end points on the same segment. A check of equation (C.2-16) shows that the orbits move as indicated by the arrows in Fig. C.2.1.

To interpret Fig. C.2.1 as a flow in \mathcal{R} , notice that each point in the projection corresponds to a circle in \mathcal{R} given by the “radius” variable $\rho = |\zeta|^2 = \text{constant}$. We recall from (C.2-10) that $|\zeta|^2 = \frac{2}{\nu}(e - \lambda\eta\xi)$ and for points on the bounding hyperbolic segments $\eta - \xi = e/\lambda$, the constant is zero so that the circle collapses to a point. Thus, the segments of the lines $\eta - \xi = \pm c$ in the $\eta - \xi$ projection correspond to the two-spheres bounding \mathcal{R} . Since each

corresponds to a circle crossed with an interval where the two end circles are pinched to a point.

Thus, we can distinguish between nine classes of orbits grouped into four categories:

1. The point at the origin in Fig. C.2.1(a), $\xi = \eta = 0$, corresponds to a **periodic orbit** in \mathcal{R}
2. The four half-open segments on the axes, $\eta\xi = 0$ (or equivalently $|\zeta|^2 = \rho^*$ where $\rho^* = 2e/\nu$), correspond to four cylinders of orbits asymptotic to this periodic solution either as time increases ($\xi = 0$) or as time decreases ($\eta = 0$). These are called **asymptotic** orbits. These are drawn as the solid green lines with arrows pointing toward or away from the origin in Fig. C.2.1.
3. The hyperbolic segments determined by $\eta\xi = \text{constant} > 0$ (or equivalently $|\zeta|^2 < \rho$) correspond to two cylinders which cross \mathcal{R} from one bounding sphere to the other, meeting both in the same hemisphere; the north one if they go from $\eta - \xi = +c$ to $\eta - \xi = -c$, the south one in the other case. Since these orbits transit from one region to another, we call them **transit** orbits. The two trajectories labeled T_{12} and T_{21} in Fig. C.2.1(b).
4. Finally, the hyperbolic segments determined by $\eta\xi = \text{constant} < 0$ ($|\zeta|^2 > \rho^*$) correspond to two cylinders of orbits in \mathcal{R} each of which runs from one hemisphere to the other hemisphere on the same bounding sphere. Thus if $\eta > 0$, the sphere is n_1 ($\eta - \xi = -c$) and orbits run from the south ($\eta + \xi < 0$) to the north ($\eta + \xi > 0$) hemisphere while the converse holds if $\eta < 0$, where the sphere is n_2 . Since these orbits return to the same region, we call them **non-transit** orbits. These two trajectories are labeled T_{11} and T_{22} in Fig. C.2.1(b).

C.3 Derivation of coupling constant

For applying the methods developed for 1 DOF and 2 DOF model of ship dynamics, we need to estimate the ratio of second moment of inertia and the coupling constant for the ship, *Edith Terkol*. The ratio of pitch and roll natural frequencies is given by R , so we have

$$\omega_\theta = R\omega_\phi \quad (\text{C.3-1})$$

Furthermore, we know the angle of vanishing stability, ϕ_e and the corresponding pitch angle, θ_e is given by

$$\phi_e = \frac{\omega_\phi \omega_\theta}{K_1 \sqrt{2}} \sqrt{\frac{I_{yy}}{I_{xx}}}, \quad \theta_e = \frac{\omega_\phi^2}{2K_1}$$

Thus, we have

$$\theta_e = \frac{K_1 I_{xx}}{\omega_\theta^2 I_{yy}} \phi_e^2$$

Let us consider the equation of motion for roll degree of freedom and its nonlinear term involving K_1 in (4.2.1) for the angle of vanishing stability. So we have

$$\begin{aligned} 2K_1 \theta_e \phi_e &= 2K_1 \phi_e \left(\frac{K_1 I_{xx}}{\omega_\theta^2 I_{yy}} \phi_e^2 \right) = \frac{2K_1^2 I_{xx}}{\omega_\theta^2 I_{yy}} \phi_e^3 \\ &= \frac{2K_1^2 I_{xx}}{R^2 \omega_\phi^2 I_{yy}} \phi_e^3 \\ &= A \phi_e^3 \end{aligned}$$

Thus, the restoring moment (in terms of potential energy $V(\phi)$ this is $-\frac{dV}{d\phi}$) for roll dynamics is given by

$$M_\phi = -\omega_\phi^2 \phi + A \phi^3 = \phi (-\omega_\phi^2 + A \phi^2) \quad (\text{C.3-2})$$

which vanishes at instant of capsize, $\phi = \phi_e$. Thus, we have

$$A = \omega_\phi^2 / \phi_e^2 \quad (\text{C.3-3})$$

and for the ship *Edith Terkol*, $A = 0.5239 \text{ s}^{-2}$. Thus, computing the constant K_1 requires estimating the ratio of second moment of inertia assuming a solid rectangular parallelepiped. Using $L = 58.6 \text{ m}$, $B = 9.65 \text{ m}$, and $D = 4.15 \text{ m}$ (as shown in Fig. C.3.1) from Ref. [86] and the formula for I_{xx} and I_{yy} , we get

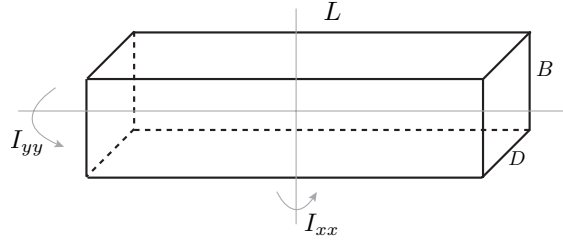


Figure C.3.1: Schematic of a solid rectangular parallelepiped that represents a ship

$$I_{xx} = \frac{m}{12} (D^2 + B^2)$$

and,

$$I_{yy} = \frac{m}{12} (L^2 + D^2)$$

which gives

$$\frac{I_{yy}}{I_{xx}} = \frac{L^2 + D^2}{B^2 + D^2} \quad (\text{C.3-4})$$

which on substitution of appropriate values gives 31.28. Thus, the coupling constant is given by

$$K_1 = \sqrt{\frac{A\omega_\phi^2 I_{yy}}{2 I_{xx}}} R \quad (\text{C.3-5})$$

C.4 Derivation of differential correction term

Let trajectories of the differential equation $\dot{x} = f(x)$, e.g. (4.2.6), with initial condition $x(t_0) = x_0$ be denoted by the flow map $\phi(t, t_0; x_0)$, or $\phi(t; x_0)$. In what follows, we note $x \in \mathbb{R}^n$ and $f : \mathbb{R}^n \rightarrow \mathbb{R}^n$ unless the specific case of $n = 4$ for 2 degree of freedom systems is mentioned. For the guess initial condition, $\bar{x}_{0,g}$, a first guess to an initial condition along a periodic orbit, a trajectory that starts from the perturbed initial vector $\bar{x}_0 + \delta\bar{x}_0$ evolved until $t + \delta t$ with the displacement

$$\delta\bar{x}(t + \delta t) = \phi(t + \delta t, t_0; \bar{x}_0 + \delta\bar{x}_0) - \phi(t, t_0; \bar{x}_0)$$

with respect to the first guess reference solution $\bar{x}(t)$. We compute the displacement at time $t_1 + \delta t_1$ using

$$\delta\bar{x}(t_1 + \delta t_1) = \phi(t_1 + \delta t_1, t_0; \bar{x}_0 + \delta\bar{x}_0) - \phi(t_1, t_0; \bar{x}_0) \quad (\text{C.4-1})$$

and expanding the right hand side using Taylor series, we get

$$\delta\bar{x}(t_1 + \delta t_1) = \frac{\partial\phi(t_1, t_0; \bar{x}_0)}{\partial x_0} \delta\bar{x}_0 + \frac{\partial\phi(t_1, t_0; \bar{x}_0)}{\partial t_1} \delta t_1 + h.o.t, \quad (\text{C.4-2})$$

$$= \frac{\partial\phi(t_1, t_0; \bar{x}_0)}{\partial x_0} \delta\bar{x}_0 + \dot{\bar{x}}_1 \delta t_1 + h.o.t, \quad (\text{C.4-3})$$

where the first part of the second term $\frac{\partial\phi(t_1, t_0; \bar{x}_0)}{\partial t_1}$ comes from $\frac{d\phi(t, t_0; \bar{x}_0)}{dt} = f(\phi(t, t_0; \bar{x}_0))$, which is the vector field after flowing for $t = t_1$ along the reference trajectory. The matrix, $\frac{\partial\phi(t_1, t_0; \bar{x}_0)}{\partial t_1}$, which satisfies the above relation to first order $\delta t_1 = 0$ is the state transition matrix (STM) denoted by $\Phi(t_1, t_0)$. The first term involving the derivative of a trajectory with respect to the initial condition at $t = t_1$ is given by

$$\delta\bar{x}(t_1) = \Phi(t_1, t_0) \delta\bar{x}_0$$

can be obtained numerically as a solution to the variational equations

$$\delta\dot{\bar{x}}(t) = Df(\bar{x}(t))\delta\bar{x} \quad (\text{C.4-4})$$

where $Df(\bar{x}(t))$ is the Jacobian of the vector field evaluated at $\bar{x}(t)$. Suppose we want to reach a desired endpoint, x_d , but

$$\bar{x}(t_1) = \phi(t_1, t_0; \bar{x}_0) = \bar{x}_1 = x_d - \delta\bar{x}_1$$

is slightly off ($|\delta\bar{x}_1| > d$) for a specified tolerance $d \ll 1$ and we need correction. Since,

$$\begin{aligned} \phi(t_1, t_0; \bar{x}_0 + \delta\bar{x}_0) &= \phi(t_1, t_0; \bar{x}_0) + \frac{\partial\phi(t_1, t_0; \bar{x}_0)}{\partial x_0} \delta\bar{x}_0 + h.o.t., \\ &= \phi(t_1, t_0; \bar{x}_0) + \Phi(t_1, t_0) \delta\bar{x}_0 + h.o.t., \\ &= \bar{x}_1 + \delta\bar{x}_1 + h.o.t., \\ &= x_d + h.o.t., \end{aligned}$$

which implies that changing \bar{x}_0 by

$$\delta\bar{x}_0 = \Phi(t_1, t_0)^{-1} \delta\bar{x}_1$$

will perform the correction to first order. By iteration, the process converges with the criteria:

$$\|\phi(t_1, t_0; \bar{x}_0 + \Delta\bar{x}_0) - x_d\| < d$$

where $\Delta\bar{x}_0$ is the accumulation of corrections $\delta\bar{x}_0$ which yields x_d within the desired tolerance d . Thus, the procedure of differential correction proceeds as follows:

We choose a guess initial condition, $\bar{x}_{0,g}$ at $t_0 = 0$, for example this is of the form $[x_0, y_0, 0, 0]^T$ for the roll-pitch coupled model (4.3.2).

Using a high tolerance (typically 10^{-14}) for a standard integration package, we integrate this initial condition until the *half-period event* is satisfied. This gives us $\bar{x}(t_1)$, so we can compute $\Phi(t_1, 0)$ and for a periodic orbit, the desired final state has the form

$$\bar{x}(t_1) = [x_1, y_1, 0, 0]^T$$

where, $t_1 = T/2$, a *half-period* of the periodic orbit. As a result of numerical integration, the obtained value of v_{x_1} may not be 0 and for our purpose of convergence, we want $|v_{x_1}| < d$ (for example, $d = 10^{-10}$). Thus, the state transition matrix after one half-cycle, $\Phi(t_1, 0)$, can be used to correct the initial condition to obtain a periodic orbit as

$$\delta\bar{x}_1 \approx \Phi(t_1, 0)\delta\bar{x}_0 + \dot{\bar{x}}_1\delta t_1$$

Suppose $|v_{x_1}| > d$ and we keep x_0 constant, then expanding the above linear system, the correction to v_{y_0} can be calculated from

$$v_{x_1} = \delta v_{x_1} = \Phi_{32}\delta y_0 + \dot{v}_{x_1}\delta t_1 + h.o.t.$$

$$0 = \delta v_{y_1} = \Phi_{42}\delta y_0 + \dot{v}_{y_1}\delta t_1 + h.o.t$$

where, $\Phi_{i,j}$ is an element of the matrix $\Phi(t_1, 0)$ and \dot{v}_{x_1} comes from the equations of motion evaluated at the *half-period event*, $t = t_1$. Here, we set $v_{x_1} = \delta v_{x_1}$ to enforce $v_{x_1} = 0$. Furthermore, eliminating δt_1 , we get

$$\delta t_1 = -\frac{\Phi_{42}\delta y_0}{\dot{v}_{y_1}}$$

and substituting in the equation for correction to δv_{x_1} , we get

$$\begin{aligned} v_{x_1} &= \Phi_{32} \delta y_0 + \dot{v}_{x_1} \left(-\Phi_{42} \frac{\delta y_0}{\dot{v}_{y_1}} \right) \\ v_{x_1} &= \delta y_0 \left(\Phi_{32} - \Phi_{42} \frac{\dot{v}_{x_1}}{\dot{v}_{y_1}} \right) \end{aligned}$$

and hence the y -coordinate should be corrected by

$$\delta y_0 = \left(\Phi_{32} - \Phi_{42} \frac{\dot{v}_{x_1}}{\dot{v}_{y_1}} \right)^{-1} v_{x_1} \quad (\text{C.4-5})$$

Thus, the differential correction in one of the coordinates can be used to correct the guess for initial condition of a periodic orbit. This can be adopted as a general numerical procedure for unstable periodic orbits or unstable solutions of differential equations with known end points.

C.5 Boundary of total energy on surface-of-section

The energy surface given by (4.2.12) can be visualized as an ellipsoid in the (y, v_y, v_x) -space. When $x = 0$, that is the intersection with the surface-of-section, U_1 (4.2.13) or (4.2.14), the total energy (4.2.12) becomes

$$E(x, y, v_x, v_y) = e = \frac{y^2}{1} + \frac{v_y^2}{R^2} + \frac{v_x^2}{2} \quad (\text{C.5-1})$$

$$\frac{y^2}{(\sqrt{e})^2} + \frac{v_y^2}{(R\sqrt{e})^2} + \frac{v_x^2}{(\sqrt{2e})^2} = 1 \quad (\text{C.5-2})$$

Now, the boundary of energetically accessible region on the surface-of-section, U_1 or U_2 , is given by $v_x = 0$. Thus the boundary of constant total energy is the ellipse

$$\frac{y^2}{(\sqrt{e})^2} + \frac{v_y^2}{(R\sqrt{e})^2} = 1 \quad (\text{C.5-3})$$

with $2R\sqrt{e}$ as major axis and $2\sqrt{e}$ as minor axis for $R > 1$.

Chapter 5

Conclusions

“The purpose of computation is insight, not numbers.” – Richard Hamming

In this dissertation, I explored methods in nonlinear dynamics and chaos theory that are based on geometry of solutions which has implications in diverse areas of mechanics, physical sciences, and engineering. The mathematical ideas are discussed in the context of ordinary differential equations and flow maps that can be readily obtained for a given dynamical system with geometric constructions [16, 87] like surface-of-section and invariant manifolds. These techniques serve as means of *coarse grain sampling* of the phase space that is significant from the perspective of global transport and control.

One aspect of studying phase space transport is to characterize dynamically distinct trajectories of the system. For incompressible, inviscid fluid flow, this is applicable for studying transport of phase space volume which can be used to define intrinsic and extrinsic properties of the system. The time evolution of these properties is of interest for optimizing or designing mechanical devices. For control systems, the understanding of global transport inspires control laws to be aware of the *partial barriers* in phase space and hence can be used along with energy or time constraints for solving optimal control problems. The theory, numerical methods and computational results presented in Chapter 2 are meant to serve this

objective.

The other aspect of phase space transport is the prediction and control of escape or transition in potential well which is ubiquitous in nonlinear dynamics with multiple equilibria. I presented the phenomena in the context of ship dynamics and capsize for 1 DOF and 2 DOF models in Chapter 3 and Chapter 4, respectively. By applying this concept to problems in mechanics, my objective is to appeal and draw attention of scientists and engineers in physical sciences and applied mechanics. Furthermore, my objective is to show the relevant geometric construction for predicting escape or transition phenomena. Next, using these phase space structures, I advanced the application of partial control to avoid escaping in presence of disturbance, while using a smaller control. The results obtained in the Chapter 3 and Chapter 4 are counter-intuitive yet provide numerical evidence of finding safety in engineering systems in face of what may seem to be insurmountable disturbance. In short, partial control is an appealing method due to two important conditions: avoiding escape/transition using a *smaller control than the disturbance* and sustaining dynamics in a region of phase space without solving for a *specific trajectory*.

5.1 Contributions and future directions

This dissertation research aimed at using concepts from geometry and low-dimensional topology to global transport in phase space, and demonstrated the analytical and numerical methods by applying it to problems in mechanics and engineering. In closing, I want to reflect upon the contributions in terms of the following:

- **C1** Numerical method in lobe dynamics which is an attempt at generalized computation of intersection points and areas for closed curves. This opens up a new avenue of research in using concepts from computational geometry such as winding number, detection of intersection points to problems of phase space transport. Future directions

include detection of Lagrangian Coherent Structures in 3D and optimal control using front propagation.

- **C2** Escaping dynamics as a framework for studying critical events and designing avoidance behavior. In this context, I introduced the notion of defining escaping zone based on events relevant to the physics of the problem, and using geometric construction of Poincaré surface-of-section and tube dynamics.
- **C3** Application of partial control and avoiding escape from a potential well to a problem of engineering significance. Until now, the applied problems are in population model in ecology [88], extinction of healthy cells [89], and models of axisymmetrical galaxy [48]. I hope this reignites interest in control of chaos and escaping dynamics in engineering systems.
- **C4** Connecting the notion of discrete disturbance with continuous noise that is generated due to random forcing. This investigation lays down the foundation for discrete representation of noise such that partial control can have broader applications.

However, there are still some “holes” to be filled, and pillars to be strengthened in this field to complete the edifice of geometric view of phase space transport and partial control of escaping dynamics. I summarize these as follows:

- *Merging of algorithms from computational geometry with lobe dynamics* to enhance transport calculations in higher dimensional dynamical systems.
- *Guarantee of safe sets existence for a given dynamical system from a parameter standpoint?* Critical dynamics near the non-existence of safe set has been observed in computations which implies the a parameter dependence near the vanishing of safe set.

- *Partial control time step or minimum control frequency* required in applying partial control that should complete the picture from a control engineer's perspective.
- *Phase space representation of continuous noise* that should account for the effects of the random forcing as a discrete disturbance. I hope the presented investigation in this dissertation will launch interests in this direction.

Complete list of references

- [1] Hassan K. Khalil, *Nonlinear systems* 3rd ed. Prentice-Hall Inc., Upper Saddle River, New Jersey 07458, 2002
- [2] S. Wiggins, *Global Dynamics, Phase Space Transport, Orbits Homoclinic to Resonances, and Applications* Fields Institute Monographs American Mathematical Society, 1993
- [3] S. Wiggins, *Chaotic Transport in Dynamical Systems* vol. 2 Interdisciplinary Appl. Math. Berlin-Heidelberg-New York: Springer, 1992
- [4] Darin Beigie, Anthony Leonard, and Stephen Wiggins, A global study of enhanced stretching and diffusion in chaotic tangles, 3.May (1991), 1039–1050
- [5] Jong Hyun Kim and John Stringer, *Applied chaos* John Wiley & Sons, 1992
- [6] Stephen Wiggins, *Chaotic transport in dynamical systems*
- [7] Vered Rom-Kedar, Anthony Leonard, and Stephen Wiggins, An analytical study of transport , mixing and chaos in an unsteady vortical flow, *Journal of Fluid Mechanics*, (1990)
- [8] Vered Rom-Kedar, *Part I: An Analytical Study of Transport, Mixing, and Chaos in an Unsteady Vortical Flow. Part II: Transport in Two Dimensional Maps.* PhD thesis California Institute of Technology, 1988

- [9] T. Uzer, C. Jaffé, J. Palacián, P. Yanguas, and S. Wiggins, The geometry of reaction dynamics, *Nonlinearity*, 15 (2002), 957–992
- [10] C. Jaffé, David Farrelly, and T. Uzer, Transition state in atomic physics, *Phys. Rev. A*, 60 (1999), 3833–3850
- [11] Charles Jaffé, Shane Ross, Martin Lo, Jerrold Marsden, David Farrelly, and T. Uzer, Statistical Theory of Asteroid Escape Rates, *Physical Review Letters*, 89.1 (2002), 011101
- [12] J M T Thompson and M S Soliman, Fractal Control Boundaries of Driven Oscillators and their Relevance to Safe Engineering Design, *Proceedings of the Royal Society A: Mathematical, Physical and Engineering Sciences*, 428.1874 (1990), 1–13
- [13] J. M. T. Thompson, R. C. T. Rainey, and M. S. Soliman, Mechanics of Ship Capsize under Direct and Parametric Wave Excitation, *Philosophical Transactions of the Royal Society A: Mathematical, Physical and Engineering Sciences*, 338.1651 (1992), 471–490
- [14] J. M. T. Thompson and J. R. D. Souza, Suppression of Escape by Resonant Modal Interactions: In Shell Vibration and Heave-Roll Capsize, *Proceedings of the Royal Society A: Mathematical, Physical and Engineering Sciences*, 452.1954 (1996), 2527–2550
- [15] J. M. T. Thompson, Designing Against Capsize in Beam Seas: Recent Advances and New Insights, *Applied Mechanics Reviews*, 50.5 (1997), 307
- [16] John Michael Tutill Thompson and H Bruce Stewart, *Nonlinear dynamics and chaos* John Wiley & Sons, 2002
- [17] Tomasz Kapitaniak, *Controlling Chaos* Academic Press, 1996
- [18] Vered Rom-Kedar, A. Leonard, and S. Wiggins, An analytical study of transport, mixing and chaos in an unsteady vortical flow, *J. Fluid Mech.*, 214 (1990), 347–394
- [19] D. Beigie, Multiple separatrix crossing in multi-degree-of-freedom Hamiltonian flows, *English Journal of Nonlinear Science*, 5.1 (1995), 57–103

- [20] Francois Lekien, Shawn C. Shadden, and Jerrold E. Marsden, Lagrangian coherent structures in n -dimensional systems, *Journal of Mathematical Physics*, 48.6, 065404 (2007), 1–19
- [21] M. Dellnitz, O. Junge, W. S. Koon, F. Lekien, M. W. Lo, J. E. Marsden, K. Padberg, R. Preis, S. D. Ross, and B. Thiere, Transport in dynamical astronomy and multibody problems, *Int. J. Bifurc. Chaos*, 15 (2005), 699–727
- [22] J Duan and S Wiggins, Lagrangian transport and chaos in the near wake of the flow around an obstacle: a numerical implementation of lobe dynamics, *Nonlinear Processes in Geophysics*, 4.3 (1999), 125–136
- [23] Roger M Samelson and Stephen Wiggins, *Lagrangian transport in geophysical jets and waves: the dynamical systems approach* vol. 31 Springer, 2006
- [24] Vered Rom-Kedar and S. Wiggins, Transport in two-dimensional maps, *Arch. Rat. Mech. Anal.*, 109 (1990), 239–298
- [25] Vered Rom-Kedar, Transport in a class of n -d.o.f. systems, *Hamiltonian Systems with Three or More Degrees of Freedom (S’Agaró, 1995)*, vol. 533 NATO Adv. Sci. Inst. Ser. C Math. Phys. Sci. Dordrecht: Kluwer Acad. Publ., 1999, 538–543
- [26] Björn Sandstede, Sanjeeva Balasuriya, Christopher K R T Jones, and Patrick Miller, Melnikov theory for finite-time vector fields, *Nonlinearity*, 13.4 (2000), 1357–1377
- [27] Sanjeeva Balasuriya, Approach for maximizing chaotic mixing in microfluidic devices, *Physics of Fluids*, 17.11 (2005), 118103
- [28] Sanjeeva Balasuriya, Cross-separatrix flux in time-a-periodic and time-impulsive flows, *Nonlinearity*, 19.12 (2006), 2775–2795
- [29] Sanjeeva Balasuriya, Gary Froyland, and Naratip Santitissadeekorn, Absolute flux optimising curves of flows on a surface, *Journal of Mathematical Analysis and Applications*, 409.1 (2014), 119–139

- [30] K. A. Mitchell, J. P. Handley, J. B. Delos, and S. K. Knudson, Geometry and topology of escape. II. Homotopic lobe dynamics, *Chaos*, 13.3 (2003), 892–902 arXiv: [0307020](https://arxiv.org/abs/0307020) [[nlin.CD](#)]
- [31] K. A. Mitchell, J. P. Handley, B. Tighe, J. B. Delos, and S. K. Knudson, Geometry and topology of escape. I. Epistrophes, *Chaos: An Interdisciplinary Journal of Nonlinear Science*, 13.3 (2003), 880
- [32] Kevin A. Mitchell and John B. Delos, A new topological technique for characterizing homoclinic tangles, *Physica D: Nonlinear Phenomena*, 221.2 (2006), 170–187
- [33] V Rom-Kedar and S Wiggins, Transport in two-dimensional maps, *Archive for Rational Mechanics and Analysis*, 109.3 (1990), 239–298
- [34] W. S. Koon, M. W. Lo, J. E. Marsden, and S. D. Ross, *Dynamical Systems, the Three-Body Problem and Space Mission Design* ISBN 978-0-615-24095-4: Marsden Books, 2008
- [35] Ana M. Mancho, Des Small, Stephen Wiggins, and Kayo Ide, Computation of stable and unstable manifolds of hyperbolic trajectories in two-dimensional, aperiodically time-dependent vector fields, *Physica D: Nonlinear Phenomena*, 182.3-4 (2003), 188–222
- [36] R. S. MacKay, J. D. Meiss, and I. C. Percival, Transport in Hamiltonian systems, *Physica D*, 13 (1984), 55–81
- [37] J. M. T. Thompson and J. R. de Souza, Suppression of escape by resonant modal interactions: in shell vibration and heave-roll capsize, *Proc. R. Soc. Lond. A*, 452 (1996), 2527–2550
- [38] Charles Jaffé, Shane D Ross, Martin W Lo, Jerrold Marsden, David Farrelly, and T Uzer, Statistical theory of asteroid escape rates, *Physical Review Letters*, 89.1 (2002), 011101

- [39] C. Jaffé, S. D. Ross, M. W. Lo, J. E. Marsden, D. Farrelly, and T. Uzer, Theory of asteroid escape rates, *Physical Review Letters*, 89 (2002), 011101
- [40] Jaffé, Charles and Farrelly, David and Uzer, T, Transition state in atomic physics, *Physical Review A*, 60.5 (1999), 3833
- [41] Mohamed S. Soliman and J. M. T. Thompson, Transient and steady state analysis of capsize phenomena, *Applied Ocean Research*, 13.2 (1991), 82–92
- [42] Tristan Perez, *Ship Motion Control* Springer-Verlag
- [43] C. Jiang, A. W. Troesch, and S. W. Shaw, Capsize criteria for ship models with memory-dependent hydrodynamics and random excitation, *Philosophical Transactions of the Royal Society A: Mathematical, Physical and Engineering Sciences*, 358.1771 (2000), 1761–1791
- [44] Jeffrey M. Falzarano, Steven W. Shaw, and Armin W. Troesch, Application of global methods for analyzing dynamical systems to ship rolling motion and capsizing, *International Journal of Bifurcation and Chaos*, 2 (1992), 101–115
- [45] I. Senjanovic, G. Cipric, J. Parunov, and J. Senjanovic, I. and Cipric, G. and Parunov, Survival Analysis of Fishing Vessels Rolling in Rough Seas, *Philosophical Transactions: Mathematical, Physical and Engineering Sciences*, 358.1771 (2000), 1943–1965
- [46] Luis Perez-Rojas, Sara Sastre, and Ainara Martin, Review of the ship accidents investigations presented at the STAB presented at the STAB, *Proceedings of 10th International Ship Stability Workshop*, (2008), 219–233
- [47] LS McCue, Applications of finite-time Lyapunov exponents to the study of capsize in beam seas, *Contemporary Ideas on Ship Stability and Capsizing in waves*, (2011), 1–9
- [48] Mattia Coccolo, Jesús M. Seoane, Samuel Zambrano, and Miguel a. F. Sanjuán, Partial Control of Escapes in Chaotic Scattering, *International Journal of Bifurcation and Chaos*, 23.01 (2013), 1350008

- [49] Juan Sabuco, Samuel Zambrano, Miguel A F Sanjuán, and James A Yorke, Finding safety in partially controllable chaotic systems, *Communications in Nonlinear Science and Numerical Simulation*, 17.11 (2012), 4274–4280
- [50] Juan Sabuco, Samuel Zambrano, and Miguel A F Sanjuán, Partial control of chaotic transients using escape times, *New Journal of Physics*, 12.11 (2010), 113038
- [51] Juan Sabuco, Miguel a F Sanjuán, and James a Yorke, Dynamics of partial control. *Chaos (Woodbury, N.Y.)*, 22.4 (2012), 047507
- [52] Juan Sabuco, Samuel Zambrano, Miguel a.F. Sanjuán, and James a. Yorke, Finding safety in partially controllable chaotic systems, *Communications in Nonlinear Science and Numerical Simulation*, 17.11 (2012), 4274–4280
- [53] K. J. Spyrou and J. M. T. Thompson, The nonlinear dynamics of ship motions: a field overview and some recent developments, *Philosophical Transactions of the Royal Society A: Mathematical, Physical and Engineering Sciences*, 358.1771 (2000), 1735–1760
- [54] Huan Lin and Solomon C S Yim, Chaotic roll motion and capsize of ships under periodic excitation with random noise, *Applied Ocean Research*, 17.3 (1995), 185–204
- [55] J. Randolph Paulling and R. M. Rosenberg, On Unstable Ship Motions Resulting From Nonlinear Coupling, *Journal of Ship Research*, 3 (1959), 36–46
- [56] Ali H. Nayfeh, Dean T. Mook, and Larry R. Marshall, Nonlinear Coupling of Pitch and Roll Modes in Ship Motions, *Journal of Hydronautics*, 7.4 (1973), 145–152
- [57] Ali H. Nayfeh, Dean T. Mook, and Larry R. Marshall, Perturbation-Energy Approach for the Development of the Nonlinear Equations of Ship Motion, *Journal of Hydronautics*, 8.4 (1974), 130–136
- [58] Dean T Mook, Larry R Marshall, and All H Nayfeh, Subharmonic and Superharmonic Resonances in the Pitch and Roll Modes of Ship Motions, *Journal of Hydronautics*, 8.1 (1974), 32–40

- [59] Leigh S. McCue and Armin W. Troesch, The effect of coupled heave/heave velocity or sway/sway velocity initial conditions on capsizing modeling, *Proceedings of the 8th International Conference on Stability of Ships and Ocean Vehicles, Madrid, Spain, 2003*, 521–529
- [60] Leigh McCue and Armin Troesch, Probabilistic determination of critical wave height for a multi-degree of freedom capsizing model, *Ocean Engineering*, 32.13 (2005), 1608–1622
- [61] L. McCue, C. Bassler, and W. Belknap, Real-time Identification of Behavior Leading to Capsizing, *Proceedings of the 9th International Conference on Stability of Ships and Ocean Vehicles, Rio de Janeiro, Brazil, 2006*
- [62] Marcelo A.S. Neves and Claudio A. Rodríguez, On unstable ship motions resulting from strong non-linear coupling, *Ocean Engineering*, 33.14-15 (2006), 1853–1883
- [63] Marcelo A.S. Neves and Claudio A. Rodríguez, A coupled non-linear mathematical model of parametric resonance of ships in head seas, *Applied Mathematical Modelling*, 33.6 (2009), 2630–2645
- [64] Wang Sang Koon, Martin W. Lo, Jerrold E. Marsden, and Shane D. Ross, Heteroclinic connections between periodic orbits and resonance transitions in celestial mechanics. *Chaos (Woodbury, N.Y.)*, 10.2 (2000), 427–469
- [65] Wang-Sang Koon, Jerrold E Marsden, Shane D Ross, Martin Lo, and Daniel J Scheeres, Geometric mechanics and the dynamics of asteroid pairs. *Annals of the New York Academy of Sciences*, 1017 (2004), 11–38
- [66] Tristan Perez, *Ship Motion Control*. Advances in Industrial Control London: Springer-Verlag, 2005 chap. 2
- [67] Miguel Angel Sepulveda and Eric J. Heller, Semiclassical analysis of hierarchical spectra, *The Journal of Chemical Physics*, 101.9 (1994), 8016

- [68] Dmytro Babyuk, Robert E. Wyatt, and John H. Frederick, Hydrodynamic analysis of dynamical tunneling, *The Journal of Chemical Physics*, 119.13 (2003), 6482
- [69] R Barrio, F Blesa, and S Serrano, Bifurcations and safe regions in open Hamiltonians, *New Journal of Physics*, 11.5 (2009), 053004
- [70] Wang Sang Koon, Martin W Lo, Jerrold E Marsden, and Shane D Ross, Dynamical systems, the three-body problem and space mission design, 21 (2011), 327
- [71] Jurgen Moser, On the generalization of a theorem of A. Liapounoff, *Communications on Pure and Applied Mathematics*, XI (1958), 257–271
- [72] K. R. Meyer, G. R. Hall, and D. Offin, *Introduction to Hamiltonian Dynamical Systems and the N-Body Problem* Springer, 2009
- [73] Wang Sang Koon, Martin W. Lo, Jerrold E. Marsden, and Shane D. Ross, Heteroclinic connections between periodic orbits and resonance transitions in celestial mechanics. *Chaos (Woodbury, N. Y.)*, 10.2 (2000), 427–469
- [74] Jerrold E. Marsden and Shane D. Ross, New methods in celestial mechanics and mission design, *Bulletin of the American Mathematical Society*, 43.1 (2006), 43–73
- [75] Tristan Perez and Mogens Blanke, Ship roll motion control, *Proceedings of the 8th IFAC Conference on Control Applications in Marine Systems, Rostock, Germany, 2010*, 1–12
- [76] Shang-Rou Hsieh, Armin W. Troesch, and Steven W. Shaw, A Nonlinear Probabilistic Method for Predicting Vessel Capsizing in Random Beam Seas, *Proceedings of the Royal Society A: Mathematical, Physical and Engineering Sciences*, 446.1926 (1994), 195–211
- [77] Juan Sabuco, Samuel Zambrano, Miguel A F Sanjuán, and James A. Yorke, Finding safety in partially controllable chaotic systems, *Communications in Nonlinear Science and Numerical Simulation*, 17.11 (2012), 4274–4280

- [78] Juan Sabuco, Miguel a F Sanjuán, and James a Yorke, Dynamics of partial control. *Chaos (Woodbury, N. Y.)*, 22.4 (2012), 047507
- [79] Samuel Zambrano, Miguel a. F. Sanjuán, and James a. Yorke, Partial control of chaotic systems, *Physical Review E*, 77.5 (2008), 055201
- [80] Ying-Cheng Lai and Tamás Tél, *Transient Chaos* vol. 48 1 Springer-Verlag, 2010, 146–146
- [81] Mattia Coccolo, Jesús M Seoane, Samuel Zambrano, and Miguel a. F Sanjuán, Partial Control of Escapes in Chaotic Scattering, *International Journal of Bifurcation and Chaos*, 23.01 (2013), 1350008
- [82] Y.-W. Lee, L. S. McCue, M. S. Obar, and A. W. Troesch, Experimental and numerical investigation into the effects of initial conditions on a three degree of freedom capsizing model, *Journal of Ship Research*, 50.1 (2006), 63–84
- [83] C Jaffé, D Farrelly, and T Uzer, Transition state in atomic physics, *Phys Rev A*, 60.5 (1999), 3833–3850
- [84] Frederic Gabern, Wang S. Koon, Jerrold E. Marsden, and Shane D. Ross, Theory and computation of non-RRKM lifetime distributions and rates in chemical systems with three or more degrees of freedom, *Physica D: Nonlinear Phenomena*, 211.3-4 (2005), 391–406
- [85] F. Gabern, W. S. Koon, J. E. Marsden, S. D. Ross, and T. Yanao, Application of tube dynamics to non-statistical reaction processes, *Few-Body Systems*, 38.2-4 (2006), 167–172
- [86] A S White, P T Gleeson, and M Karamanoglu, Control of Ship capsizing in stern quartering seas. *International Journal of Simulation Systems, Science & Technology.*, 8.2 (2007), 20–31

- [87] S Foale and J Thompson, Geometrical concepts and computational techniques of non-linear dynamics, *Computer Methods in Applied Mechanics and Engineering*, 89.1-3 (1991), 381–394
- [88] Rubén Capeáns, Juan Sabuco, and Miguel A F Sanjuán, When less is more: Partial control to avoid extinction of predators in an ecological model, *Ecological Complexity*, 19.2 (2014), 1–8
- [89] Álvaro G López, Juan Sabuco, Jesús M Seoane, Jorge Duarte, Cristina Januário, and Miguel a F Sanjuán, Avoiding healthy cells extinction in a cancer model. *Journal of theoretical biology*, 349 (2014), 74–81